

Thermal Process Simulation of Reactive Particles on Moving Grates

Dissertation

zur Erlangung des Akademischen Grades

**Doktoringenieur
(Dr.-Ing.)**

von: M.Sc. Chuan Cheng
geb. am: 15.04.1970
in: Sichuan / V.R.China

genehmigt durch die Fakultät für Verfahrens- und Systemtechnik
der Otto-von-Guericke-Universität Magdeburg.

Gutachter: Prof. Dr.-Ing. Eckehard Specht
Prof. Dr.-Ing. Michael Beckmann

eingereicht am: 08.05.2007
Promotionskolloquium am: 22.05.2007

Schriftliche Erklärung

Ich erkläre hiermit, dass ich die vorliegende Arbeit ohne unzulässige Hilfe Dritter und ohne Benutzung anderer als der angegebenen Hilfsmittel angefertigt habe; die aus fremden Quellen direkt oder indirekt übernommenen Gedanken sind als solche kenntlich gemacht.

Insbesondere habe ich nicht die Hilfe einer kommerziellen Promotionsberatung in Anspruch genommen. Dritte haben von mir weder unmittelbar noch mittelbar geldwerte Leistungen für Arbeiten erhalten, die im Zusammenhang mit dem Inhalt der vorgelegten Dissertation stehen.

Die Arbeit wurde bisher weder im Inland noch im Ausland in gleicher oder ähnlicher Form als Dissertation eingereicht und ist als Ganzes auch noch nicht veröffentlicht.

München, den 03.05.2007

Danksagung

Die vorliegende Dissertation entstand während meiner Tätigkeit im Institut für Strömungs- und Thermodynamik an der Otto-von-Guericke-Universität Magdeburg in den Jahren 2003 bis 2007.

Mein besonderer Dank gilt meinem Doktorvater Herrn Prof. Dr.-Ing. habil. Eckehard Specht für die Anregung zu dieser Arbeit, die stete Unterstützung und Betreuung.

Außerdem danke ich Herrn Prof. Dr.-Ing. habil. Michael Beckmann von der Bauhaus-Universität Weimar für die Bereitschaft als Gutachter zu wirken.

Herrn Prof. Dr.-Ing. habil. Ulrich Hauptmanns und der Firma Drägerwerk AG danke ich für die finanzielle Unterstützung.

Für ihre Hilfsbereitschaft in wissenschaftlichen Fragen und für die freundliche Arbeitsatmosphäre danke ich allen ehemaligen und augenblicklichen Mitarbeiterinnen und Mitarbeitern des Instituts für Strömungstechnik und Thermodynamik (ISUT).

Kurzfassung

Die Wanderroste werden in vielen Industriezweigen verwendet. Für die Verbesserung der Produktqualität (bei der Abkühlung des Zementklinkers), die Energieeinsparung (beim Vorwärmen des Kalksteins), die Emissionskontrolle (bei der Abfallverbrennung) oder die Analyse einiger spezieller Betriebsprobleme (wie z.B. Überhitzung des Wanderrostes oder Fluidisation der Feinpartikel), ist es wichtig, die physikalischen und chemischen Phänomene in den Gas-Partikel-Systemen auf den Wanderrosten zu simulieren. In dieser Dissertation wurden zwei numerische Simulationsmodelle für Verhalten reaktiver Partikel auf Wanderrosten basierend auf der Zellenmethode entwickelt.

Das Programm LEPOL simuliert das Trocknen, die Vorwärmung, die Teilentsäuerung und die Nachwärmung der Kalksteinpartikel auf einem großen LEPOL-Rost, der vor einem Kalkdrehofen platziert ist. Der Hauptzweck der Simulation ist zu zeigen, wie man die Durchschnitts- bzw. Spitzentemperatur des Heißgases beim Austritt aus der Steinschüttung senken kann, um das Rostglied vor der Gashitze zu schützen. Aufgrund des ungünstigen Wärmekapazitätsstromsverhältnisses zwischen Gas und Steinschüttung kann das Rostglied effektiv geschützt werden, indem man die Heißgasmenge von der Gaskammer durch einen Bypass verringert.

Als Bestandteil des Programms wurden quasistationäre Kern-Schale-Modelle für die Zersetzung des Kalksteins und des Magnesits entwickelt. Darüber hinaus wurden zwei unterschiedliche Zersetzungsmodelle jeweils für separate und simultane (mit hintereinander laufender Reaktionsfronte) Zersetzung der Bestandteile $MgCO_3$ und $CaCO_3$ im Dolomit hergeleitet. Es wurde ein Verfahren beschrieben, die Reaktions-, Porendiffusions- und Wärmeleitkoeffizienten während der Zersetzung der Erdalkalien (unterschiedlich in Art und Ursprung) durch Linearisierung der Umwandlungskurven auszuwerten.

Ein weiteres Programm CLINKER simuliert die Schnellkühlung der Zementklinkerpartikel auf einem ähnlichen Wanderrost, um die Betriebsparameter zu optimieren und die Fluidisation der Kleinpartikel zu vermeiden. Das Fluidisationsphänomen der Kleinpartikel kann durch einen verlängerten Rost, eine schnellere Rostgeschwindigkeit, eine kleinere Kühlluftmenge, einen geringeren Klinkerdurchsatz oder eine größere Partikelgröße vermieden werden.

Schlüsselwörter: Wanderrost, LEPOL, Partikel, Kalkstein, Zersetzung, Klinker, Fluidisation

Abstract

The moving grates, or travelling grates, are widely used in industries. For the purpose of product quality improvement (in quenching of clinker), energy consumption reduction (in pre-heating of limestone), emission control (in waste incineration) or to tackle some special operation problems (such as over heating of grates or fluidisation of fine particles), it is important to simulate the physical and chemical phenomena in the gas-solid systems on the moving grates. In this dissertation, two numerical bed models with cell method were established to Simulation of reactive particles on moving grates.

Program LEPOL simulated the drying, pre-heating and partial calcination of limestone particles on a travelling LEPOL-Grate, which was built in front of a lime rotary kiln. The main purpose of the simulation was to show how to decrease the average or peak temperature of the hot gas when it reaches the LEPOL-Grate, in order to protect the grate from the gas heat. This could be achieved effectively by reducing the hot gas amount with a gas bypass at the roof of hot gas chamber.

As a part of above program, one-dimension steady-state shrinking core models were built for the decomposition of limestone and magnesite. For dolomite, furthermore, both separate and simultaneous decomposition models of $MgCO_3$ and $CaCO_3$ components in dolomite were established. A method was described to evaluate the reaction rate coefficients, pore diffusivity and thermal conductivity during decomposition of the three earth alkalis of different types and origins, by linearization of conversion curves.

Another program, CLINKER, simulated the rapid cooling down of clinker particles on a similar moving grate. The purpose of the simulation was to find some methods to avoid the fluidisation of smaller clinker particles. The fluidisation phenomena of smaller clinker particles could be avoided by a prolonged grate, a rapid grate velocity (means correspondingly a smaller clinker particle bed height), smaller air input amount, smaller clinker through-put or bigger clinker particle size.

Keywords: Moving grate, LEPOL, Particle, Limestone, Decomposition, Clinker, Fluidisation

Contents

1.	Introduction.....	1
2.	Description of processes on moving grates	3
2.1	Preheating and decomposition of earth alkali.....	3
2.2	Cooling down of clinker	3
2.3	Waste incineration.....	4
2.4	Sintering of iron oxides	4
3.	General description of sub-processes	6
3.1	General method to simulate process on a moving grate.....	6
3.2	Determination of heat transfer coefficient.....	6
3.2.1	Based on a flow over single particle	6
3.2.2	Based on a hydraulic diameter	7
3.2.3	Transient factor	8
3.3	Determination of mass transfer coefficient.....	8
3.4	Drying	9
3.5	Equivalent particle diameter	9
3.6	Void fraction of particle bed.....	11
3.7	Pressure drop in particle bed.....	11
3.7.1	Based on a hydraulic diameter	11
3.7.2	Based on particle cross flow	12
3.8	Fluidisation of particles.....	13
3.8.1	Principle of the fluidization of solid particle	13
3.8.2	Minimal fluidisation velocity	14
3.9	Decomposition of earth alkali	14
3.9.1	Decomposition model of limestone	14
3.9.2	Decomposition model of magnesite	17
3.9.3	Decomposition model of dolomite	17
4.	Building of models	22
4.1	Building of the model LEPOL	22
4.2	Building of the model CLINKER.....	22
4.3	Calculation of pure heat transfer	22
4.4	Calculation involving evaporation or reaction.....	24
5.	Material properties	25
5.1	Material properties in limestone decomposition	25
5.1.1	Equilibrium pressure	25
5.1.2	Evaluation method for k , D^p and λ	25
5.1.3	Experimental apparatus.....	26
5.1.4	Decomposition behaviour.....	27
5.1.5	Reaction coefficients.....	28
5.1.6	Effective pore diffusivity	28
5.1.7	Thermal conductivity	29
5.1.8	Heat capacity.....	29
5.2	Material properties in magnesite decomposition	29
5.2.1	Equilibrium pressure	30
5.2.2	Decomposition behaviour.....	31
5.2.3	Reaction rate coefficients	31
5.2.4	Effective pore diffusivity	31
5.2.5	Thermal conductivity	32
5.2.6	Heat capacity.....	32
5.3	Material properties in dolomite decomposition	32
5.3.1	Equilibrium pressure	32
5.3.2	Simultaneous decomposition behavior of both components	33
5.3.3	Separate decomposition behavior of both components	33
5.3.4	Reaction rate coefficients	34
5.3.5	Effective pore diffusivity	35
5.3.6	Thermal conductivity	35
5.3.7	Heat capacity.....	35
5.4	Clinker.....	36
5.5	Gas and air	36
6.	Simulation and result with the model LEPOL.....	38

6.1	Operation data	38
6.2	Simulation cases	38
6.2.1	Single-layer operation mode	38
6.2.2	Two-layer operation mode	39
6.3	Rough energy balance	40
6.4	Result analysis of case 0	40
6.5	Influencing parameters	41
6.6	Suggestions	46
7.	Simulation and result with the model CLINKER.....	47
7.1	Operation data	47
7.2	Simulation cases.....	47
7.3	Rough energy balance	48
7.4	Result analysis of case 0	48
7.5	Influencing parameters	48
7.6	Suggestions	51

Nomenclature

a	m^2/s	Temperature diffusivity
A	m^2	Surface
b	-	Form factor
c_p	$J/(kg \cdot K)$	Specific heat capacity at constant pressure
C	-	Volume fraction
d	m	Diameter
D	m^2/s	Diffusivity
f	-	Function
f	-	Factor
g	m/s^2	Gravity acceleration
h_{CO_2}	J/kg	Reaction enthalpy regarding to CO_2 in kg
h_{VAP}	J/kg	Evaporation enthalpy of water
$\Delta \tilde{H}_R$	J/mol	Molar reaction enthalpy
k	m/s	Reaction coefficient as in Equation (3.51)
k_1	$mol/(m^2 \cdot s)$	Reaction coefficient as in Equation (4.6)
K_{CO_2}	kg/m^3	CO_2 concentration in solid
l	m	Length
\dot{m}	$kg/(m^2 \cdot s)$	Mass flux
M	kg	Mass
\dot{M}	kg/s	Mass flow
\tilde{M}	kg/mol	Molar mass
n	-	Number of particle
n	-	Exponent index
\dot{n}	$mol/(m^2 \cdot s)$	Molar flux
N	-	Number of particle
\dot{N}	mol/s	Molar flow
O	m^2/kg	Specific surface of packed bed
P	N/m^2	Pressure
P	-	Heat exchange effectiveness
\dot{q}	W/m^2	Heat flux
\dot{Q}	W	Heat flow
r	m	Radial coordinate

R	1/s	Resistance
R	-	Heat capacity flow ratio
R _{CO₂}	J/(kg·K)	Gas constant for CO ₂
\tilde{R}	J/(mol·K)	Universal gas constant
t	s	Time
T	K	Temperature
x _i	-	Mass fraction of component i in a gas mixture
\tilde{x}_i	-	Molar or volume fraction of component i in a gas mixture
X	-	Conversion degree
V	m ³	Volume
w	m/s	Velocity
W	N	Resistance force
x,y,z	m	Local coordinates
\tilde{x}	-	Mole fraction
X	m	Length
α	W/(m ² ·K)	Heat transfer coefficient
β	m/s	Mass transfer coefficient
δ	m	Thickness of boundary layer
η	kg/(m·s)	Dynamic viscosity
κ	-	Transient factor
λ	W/(m·K)	Thermal conductivity
ν	m ² /s	Kinematic viscosity
ρ	kg/m ³	Density
Ψ	-	Void fraction of packed bed
Ψ	-	Sphericity

Subscripts:

B	Bulk
eff	Effective
eq	Equilibrium
F	Reaction front
F	Fluid
C	Core
CS	Circumscribing sphere
D	Diffusion
G	Gas
H	Hydraulic
k	Reaction

lam	Laminar
M	Mean
M	Mixture
max	Maximum
MF	Minimum fluidisation
min	Minimum
OX	Oxide
P	Pressure
P	Particle
S	Surface
S	Sphere
S	Solid
turb	Turbulent
VAP	Evaporation
W	Wadell sphericity
α	Heat transfer
β	Mass transfer
κ	Transient factor
λ	Thermal conduction
Ψ	Void fraction of packed bed
I	Decomposition of MgCO ₃ component in dolomite
II	Decomposition of CaCO ₃ component in dolomite

Superscripts:

P Pore

Dimensionless numbers:

Ar	Archimedes number
Bi	Biot number
Eu	Euler number
NTU	Number of transfer unit
Nu	Nusselt number
Pr	Prandtl number
Re	Reynolds number
Sc	Schmidt number
Sh	Sherwood number

1. Introduction

A moving grate, or travelling grate, is a flat frame consisting of steel segments, which can be driven to move in one direction or reciprocally. The function of such a grate is to hold or transport solid material, and at the same time to allow fluid, mostly air or gas, to penetrate through the clefts or orifices between or in the grate segments.

Moving grates are widely used apparatus, which have applications in many industry branches, such as:

- Heating up or drying of solid material by hot gas, such as preheating and pre-calcination of earth alkali (limestone, magnesite and dolomite),
- Cooling down of hot solid material, such as clinker, by cold air,
- Incineration of lumpy solid fuel, such as coal particles, wood pieces or municipal refuses,
- Sintering of raw iron ore in iron-making industry.

A number of different types of moving grate exist, for example, the roller grate, rocker grate, stoker grate, forward reciprocating systems and reverse reciprocating systems, as summarised by Clayton et al. [1]. These construction types of moving grate, which are often seen in industries, are shown in Figure 1.1.

For the purpose of product quality improvement (in quenching of clinker), energy consumption reduction (in pre-heating of limestone), emission control (in waste incineration) or to tackle some special problems, such as over heating of grate segments or fluidisation of fine particles, it is necessary to optimize the operation of the grates. This can be done through simulation of the physical and chemical phenomena in the gas-solid systems on the moving grates.

Three general types of simulation models can be applied: Computational Fluid Dynamics (CFD), stochastic models and bed models. CFD models simulate the fluid flow, heat and mass transfer and reaction phenomena above a traveling grate by solving numerically the continuity and energy conservation equations and the Navier-Stokes equations (conservation of momentum). Stochastic models, such as Markov chain models, are developed originally to estimate the mixing of powders in hoppers and the mixing in fluidized bed reactors. Nakamura and Themelis [2] have applied the Markov chain model for a waste incineration facility in order to determine how solid particles move and mix on a moving grate. Another approach is numerical bed model with cell method, which is described in VDI-Wärmeatlas [3]. It is typically applied for simulation of complicated heat exchanger.

In this dissertation, two numerical bed models with cell method are established to calculate the physiochemical processes on the moving grates, namely heat and mass transfer between gaseous and solid phases, and possible chemical reaction or the reactive particles.

The program LEPOL simulates the drying, pre-heating and partial calcination of limestone particles on a Lepol grate, which is built in front of a lime rotary kiln. In this application, the hot gas with a temperature of about 1100°C from the rotary kiln is diverted by a gas chamber, and flows nearly perpendicularly downwards through the limestone bed and the grate. In the practice, an often occurring problem is that the hot gas can not be cooled down sufficiently by the limestone. Therefore the grate segments, which undergo both high mechanic load and high gas temperature, could loose strength and be finally deformed. This will cause jam of the whole grate system and lead to troublesome and expensive shut down and maintenance. Through the simulation, the improvement potentials of processes are investigated, in order to protect the steel grate against the high gas temperature at exit.

As a part of above program, the kinetics of earth alkali decomposition should be extra studied. One-dimensional steady state shrinking core models are built for the decomposition of limestone and magnesite. For dolomite, furthermore, both separate and simultaneous decomposition models of

MgCO₃ and CaCO₃ components are established. An analytical method is described to evaluate the material properties (reaction coefficients, pore diffusivities and thermal conductivities) during the decomposition of the three earth alkalis of different types and origins, by linearization of conversion curves.

Another program, CLINKER, is written to simulate the rapid cooling down of clinker particles on a similar moving grate. Immediately after the rotary kiln, the clinker particles have a temperature as high as 1400°C. They should be cooled down by cold air as rapid as possible, so that the desired crystal structure can be formed to obtain a good cement quality. The quenching effect is realised by blowing a large amount of cold air upwards through the grate segments and clinker particle layer. The problem in this practice is, different from that in limestone preheating, that the fluidisation of fine clinker particle could take place. This limits the production capacity of a given grate system. The aim of the simulation is to optimize the grate operation to avoid fluidisation, but as the same the quenching rate must be still ensured.

2. Description of processes on moving grates

2.1 Preheating and decomposition of earth alkali

In the industry, the limestone will be broken by a crusher at first and washed by water to remove clay. Then they will be sieved and separated in two fractions: the coarse fraction between 30 and 70 mm and the fine fraction smaller than 30 mm. The coarse fraction is calcinated preferably in a norm shaft kiln, which can provide a more effective heat transfer. The smaller limestone particles, on the contrary, should be only decomposed in a rotary kiln; otherwise the pressure drop in norm shaft kiln could be so drastic that the combustion gas can not flow through the whole bed.

In a rotary kiln, the heat is obtained by combustion of gaseous fuel or coal powder. The gas burner is normally built at the lower end of the kiln tube, so the combustion gas flows counter current to the solid movement. As the heat transfer between gas and solid are mainly due to thermal radiation between the wall and solid bed surfaces, and heat conduction through the direct contact of wall and solid bed, the heat transfer is weaker than that in shaft kiln. When the hot gas exits at the kiln head, it has still very high temperature of about 1100°C. This enthalpy in gas can be recycled when an additional grate system is built in front of the kiln head for preheating the cold limestone with the hot gas.

A typical Lepol grate for limestone preheating has a big dimension, typically 23 meter long and 4 meter wide, which is shown in Figure 2.1.

On the moving grate, following four sub-processes can be observed in sequence:

- Drying of the wet limestone,
- Preheating of the dry limestone,
- Partial decomposition of limestone when the decomposition temperature is reached,
- After-heating of lime particles, after the decomposition of a particle has been completed.

The four physiochemical sub-processes are illustrated in Figure 2.2.

The grate moves with a velocity of about 22 m/h towards the kiln head and transports the limestone layer into the rotary kiln. The hot gas, which exits the kiln head with a temperature of about 1100°C, is diverted by a gas chamber and flows nearly perpendicularly downwards through the stone bed and the grate. Thus the limestone particles are heated up. When the decomposition temperature, which corresponds to a CO₂ fraction in the combustion gas, is reached, dissociation of the limestone begins, just like the calcination process in the rotary kiln itself. Depending on the gas temperature and residence time, the average conversion degree of limestone on the grate could vary from 15 to 25%. Therefore this system of gas chamber and grate is called sometimes pre-calcinator instead of pre-heater. In the practice, an often occurring problem is that the hot gas cannot be cooled down by the limestone sufficiently. Therefore the grate segments, which undergo both high mechanical load and high gas temperature, could loose strength and be finally deformed.

2.2 Cooling down of clinker

The raw material for Portland cement production is a mixture of minerals containing calcium oxide, silicon oxide, aluminium oxide, ferric oxide, and magnesium oxide. After preparation and blending, the raw material is burnt in a cement rotary kiln with temperatures increasing over the length of the cylinder up to 1450°C [4]. The resulting material, clinker, has therefore a temperature as high as 1400°C when leaving the kiln. The clinker must be cooled down for further transport and grinding, and for recovery of energy. More important, the clinker must be quenched as rapid as possible to obtain a desired quality. The cooling of the clinker influences its structure, the mineralogical composition, as well as the grindability, and consequently the behaviour of the interstitial material on hydration, which means quality of cement [5].

To quench the clinker particles, the grate cooler was developed in 1930's. It consists of a perforated grate enclosed in a rectangular chamber. A bed of clinker up to 0.5 m deep moves along the grate. The cold air is blown from the bottom of grate and flows upwards through the grate and the clinker layer. Compared with early types such as rotary coolers or satellite coolers, the grate systems can quench the clinker more rapidly. Because the apparatus does not rotate, it has another advantage: The heated air can be drawn out properly and reused in fuel drying, or as combustion air. A typical grate cooler in cement production is shown in Figure 2.3.

To intensify the cooling effect, a large flow rate of air is desired. But in the practice, this operation results in another problem: At the surface of solid bed small clinker pellets could begin to fluidize. The problem of fluidization limits the flow rate of cooling air, and thus the production capacity in a given apparatus.

2.3 Waste incineration

Grate systems are also used for solid fuel firing in furnaces or solid waste incinerators. A typical incineration system for municipal solid waste is shown in Figure 2.4 by Williams [6]. The process of waste incineration on a grate is very complicated, depending on the waste composition, moisture content, thermal degradation temperature, volatile fraction and ignition temperature of each component, and fixed carbon content. But generally the waste undergoes three sub-processes on a grate in the incinerator, which can be illustrated in Figure 2.5:

- Drying,
- Devolatilisation of organic material, and combustion of the volatiles will take place above the solid bed surface and in the combustion chamber,
- Combustion of the solid carbonaceous residue.

On entering the hot furnace, the waste is heated up by contact with the hot grate, convection from combustion gases and thermal radiation from walls of the chamber. The moisture content of municipal solid, which can vary between 25 and 50%, is driven off in the temperature range between 50 and 100°C.

After moisture release, the waste then undergoes thermal decomposition and pyrolysis. The volatile combustible gases and vapors are generated from the organic materials. In the organic matter of municipal waste, the volatiles amount to 70 - 90%. The devolatilisation takes place over a wide range of temperatures between 200 and 750°C. The combustion of volatiles to produce the flame takes place immediately above the waste bed surface and in the space of combustion chamber as well.

After the drying and devolatilisation stages, the residue consists of a carbonaceous char (fixed carbon) and some inert materials. The carbonaceous char, different from the volatile carbon in the volatiles, combusts on the grate and may take 30 - 60 minutes for a complete burn-out.

The grates transport the solid waste from the inlet hopper to the discharge end, providing agitation or mixing of the waste to stoke the fire and loosen the combusting materials. The grate can be driven with variable speeds to adjust the residence time of the waste in the combustion zone is the waste composition fluctuates.

2.4 Sintering of iron oxides

Iron sintering plants are often associated with iron and steel plants. The sintering process is a pre-treatment step in the iron production, where fine particles of iron ores (sometimes secondary iron oxide wastes as well) are agglomerated by combustion. Raw mix of iron ores, limestone, and fuel coke particles forms a bed on a traveling grate, which is illustrated in Figure 2.6. The aim of the sintering is to obtain a semi-molten mass with the appropriate size (bigger than 5 mm) and strength, which is necessary for feeding into blast furnaces.

The surface is ignited with a gas burner at the start of the grate, and air is drawn through the moving bed by a suction fan to enable the fuel combustion. The combustion begins at the top of the bed and propagates into the bed with sintering near the combustion front. Below the combustion front, the combustion gas evaporates moisture in the solid particles, while condensation occurs below the evaporation zone. These processes progress slowly through a traveling bed of 100 m for 30 - 60 minutes. The grate velocity and gas flow rate are controlled to ensure that "burn through" occurs just before the discharge of sintered material.

As shown in Figure 2.7 by Yang et al. [7], an iron particle in a sintering bed undergoes several stages of process in the direction of grate movement:

- Heating up,
- Moisture condensation,
- Moisture evaporation,
- Coke combustion and sintering,
- Cooling down of the sintered pellets.

3. General description of sub-processes

3.1 General method to simulate process on a moving grate

In principle the system of a moving bed of particle on the grate and a fluid, which is flowing perpendicularly through the bed, can be approximated by a cross flow heat exchanger. The gas or the air is one fluid stream, while the particle bed can be regarded as another fluid stream. The heat transfer area of this heat exchanger is then the total surface area of all the particles on the grate. Because the gas distribution and all temperatures are practically homogeneous in the width direction of the grate, the system can be simplified as a two-dimensional model. The temperature of gas or air changes with the height, while the temperature of the particles changes with the length.

To compute the temperature distribution of both fluids, the cell method described in VDI-Wärmeatlas [3] is applied. With the cell method the total bed space is divided into small cells, where the streams or parts of them flow sequently or parallel with each other. Each cell can be understood as a single heat exchanger with individual inlet and outlet temperatures of both flows. Inside of each cell, the masses, temperatures, heat transfer coefficients and other material properties of both flows are treated as constant. But they do differ from cell to cell.

Given the input temperatures, material properties, heat transfer coefficient and area for one cell, the two output temperatures can be calculated. These output temperatures can be used as input temperature for next cell. In this way the temperature distribution of both flows inside the whole particle bed can be computed.

In the program CLINKER, as no water evaporation or chemical reaction exist, the mass of air is constant along the height, and the mass of clinker does not change along the length. In the program LEPOL, however, the mass of the hot gas increases along the height due to water evaporation and produced CO₂ by limestone decomposition; the mass of limestone declines along the length correspondingly.

As all the properties of both flows are dependent on temperature, they have to be calculated for each cell. In the limestone or clinker bed, the heat convection dominates mostly. Given the temperatures and the flow condition, the heat and mass transfer coefficients can be obtained by Nusselt and Sherwood function for each cell.

3.2 Determination of heat transfer coefficient

3.2.1 Based on a flow over single particle

The values of the heat transfer coefficient between fluid and solid particles in a packed bed are significantly higher than the values of the heat transfer coefficient between fluid and a single sphere. The heat transfer coefficient for a packed bed can be calculated by modification of the heat transfer coefficient between fluid and a single solid sphere, which has been investigated sufficiently.

The heat transfer coefficient between fluid and a single solid sphere is calculated by Nusselt function according to Gnielinski [8] and [9]. The Nusselt function for a single sphere in laminar flow is:

$$Nu_{lam} = 0.644 \cdot Re^{\frac{1}{2}} \cdot Pr^{\frac{1}{3}} \quad (3.1)$$

The Nusselt function for a single sphere in turbulent flow is:

$$Nu_{turb} = \frac{0.037 \cdot Re^{0.8} \cdot Pr}{1 + 2.443 \cdot Re^{-0.1} \cdot (Pr^{0.667} - 1)} \quad (3.2)$$

From the two values, the Nusselt function for a single sphere can be averaged as:

$$Nu_s = 2 + \left(Nu_{lam}^2 + Nu_{urb}^2 \right)^{0.5} \quad (3.3)$$

The Prandtl number is defined as:

$$Pr = \frac{\nu}{a} \quad (3.4)$$

where ν is the kinematic viscosity,
and a the temperature conductivity, which is defined as:

$$a = \frac{\lambda_F}{\rho_F \cdot c_{pF}} \quad (3.5)$$

where λ_F is thermal conductivity of the fluid,
 ρ_F the density of the fluid,
and c_{pF} the specific heat capacity of the fluid.

The Reynolds number is defined as:

$$Re = \frac{w \cdot d}{\nu} \quad (3.6)$$

where w is the empty tube velocity,
and d the diameter of sphere.

When the particle has another geometric form, an equivalent diameter can be obtained by:

$$d = \sqrt{\frac{A_p}{\pi}} \quad (3.7)$$

where A_p is the measured surface area of a given particle.

The Nusselt number for a single sphere must be modified by a form factor f_ψ to obtain the Nusselt number in a packed bed:

$$Nu = f_\psi \cdot Nu_s \quad (3.8)$$

The form factor f_ψ of a bed packed with spheres of equal size can be calculated with sufficient accuracy for the void fraction range of $0.26 < \psi < 1$, from this correlation:

$$f_\psi = 1 + 1.5 \cdot (1 - \psi) \quad (3.9)$$

For cylinders with a length l to diameter d ratio within the range $0.24 < l/d < 1.2$, $f_\psi = 1.6$;

For a cube $f_\psi = 1.6$;

For the Raschig rings $f_\psi = 2.1$.

Therefore, the heat transfer coefficient, α , for a packed bed is obtained by:

$$\alpha = \frac{Nu \cdot \lambda_G}{d} \quad (3.10)$$

3.2.2 Based on a hydraulic diameter

Another approach to estimate heat transfer coefficient in a packed bed, which is given by Jeschar [10], uses a hydraulic diameter for particles. If the packing in a packed bed can be described as a bundle of parallel pipes, the hydraulic diameter of the particles, d_H , could be described with this relation:

$$d_H = \frac{2}{3} \cdot \frac{\psi}{1 - \psi} \cdot d \quad (3.11)$$

Expressing the Reynolds number with the hydraulic diameter gives the equation:

$$Re = \frac{w \cdot d}{\nu} \cdot \frac{1}{1 - \psi} \quad (3.12)$$

The Nusselt number is defined as:

$$Nu = \frac{\alpha \cdot d}{\lambda_G} \cdot \frac{\psi}{1-\psi} \quad (3.13)$$

In the range of $100 < Re < 40000$ and $0.6 < Pr < 1000$, the Nusselt function has this form:

$$Nu = 2 \cdot \frac{\psi}{1-\psi} + 1.12 \cdot Re^{\frac{1}{2}} \cdot Pr^{\frac{1}{3}} + 0.0056 \cdot Re \cdot Pr^{\frac{1}{3}} \quad (3.14)$$

Bes [11] has compared the convective heat transfer coefficients obtained from the two approaches. The results from the model based on single particle are slightly less than those from the hydraulic diameter model. For the typical air velocity of about 1 m/s at standard temperature and pressure, the difference between the results of both approaches is less than 20%.

3.2.3 Transient factor

The heating-up and the cooling down of solid particles is actually a transient process, so that the solid particle has a temperature distribution in radius direction. To calculate the temperature profile inside the particle, the Fourier differential equation should be solved and this requires a lot of effort. In the industrial practice, however, an assumed homogeneous average temperature (calorific temperature) is often more preferred, to make the energy balance easier. For this purposes the modified heat transfer coefficient, α_κ , is introduced by Jeschar [12]:

$$\alpha_\kappa \cdot A_S \cdot (T_G - T_M) = \alpha \cdot A_S \cdot (T_G - T_S) \quad (3.15)$$

where A_S is the surface area of the particle,

T_G the gas temperature in ambience,

T_M the calorific mean temperature of particle,

T_S the surface temperature of the particles,

and α_κ the modified heat transfer coefficient is then expressed as:

$$\alpha_\kappa = \frac{1}{\frac{1}{\alpha} + \frac{d}{2 \cdot \kappa \cdot \lambda}} \quad (3.16)$$

where λ is the thermal conductivity of the solid particle,
and κ the transient factor.

At constant ambient temperature the transient factor for spherical particle is calculated with the equation:

$$\kappa = \left(5 - \frac{\pi^2}{3} \right) \cdot \left[\frac{1}{2} - \frac{1}{\pi} \cdot \arctan \left(\ln \frac{2 \cdot Bi}{3 + 4} \right) \right] + \frac{\pi^2}{3} \quad (3.17)$$

where Bi is the Biot number and can be calculated by:

$$Bi = \frac{\alpha \cdot d}{\lambda} \quad (3.18)$$

3.3 Determination of mass transfer coefficient

In simulation of earth alkali decomposition, the convective mass transfer of produced CO_2 into the gaseous ambience must be calculated. With analogy to heat transfer, the mass transfer coefficient of CO_2 from a single limestone solid surface to the ambient, β , can be calculated from Sherwood function.

The Sherwood function for a single sphere in a laminar flow is given as:

$$Sh_{lam} = 0.644 \cdot Re^{\frac{1}{2}} \cdot Sc^{\frac{1}{3}} \quad (3.19)$$

The Sherwood function for a single sphere in a laminar flow is given as:

$$Sh_{turb} = \frac{0.037 \cdot Re^{0.8} \cdot Sc}{1 + 2.443 \cdot Re^{-0.1} \cdot (Sc^{0.667} - 1)} \quad (3.20)$$

The Sherwood function for a single sphere can be averaged from above two values:

$$Sh_S = 2 + (Sh_{lam}^2 + Sh_{turb}^2)^{0.5} \quad (3.21)$$

where Schmidt number is calculated by:

$$Sc_s = \frac{\nu}{D_{CO_2-Gas}} \quad (3.22)$$

where the binary diffusivity of CO₂ in air can be approximately taken for the binary diffusivity of CO₂ in combustion gas:

$$D_{CO_2-Gas} \approx D_{CO_2-Air} = D_{CO_2-Air0} \cdot \left(\frac{T}{T_0}\right)^{1.75} \quad (3.23)$$

where T₀ is reference temperature of 273K,

D_{CO₂-Air0} the binary diffusivity of CO₂ in air at above reference temperature,

and D_{CO₂-Air} the binary diffusivity of CO₂ in air at temperature T.

Similarly to heat transfer, the mass transfer coefficient of CO₂ in the packed bed can be obtained by modification of the mass transfer for single sphere, with the same factor f_ψ as in Equation (3.9):

$$Sh = f_{\psi} \cdot Sh_S \quad (3.24)$$

Then the mass transfer coefficient of CO₂, β, is obtained from:

$$\beta = \frac{Sh \cdot D_{CO_2-Air}}{d} \quad (3.25)$$

3.4 Drying

The drying of wet solid particles by a hot gas is normally a kinetic-controlled process. Assuming that the heat transfer is mainly due to convection, and both phases are plug flow with homogeneous material property and temperature at input, a mathematical model can be established. Actually, the overall kinetics of convective drying is determined not only by the gas phase, but also by the transport phenomena in particle phase. The concept of the normalized drying curve of the single particle is introduced to capture all influence of such transport phenomena, which is considered as an established standard.

Figure 3.1 shows a drying curve of a single particle of two different solid. With the same diameter and under the same ambient condition, both particles have the same drying rate during the first drying stage. In this stage, the solid surface is sufficiently wet, so that each particle dries just like a drop of pure water of the same size. But in the second (falling rate) drying stage, which starts from the critical moisture content, the drying rate is different, due to the particle-side transport phenomena (capillarity, diffusion, etc.). These phenomena, depending on the internal particle structure, are rate-controlling in the second stage. In this figure, solid B is obviously easier to dry than solid A.

After having been crashed, the limestone particles will be washed by water to eliminate the clay. Therefore the particles are somewhat wet (with moisture content of about 1.1%) before they enter the grate. For simplicity, only the first drying stage is considered in the program LEPOL. It is assumed, that the drying of wet limestone particles by a hot gas is a heat-transfer-controlled process with the equation:

$$\dot{M} = \frac{\alpha \cdot A \cdot (T_G - T_S)}{h_{VAP}} \quad (3.26)$$

where h_{VAP} is the evaporation enthalpy of water.

3.5 Equivalent particle diameter

The real limestone particles, or clinker pellets, are irregular and never have a perfect spherical form. But their similarity to a sphere, or the degree to which a real particle shape approaches a sphere, can be generally described by an index of sphericity. Sphericity is defined as the relation to each other of the various diameters (length, width and thickness) of a particle; specifically the degree to which the shape of a real particle approaches that of a sphere. Sphericity could be thought of as the degree of equality of the three axes of a particle where in a perfect sphere the length, width and thickness are all equal.

Quantitatively sphericity may be expressed as following according to Wadell [13]:

$$\Psi_w = \sqrt[3]{\frac{V_p}{V_{CS}}} \quad (3.27)$$

where V_p is the volume of a particle determined by immersion in a fluid, and V_{CS} the volume of a circumscribing sphere which may be taken as the volume of a sphere with a diameter equal to the long axis of the particle.

For most particles, the Wadell sphericity can be approximated by following ratio:

$$\Psi_w \approx \frac{A_s}{A_p} \quad (3.28)$$

where, A_s is the surface area of a sphere of the same volume as the real particle, and A_p the volume of the real particle.

As the sphere with the same volume has the smallest surface area, the Wadell sphericity is always smaller than 1. Its reciprocal value is called particle form factor. In the lime industry, a widely adopted statistical value of Wadell sphericity of the limestone particles after crashing is 0.832. The particle form factor is therefore about 1.20.

Making things more complicated, the size of real limestone particles is a distribution after crashing. In lime industry, the particles are sieved to obtain an appropriate range of particle size. To show how to estimate a representing equivalent diameter for real particles with size distribution, a sieve analysis must be done for a batch of input limestone particles, which is intercepted just in front of the pre-heating grate. In this sieve analysis, a serial of 10 sieves with the mesh size from 3.15 to 70mm size is used. A typical analysis result is listed in Table 3.1.

Table 3.1 Sieve analysis of limestone particles

i	X_i (mm)	$\frac{V_i}{V}$ (-)	\bar{X}_i (mm)
1	< 3.15	0.001	1.575
2	3.15 - 8.00	0.001	5.575
3	8.00 - 11.20	0	9.600
4	11.20 - 16.0	0	13.600
5	16.00 - 22.40	0.009	19.200
6	22.40 - 31.50	0.200	26.950
7	31.50 - 45.00	0.439	38.250
8	45.00 - 56.00	0.180	50.5
9	56.00 - 63.00	0.125	59.500
10	63.00 - 70.00	0.045	66.500
11	> 70.00	0	

To facilitate the computation, the real form of particles must be regarded as sphere with an equivalent diameter. The Sauter mean diameter of this representing sphere is calculated by:

$$d_s = \sum_{i=1}^I \left(\frac{V_i}{V} \cdot \frac{1}{\bar{X}_i} \right)^{-1} \quad (3.29)$$

which gives 37.7 mm, if all the particles are spheres.

The Sauter mean diameter can be obtained from modifying d_s by the form factor f :

$$d = \frac{d_s}{f} \quad (3.30)$$

Taking the form factor as 1.2, then the Sauter mean diameter of the representing sphere is then 31.4 mm.

3.6 Void fraction of particle bed

The stone bed on a moving grate can be treated as a packed bed with the upward-flow of hot gases passing crossing current of solid particles. The void fraction of the particle bed can be calculated from the real density of the particles and the apparent or bulk density of the particle bed:

$$\Psi = 1 - \frac{\rho_P}{\rho_B} \quad (3.31)$$

where ρ_P is the real density of the particle,
 ρ_B the apparent or bulk density of the particle bed.

Void fraction of a packed bed can be influenced by method of packing (random or regular, loose or dense), particle shape (sphere, cylinder etc.) and particle size distribution.

For infinitely extended, regular packing of equally sized, large spheres the void fraction is:

0.476 for simple cubic packing;
 0.395 for cubic space centred packing;
 and 0.259 for cubic face centred packing.

For random packing of equally sized, large spheres the void fraction is:

0.4 - 0.42 for loose packing,
 0.36 - 0.38 for dense packing.

For a size distribution in a particle bed, the apparent or bulk density does not depend on the average particle size, but much on the width of the particle size distribution, which is characterized for example by the ratio between the maximum and minimum size. The more closely or sharply the particle size distributes, the lower is the bulk density.

As an example, the limestone size distribution shown in Table 3.1 has a measured apparent bed density of about 1500 kg/m³. The real density of a not-porous limestone with high CaCO₃ content amounts to 2700 kg/m³. So the void fraction is then 0.44. In another operation mode in the industry, the limestone particles after crashing are separated again into two size fractions, the equivalent diameters are 8.8 mm and 22.3 mm, respectively, and the void fractions are correspondingly bigger, namely 0.48.

3.7 Pressure drop in particle bed

Pressure drop can be described with two different ways: based on hydraulic diameter or based on one particle cross-flow.

3.7.1 Based on a hydraulic diameter

Flow through a packed bed can be regarded as fluid flow past some number of submerged objects. The hydraulic diameter is defined:

$$d_H = \frac{V_H}{A_H} = \frac{\Psi}{O} \quad (3.32)$$

where V_H is the volume in a packed bed which is available for flow,
 A_H the wetted surface in the packed bed,

and O the specific surface of packed bed, which can be calculated from the specific surface of a single particle in the bed:

$$O = \frac{A_p}{V_p} \cdot (1 - \psi) \quad (3.33)$$

The Ergun equation is based on the model conception that the real packed bed can be replaced by a parallel connection of flow channels, and the pressure drop calculation is similar to the one phase pipe flow, however with the hydraulic diameter of the packed bed as characteristic dimension.

The pressure drop across the packed bed can be obtained from the equation according to Ergun [14]:

$$\frac{\Delta P}{\Delta L} = 150 \cdot \frac{(1 - \Psi)^2}{\Psi^3} \cdot \frac{\nu \cdot \rho_F \cdot w}{d^2} + 1.75 \cdot \frac{1 - \Psi}{\Psi^3} \cdot \frac{\rho_F \cdot w^2}{d} \quad (3.34)$$

where w is the empty tube velocity in the bed if no packing were present, and d the Sauter mean diameter described before.

This equation tells the pressure drop along the length of the packed bed for a given fluid velocity. It also tells that the pressure drop depends on the packing size, length of bed, fluid viscosity and fluid density. The first term of this equation describes the change in pressure under viscous flow while the second one accounts for change in pressure at turbulent flow (kinematic energy loss). The constants are based on experimental data for many shapes of particles, but the equation is most accurate for spherical particles. The Ergun equation was designed for fluid flow up to the fluidization point.

For the pressure drop in packed bed, consisting of spherical particles, another equation obtained by Brauer [15] can be applied, which is similar to Ergun equation:

$$\frac{\Delta P}{\Delta L} = 160 \cdot \frac{(1 - \Psi)^2}{\Psi^3} \cdot \frac{\eta \cdot w}{d^2} + 3.1 \cdot \frac{1 - \Psi}{\Psi^3} \cdot \frac{\rho_F \cdot w^2}{d^2} \cdot \left[\frac{\eta \cdot (1 - \Psi)}{\rho_F \cdot w \cdot d} \right]^{0.1} \quad (3.35)$$

Brauer's correlation is based on experimental data and applies to a packed bed, consisting of spherical particles of the same diameter. Therefore in this case the Sauter mean diameter is equal to the sphere diameter. For the calculation of a pressure drop for a bed consisting of spherical particles of different size, appropriate correction functions have to be considered.

3.7.2 Based on particle cross flow

This model, created by Molerus [16], is based on a flow over a single particle. When the particles are overflowed by a fluid a resistance force W is exerted on each particle. Depending on a number of particles n in a packed bed a resistance $z \cdot W$ is exerted on a bed, which is balanced by the pressure:

$$N \cdot W = \Delta p \cdot A \quad (3.36)$$

The number of particles in a bed can be obtained from the mass balance. It is equal to the ratio of the volume of solid to the volume of a single particle with Sauter mean diameter d :

$$N = \frac{(1 - \Psi) \cdot A \cdot \Delta L}{d^3 \cdot \frac{\pi}{6}} \quad (3.37)$$

From the above mentioned equations results the pressure drop:

$$W = \frac{\Delta P}{\Delta L} \cdot \frac{d^3}{6} \cdot \frac{1}{1 - \Psi} \quad (3.38)$$

The dimensionless form is:

$$Eu = \frac{4}{3} \cdot \frac{\Delta P}{\rho_F \cdot w^2} \cdot \frac{d}{\Delta L} \cdot \frac{\Psi^2}{1 - \Psi} \quad (3.39)$$

The analysis of a cross-flow of single particle in the packed bed with the help of Navier-Stokes equation and the experimental data results in the equation for the Euler number. For the spherical particles, according to Molerus [17] and Schweinzer [18]:

$$Eu = \frac{24}{Re} \cdot \left\{ 1 + 0.692 \cdot \left[\frac{r_0}{\delta} + 0.5 \cdot \left(\frac{r_0}{\delta} \right)^2 \right] \right\} + \frac{4}{\sqrt{Re}} \cdot \left[1 + 0.12 \cdot \left(\frac{r_0}{\delta} \right)^{1.5} \right] + \left(0.4 + 0.891 \cdot \frac{r_0}{\delta} \cdot Re^{-0.1} \right) \quad (3.40)$$

with

$$\frac{r_0}{\delta} = \left(\frac{0.95}{\sqrt[3]{1 - \Psi}} - 1 \right)^{-1} \quad (3.41)$$

and

$$Re = \frac{w \cdot d}{\Psi \cdot \nu} \quad (3.42)$$

Bes [11] has compared the pressure drops calculated with two methods described above. The calculations were done for the void fraction 0.4 and air of 600°C as a gas. The pressure drop in a packed bed increases for the higher superficial velocities. It is inversely proportional to the particle diameter. For a superficial velocity of about 1m/s, the pressure drop is twice as big for particles of 0.04m diameter as for the particles of 0.08m.

3.8 Fluidisation of particles

3.8.1 Principle of the fluidization of solid particle

The fluidisation phenomena of solid particles can be explained with Figure 3.2 in VDI-Wärmeatlas [3]. It shows different behaviours of solid particles in a packed bed which is blown by an upwards fluid from the bottom with an increasing flow velocity.

When the fluid flows with a limited velocity, it penetrates the packed bed only through the void channels and does not change the solid structure in the bed (Figure 3.2 a). In this case the void fraction is the same as that of packed bed.

With an increased fluid velocity, a larger upwards force is exerted upon the particles. As a result of it, some particles will begin to move in a limited area. The most particles, however, will stay at their fixed position and contact with each other. As the fluid velocity increases further, a state can be reached that all the particles begin to suspend without permanent contact (Figure 3.2 b). In this state the pressure drop between the top and the bottom surface of the bed is balanced exactly by the weight of solid and fluid in the bed. In this case, the so-called loosing point is reached. The void fraction at this point is somewhat larger than that of packed bed. The corresponding empty tube velocity of fluid in this state is then minimal fluidisation velocity.

With a further increased fluid throughput, fluidized beds with gas or liquid show different behaviours. A liquid-solid fluidized bed reacts to a throughput increase with a homogeneous expansion, while in a gas-solid fluidized bed the gas phase passes through the bed essentially in the form of solid-free bubbles (Figure 3.2 c). The gas bubbles grow mainly by coalescence during the ascent.

If the apparatus is slim and high, the gas bubbles can occupy finally the entire cross section and behave as gas pistons (Figure 3.2 d).

In a gas-solid fluidized bed, if the gas velocity exceeds the velocity with which the solid particles sink, the particles will be blown out of the apparatus. The phenomena of gas bubble formation and a clear bed surface will disappear due to the high void fraction. Because of the high solid lost these fluidized beds can be maintained only by constant circulation of the solid via a feedback cyclone (Figure 3.2 e).

3.8.2 Minimal fluidisation velocity

At the loosing point, which is also called fluidisation point, the empty tube velocity of the fluid is exactly so large that the solid particle in the packed bed can begin to move to each other. This characteristic gas velocity is then called minimal fluidisation velocity. If the fluid velocity is smaller than this velocity, then the particles are fixed in their position by gravity. With a bigger fluid velocity, a fluidisation state is established. Normally this minimal fluidisation velocity for different particles can be measured experimentally.

The minimal fluidisation velocity should be determined experimentally if possible. It should always be determined for the operating condition, which can deviate possibly substantially from refilling due to fine property discharge, dye and/or grain growth or contraction with chemical reaction.

For the force balance:

$$\Delta P \cdot A = \rho_s \cdot (1 - \Psi) \cdot g \cdot A \cdot \Delta L + \rho_F \cdot \Psi \cdot g \cdot A \cdot \Delta L \quad (3.43)$$

$$\frac{\Delta P}{\Delta L} = 150 \cdot \frac{(1 - \Psi)^2}{\Psi^3} \cdot \frac{\rho_F \cdot v \cdot w}{d^2} + 1.75 \cdot \frac{1 - \Psi}{\Psi^3} \cdot \frac{\rho_F \cdot w^2}{d} \quad (3.44)$$

Then the minimal fluidisation velocity can be calculated as:

$$w_{MF} = \sqrt{\frac{1840 \cdot (1 - \Psi)^2 \cdot v^2}{d^2} + \frac{0.571 \cdot \Psi^3 \cdot d \cdot g \cdot [\rho_s \cdot (1 - \Psi) + \rho_F \cdot \Psi]}{(1 - \Psi) \cdot \rho_F}} - \frac{42.9 \cdot (1 - \Psi) \cdot v}{d} \quad (3.45)$$

A simple correlation to determine the minimal fluidisation velocity without knowing the loosing porosity is given by Wen and Yu [19]:

$$\text{Re}_{MF} = 33.7 \cdot \left(\sqrt{1 + 3.6 \cdot 10^{-5} \cdot \text{Ar}} - 1 \right) \quad (3.46)$$

where Ar is the Archimedes number for solid particles:

$$\text{Ar} = \frac{(\rho_s - \rho_F) \cdot g \cdot d^3}{\rho_F \cdot v^2} \quad (3.47)$$

From the Reynolds number at the point of loosening:

$$\text{Re}_{MF} = \frac{w_{MF} \cdot d}{v} \quad (3.48)$$

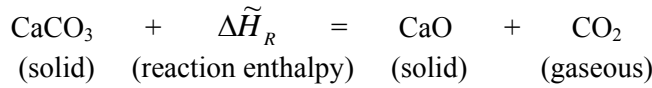
the minimal fluidization velocity, w_{MF} , can be obtained.

The comparison between the two methods shows no substantial deviation. Figure 3.3 shows concrete values of minimal fluidisation velocity for clinker particles, which is blown by cooling air flow. Smaller particles are easier to be fluidized. A higher velocity for air is required for fluidisation if the air is warmer and has correspondingly smaller density. The minimal fluidisation velocities are about 2.9 m/s with cold air of 20°C, and 6.2 m/s with hot air of 1400°C respectively for the small clinker particle with diameter of 10mm, as an example.

3.9 Decomposition of earth alkali

3.9.1 Decomposition model of limestone

The decomposition of limestone is an endothermic topochemical reaction:



The calcination process can be explained using a partially decomposed piece of carbonate, whose profiles of CO₂ partial pressure and temperature are shown in Figure 3.4. The specimen comprises a dense carbonate core surrounded by a porous oxide layer. In the calcination reactor at temperature T_A heat is transferred by radiation and convection (symbolized by α) to the solid surface at a temperature of T_S. By means of thermal conduction (λ) heat penetrates through the porous oxide layer at an average temperature of T_{OX} to reach the reaction front, where the temperature is T_F. As the reaction enthalpy is many times greater than the internal energy, the heat flowing further into the core is negligible during reaction. Therefore the core temperature is only slightly lower than the front temperature. Once heat is supplied, the chemical reaction (k) then takes place, for which the driving force is the deviation of CO₂ partial pressure from the equilibrium (P_{eq0}-P_F). The released CO₂ diffuses (D^P) through the porous oxide layer to the surface and finally passes by convection (β) to the surroundings where the CO₂ partial pressure P_A exists.

The four physical transport processes and the chemical kinetics involved are therefore interconnected. The resistances caused by heat transfer, heat conduction, chemical kinetics, pore diffusion and mass transfer can be understood with analogue to serial electrical resistances, R_α, R_λ, R_k, R_D and R_β in causal sequence.

A one-dimensional shrinking core model can be established based on the assumptions of ideal sample geometry such as sphere, cylinder or plate, a homogeneous chemical composition and structure in the sample, and a symmetrical heat supply. The reaction starts uniformly on the solid surface, always forming a smooth reaction front, which then advances continuously into the interior. This fact has been partly proven with SEM (scanning electron microscopic) by Fuertes et al. [20] and Rähler [21]. The edges of the individual crystals are the preferred locations where the reaction starts. Therefore the actual reaction surface is, as demonstrated by Fuertes et al. [20], somewhat larger than the assumed smooth surface. This deviation has been incorporated in the reaction rate coefficient in this research. Based on the shrinking core model, Szekely et al. [22] and Kainer et al. [23] have derived analytical equations to calculate the decomposition of spherical and cylindrical limestone pieces. Assuming a pseudo steady state and constant material properties, Equation (3.49) is obtained (for spherical geometry, for example) by combining the heat transfer at the particle surface and the heat conduction in the lime layer:

$$\dot{q} = \frac{\lambda}{r_F^2 \cdot \left(\frac{1}{r_F} - \frac{1}{r_S} + \frac{\lambda}{\alpha \cdot r_S^2} \right)} \cdot (T_G - T_F), \quad (3.49)$$

where α accounts for both the convection and the radiation heat transfer.

Similarly, Equation (3.50) is derived (for spherical geometry, for example) by combining the mass transfer of CO₂ at the particle surface and the diffusion in the lime layer:

$$\dot{m} = \frac{D^P}{r_F^2 \cdot \left(\frac{1}{r_F} - \frac{1}{r_S} + \frac{D^P}{\beta \cdot r_S^2} \right)} \cdot \frac{1}{R_{CO_2}} \cdot \left(\frac{P_F}{T_F} - \frac{P_G}{T_G} \right). \quad (3.50)$$

For the reaction at the front, the reaction rate is proportional to the deviation of partial pressure from equilibrium, P_{eq}-P_F:

$$\dot{m} = \frac{k}{R_{CO_2} \cdot T_F} \cdot (P_{eq} - P_F). \quad (3.51)$$

The heat flux and mass flux are related by:

$$\dot{q} = \Delta h_{CO_2} \cdot \dot{m}, \quad (3.52)$$

where Δh_{CO_2} is the specific reaction enthalpy corresponding to the produced CO_2 in mass, 3820 kJ/kg.

The mass flux of CO_2 is expressed as:

$$\dot{m} = -K_{CO_2} \cdot \frac{dr_F}{dt}, \quad (3.53)$$

where K_{CO_2} is the concentration of CO_2 in limestone, e.g. 1190 kg/m³ for a pure limestone with a density of about 2700 kg/m³.

The conversion degree X is calculated by:

$$X = \frac{M}{M_{t=0}} = 1 - \left(\frac{r_F}{r_S} \right)^b, \quad (3.54)$$

where the shape factor $b = 1, 2$ or 3 for a plate, cylinder or sphere respectively.

Two coupled differential equations for the conversion degree and the decomposition temperature can be then derived from the above system:

$$\frac{dX}{dt} \cdot [R_\alpha + R_\lambda \cdot f_1(X)] = 1, \quad (3.55)$$

$$\frac{dT}{dt} \cdot [R_\beta + R_D \cdot f_1(X) + R_k \cdot f_2(X)] = 1, \quad (3.56)$$

where the form functions $f_1(X)$ and $f_2(X)$ are summarized in Table 3.2.

Table 3.2 Form functions for different geometries

f	plate	cylinder	sphere
$f_1(X)$	$f_1(X) = 2 \cdot X$	$f_1(X) = 2 \cdot \ln(1 - X)^{-1/3}$	$f_1(X) = 2 \cdot \left[(1 - X)^{-1/3} - 1 \right]$
$f_2(X)$	$f_2(A) = 1$	$f_2(A) = \frac{1}{2} \cdot (1 - X)^{-1/2}$	$f_2(A) = \frac{1}{3} \cdot (1 - X)^{-2/3}$

The resistances R_i , where T_F is included, are given in following equations:

$$R_\alpha = \frac{K_{CO_2} \cdot \Delta h_{CO_2} \cdot r_S}{T_G - T_F} \cdot \frac{r_S}{\alpha \cdot b}, \quad (3.57)$$

$$R_\lambda = \frac{K_{CO_2} \cdot \Delta h_{CO_2} \cdot r_S^2}{T_G - T_F} \cdot \frac{r_S^2}{2 \cdot \lambda \cdot b}, \quad (3.58)$$

$$R_k = \frac{K_{CO_2} \cdot R_{CO_2} \cdot T_F \cdot r_S}{P_{eq} - P_G} \cdot \frac{r_S}{k}, \quad (3.59)$$

$$R_D = \frac{K_{CO_2} \cdot R_{CO_2} \cdot T_F \cdot r_S^2}{P_{eq} - P_G} \cdot \frac{r_S^2}{2 \cdot D^p \cdot b}, \quad (3.60)$$

$$R_\beta = \frac{K_{CO_2} \cdot R_{CO_2} \cdot T_F \cdot r_S}{P_{eq} - P_G} \cdot \frac{r_S}{\beta \cdot b}. \quad (3.61)$$

To supplement the above equation system, the dependence of equilibrium pressure upon the temperature is described thermodynamically by:

$$P_{eq} = P_{eq0} \cdot \exp\left(-\frac{\Delta \tilde{H}_R}{\tilde{R} \cdot T_F}\right), \quad (3.62)$$

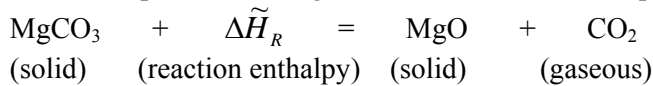
where P_{eq0} is $2.15 \cdot 10^7$ bar and $\Delta \tilde{H}_R$ 168 kJ/mol. There is no discernible dependence of the equilibrium pressure upon the genesis and nature of the limestone concerned.

With the Equations (3.55) to (3.62), X and T_F can be calculated as function of time t .

3.9.2 Decomposition model of magnesite

The alkaline earth carbonate magnesite ($MgCO_3$) is an important raw material for many branches of industry. Like limestone, a great part of the natural carbonate rock is burnt in different kinds of reactors before its final utilisation. In this treatment the decomposition of the carbonate takes place with a high input of energy, with splitting-off of CO_2 , to yield the magnesium oxide (MgO), which is used as reactant in the building industry, as for example for flooring plaster, in the ceramic industry for the production of refractory building materials, as well as for high quality ceramics and for pollution control.

The decomposition of magnesite is an endothermic topochemical reaction:



The decomposition of magnesite can be simulated with the same mathematical model for calcite decomposition, when the corresponding constants are used:

The reaction enthalpy $\Delta\tilde{H}_R$ 117 kJ/mol, or regarding to the mass of produced CO_2 , the specific reaction enthalpy Δh_{CO_2} is 2645 kJ/kg.

The concentration of CO_2 in magnesite, K_{CO_2} , is 1326 kg/m³ for a pure magnesite with a density of about 2540 kg/m³.

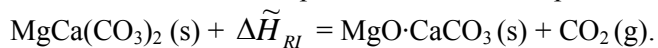
For calculation of equilibrium partial pressure, the constant P_{eq0} is $2.7 \cdot 10^8$ bar.

3.9.3 Decomposition model of dolomite

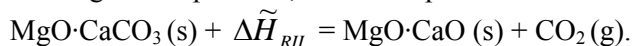
Dolomite, which is normally equal molar salt of calcite and magnesite, $MgCa(CO_3)_2$, is an important natural raw material in many branches of industry. Before final utilization, dolomite must be calcinated in shaft or rotary kilns, splitting off CO_2 to yield oxides, which can be used, for example, in construction, in metallurgy, and as a flue gas desulphurising agent. The decomposition mechanism of dolomite depends mainly upon the CO_2 partial pressure in ambience. Under a lower pressure about under $2.7 \cdot 10^4$ Pa (200 Torr), accordingg to Bandi and Krapf [24], a simultaneous decomposition takes place:



Under a higher CO_2 pressure, dolomite dissociates sequently in two stages. As the equilibrium decomposition pressure for $MgCO_3$ is lower than that for $CaCO_3$, $MgCO_3$ component will begin to dissociate at a lower temperature while decomposition of $CaCO_3$ component is still prohibited:



At a higher temperature, the decomposition of $CaCO_3$ component follows:



In the two-stage decomposition, the different products can be obtained as half-bunt oxides ($MgO \cdot CaCO_3$) or completely decomposed oxides ($MgO \cdot CaO$), by controlling the operation parameter in kiln like gas temperature, fuel type, and residence time.

Independent of the ambient partial pressure, the general decomposition process can be described by a uniform model, similar to the derivation of the shrinking-core-model for limestone decomposition.

The calcination process can be explained using a partially decomposed piece of dolomite with two separate reaction fronts, which are progressing towards the particle centre with different velocities. The profiles of CO₂ partial pressure and temperature are shown in Figure 3.5. At the first front at r_{FI} the MgCO₃ decomposition takes place, and at the second front at r_{FII} the CaCO₃ dissociation follows. The specimen comprises a dense dolomite core (MgCa(CO₃)₂) in the range of $r < r_{FI}$. Between the two fronts $r_{FI} < r < r_{FII}$ a somewhat porous layer of half-burnt dolomite (MgO·CaCO₃) exists. The out layer when $r > r_{FII}$ consists of more porous final decomposed product (MgO·CaO).

In the calcination reactor at temperature T_G heat is transferred by radiation and convection (symbolized by α) to the particle surface at a temperature of T_S . By means of thermal conduction (λ_{II}) heat penetrates through the porous oxide layer II with an average temperature of T_{OXII} to reach the reaction front II with a temperature T_{FII} . Part of the heat will be consumed at reaction II; the rest will penetrate the porous half-burnt oxide layer I with an average temperature of T_{OXI} by means of thermal conduction (λ_I) to reach reaction front I at temperature T_{FI} . As the reaction enthalpy is many times greater than the internal energy, the heat flowing further into the core is negligible during reaction. Therefore the core temperature is only slightly lower than the front temperature T_{FI} .

At front I the chemical reaction I (k_I) of MgCO₃ decomposition takes place, for which the driving force is the deviation of CO₂ partial pressure from the equilibrium ($P_{eq,FI} - P_{FI}$).

The released CO₂ diffuses (D^P_I) through the porous half-burnt oxide layer I to the second front II. At the front II the reaction II (k_{II}) of CaCO₃ decomposition takes place, for which the driving force is the deviation of CO₂ partial pressure from the equilibrium ($P_{eq,FII} - P_{FII}$). The CO₂ produced at both fronts diffuses (D^P_{II}) through the porous oxide layer II to the particle surface, and finally passes by convection (β) to the surroundings, where the CO₂ partial pressure P_G exists.

Regarding to reaction I, 7 resistances in serial can be formulated for the physical heat and mass transport processes, and the chemical kinetics involved, namely: $R_{\alpha,I}$, $R_{\lambda_{II,I}}$, R_{λ_I} , R_{k_I} , $R_{D,I}$, $R_{D_{II,I}}$ and $R_{\beta,I}$ for effective thermal convection, thermal conduction in layer II, thermal conduction in layer I, reaction kinetics at front I, mass diffusion in layer I, mass diffusion in layer II and mass convection to ambience. Similarly for reaction II, 5 resistances in serial are $R_{\alpha,II}$, $R_{\lambda_{II,II}}$, $R_{k_{II}}$, $R_{D_{II,II}}$ and $R_{\beta,II}$, corresponding to the effective thermal convection, thermal conduction in layer II, reaction kinetics at front II, mass diffusion in layer II and mass convection to the surrounding.

Assuming that both the two reaction fronts are smooth sharp interfaces, which advance continuously into the interior, a one dimensional model can be established for a sample with an ideal geometry, such as sphere, long cylinder or plate.

Taking a spherical sample with radius of r_S as example, the heat required by both MgCO₃ and CaCO₃ decompositions, \dot{Q}_I and \dot{Q}_{II} respectively, come from the ambient hot by effective convection heat transfer:

$$\dot{Q}_I + \dot{Q}_{II} = \alpha \cdot A_S \cdot (T_G - T_S) \quad (3.63)$$

The heat is conducted from particle surface to the reaction front II of CaCO₃ decomposition, through completely decomposed oxide layer:

$$\dot{Q}_I + \dot{Q}_{II} = \frac{\lambda_{II} \cdot A_S \cdot (T_S - T_{FII})}{r_S \cdot \left(\frac{r_S}{r_{FII}} - 1 \right)} \quad (3.64)$$

The heat for MgCO₃ decomposition should be supplied to the reaction front I by conduction through half-burnt oxide layer:

$$Q_I = \frac{\lambda_I \cdot A_{FII} \cdot (T_{FII} - T_{FI})}{r_{FII} \cdot \left(\frac{r_{FII}}{r_{FI}} - 1 \right)} \quad (3.65)$$

The reaction rate of MgCO_3 decomposition at the front I is proportional to the deviation of CO_2 partial pressure from the equilibrium:

$$\dot{M}_I = k_I \cdot A_{FI} \cdot \left(\frac{P_{eq,FI} \cdot \tilde{M}_{CO_2}}{\tilde{R} \cdot T_{FI}} - \frac{P_{FI} \cdot \tilde{M}_{CO_2}}{\tilde{R} \cdot T_{FI}} \right) \quad (3.66)$$

The produced CO_2 from MgCO_3 decomposition passes through the half-burnt oxide layer to reach the reaction front II through pore diffusion:

$$\dot{M}_I = \frac{D^P_I \cdot A_{FII}}{r_{FII} \cdot \left(\frac{r_{FII}}{r_{FI}} - 1 \right)} \cdot \left(\frac{P_{FI} \cdot \tilde{M}_{CO_2}}{\tilde{R} \cdot T_{FI}} - \frac{P_{FII} \cdot \tilde{M}_{CO_2}}{\tilde{R} \cdot T_{FII}} \right) \quad (3.67)$$

Similarly, the reaction of CaCO_3 decomposition on the reaction front II is driven by the deviation of CO_2 pressure from the equilibrium:

$$\dot{M}_{II} = k_{II} \cdot A_{FII} \cdot \left(\frac{P_{eq,FII} \cdot \tilde{M}_{CO_2}}{\tilde{R} \cdot T_{FII}} - \frac{P_{FII} \cdot \tilde{M}_{CO_2}}{\tilde{R} \cdot T_{FII}} \right) \quad (3.68)$$

Both parts of produced CO_2 mass should pass through the completely decomposed oxide layer to reach the particle surface by pore diffusion:

$$\dot{M}_I + \dot{M}_{II} = \frac{D^P_{II} \cdot A_S}{r_S \cdot \left(\frac{r_S}{r_{FII}} - 1 \right)} \cdot \left(\frac{P_{FII} \cdot \tilde{M}_{CO_2}}{\tilde{R} \cdot T_{FII}} - \frac{P_S \cdot \tilde{M}_{CO_2}}{\tilde{R} \cdot T_S} \right) \quad (3.69)$$

Both parts of produced CO_2 mass should be transported to ambience by convection:

$$\dot{M}_I + \dot{M}_{II} = \beta \cdot A_S \cdot \left(\frac{P_S \cdot \tilde{M}_{CO_2}}{\tilde{R} \cdot T_S} - \frac{P_G \cdot \tilde{M}_{CO_2}}{\tilde{R} \cdot T_G} \right) \quad (3.70)$$

The mass and heat is coupled by the two reaction enthalpies:

$$\dot{Q}_I = \frac{\dot{M}_I \cdot \Delta \tilde{H}_{RI}}{\tilde{M}_{CO_2}} \quad (3.71)$$

$$\dot{Q}_{II} = \frac{\dot{M}_{II} \cdot \Delta \tilde{H}_{RII}}{\tilde{M}_{CO_2}} \quad (3.72)$$

The equilibrium pressures of CO_2 in both reactions are temperature dependent:

$$P_{eq,FI} = P_{eq0,I} \cdot \exp\left(-\frac{\Delta \tilde{H}_{RI}}{\tilde{R} \cdot T_{FI}}\right) \quad (3.73)$$

$$P_{eq,FII} = P_{eq0,II} \cdot \exp\left(-\frac{\Delta \tilde{H}_{RII}}{\tilde{R} \cdot T_{FII}}\right) \quad (3.74)$$

where $\Delta \tilde{H}_{RI}$ is 117 kJ/mol for MgCO_3 decomposition, corresponding to 2660 kJ/(kg CO_2), and $\Delta \tilde{H}_{RII}$ 168 kJ/mol for CaCO_3 decomposition, corresponding to 3800 kJ/(kg CO_2).

The mass flows of CO₂ are related with the conversion velocities of both components, MgCO₃ and CaCO₃:

$$\dot{M}_I = \frac{1}{3} \cdot K_{CO2I} \cdot A_{FI} \cdot r_S \cdot (1 - X_I)^{\frac{2}{3}} \cdot \frac{dX_I}{dt} \quad (3.75)$$

$$\dot{M}_{II} = \frac{1}{3} \cdot K_{CO2II} \cdot A_{FII} \cdot r_S \cdot (1 - X_{II})^{\frac{2}{3}} \cdot \frac{dX_{II}}{dt} \quad (3.76)$$

where K_{CO2I} and K_{CO2II} are CO₂ concentrations, which are contained in component MgCO₃ and CaCO₃ respectively. For a typical pure dolomite with a density of 2840 kg/m³, K_{CO2I} = K_{CO2II} = 678 kgCO₂/m³. This value will be referred as K_{CO2} in further discussion.

Some subsidiary geometric relations are obvious:

$$A_S = 4\pi \cdot r_S^2 \quad (3.77)$$

$$A_{FI} = 4\pi \cdot r_{FI}^2 \quad (3.78)$$

$$A_{FII} = 4\pi \cdot r_{FII}^2 \quad (3.79)$$

$$r_{FI} = (1 - X_I)^{\frac{1}{3}} \cdot r_S \quad (3.80)$$

$$r_{FII} = (1 - X_{II})^{\frac{1}{3}} \cdot r_S \quad (3.81)$$

Four coupled differential equations for the conversion velocities of MgCO₃ and CaCO₃ ($\frac{dX_I}{dt}$ and $\frac{dX_{II}}{dt}$) and the decomposition temperature (T_{FI} and T_{FII}) can be then derived from the above system:

$$\frac{T_G - T_{FII}}{K_{CO2}} = \frac{dX_I}{dt} [R_{\alpha,I} \cdot f_1 + R_{\lambda_{III,I}} \cdot f_2(X_{II})] + \frac{dX_{II}}{dt} [R_{\alpha,II} \cdot f_1 + R_{\lambda_{III,II}} \cdot f_2(X_{II})] \quad (3.82)$$

$$\frac{T_{FII} - T_{FI}}{K_{CO2}} = \frac{dX_I}{dt} \cdot R_{\lambda_I} \cdot [f_2(X_I) - f_2(X_{II})] \quad (3.83)$$

$$\left(\frac{P_{eq,FI}}{T_{FI} \cdot R_{CO2}} - \frac{P_{eq,FII}}{T_{FII} \cdot R_{CO2}} \right) \frac{1}{K_{CO2}} = \frac{dX_I}{dt} \{ R_{kl} \cdot f_3(X_I) + R_{DI} [f_2(X_I) - f_2(X_{II})] \} - \frac{dX_{II}}{dt} \cdot R_{kII} \cdot f_3(X_{II}) \quad (3.84)$$

$$\left(\frac{P_{eq,FII}}{T_{FII} \cdot R_{CO2}} - \frac{P_G}{T_G \cdot R_{CO2}} \right) \frac{1}{K_{CO2}} = \frac{dX_I}{dt} [R_{DII} \cdot f_2(X_{II}) + R_{\beta} \cdot f_1] + \frac{dX_{II}}{dt} [R_{kII} \cdot f_3(X_{II}) + R_{DII} \cdot f_2(X_{II}) + R_{\beta} \cdot f_1] \quad (3.85)$$

The twelve resistances in above 4 differential Equations (3.82) to (3.85) are defined as followings:

$$R_{\alpha,I} = \frac{r_S \cdot \Delta h_{CO2I}}{\alpha} \quad (3.86)$$

$$R_{\alpha,II} = \frac{r_S \cdot \Delta h_{CO2II}}{\alpha} \quad (3.87)$$

$$R_{\lambda_I} = \frac{r_S^2 \cdot \Delta h_{CO2I}}{\lambda_I} \quad (3.88)$$

$$R_{\lambda_{III,I}} = \frac{r_S^2 \cdot \Delta h_{CO2I}}{\lambda_{III}} \quad (3.89)$$

$$R_{\lambda I, II} = \frac{r_s^2 \cdot \Delta h_{CO2 II}}{\lambda_{II}} \quad (3.90)$$

$$R_{kI} = \frac{r_s}{K_{CO2 I}} = \frac{r_s}{K_{CO2}} \quad (3.91)$$

$$R_{kII} = \frac{r_s}{K_{CO2 II}} = \frac{r_s}{K_{CO2}} \quad (3.92)$$

$$R_{D I} = \frac{r_s^2}{D^p I} \quad (3.93)$$

$$R_{D II, I} = R_{D II, II} = R_{D II} = \frac{r_s^2}{D^p II} \quad (3.94)$$

$$R_{\beta, I} = R_{\beta, II} = R_{\beta} = \frac{r_s}{\beta} \quad (3.95)$$

where $\Delta h_{CO2 I}$ is the reaction enthalpy for $MgCO_3$ decomposition per 1 kg produced CO_2 , 2660 kJ/(kg CO_2), and $\Delta h_{CO2 II}$ the reaction enthalpy for $CaCO_3$ decomposition per 1 kg produced CO_2 , 3800 kJ/(kg CO_2).

The form functions are summarised in Table 3.3.

Table 3.3 Form functions for decomposition model of dolomite

f	for	plate	cylinder	sphere
f_1	R_{α}, R_{β}	$\frac{1}{b}$		
$f_2(X)$	$R_{\lambda I}, R_{D I}$	X	$\frac{1}{4} \ln\left(\frac{1}{1-X}\right)$	$\frac{1}{3(1-X)^{1/3}} - \frac{1}{3}$
$f_3(X)$	R_{kI}, R_{kII}	$\frac{1}{b}(1-X)^{(1/b-1)}$		

Then system of Equations (3-82) to (3-95), together with form functions in Table 3.3 and thermodynamic relations in Equation (3-73) and (3-74), is established for describing mathematically the simultaneous decomposition of dolomite. The conversion degree X_I and X_{II} , the profiles of temperature T and CO_2 partial pressure P , can be calculated as function of decomposition time t . The prerequisite for such a computation is that the material properties during dolomite decomposition (λ_I , $D^p I$, k_I , λ_{II} , $D^p II$ and k_{II}) should be known.

As mentioned before, the two components in dolomite can be separately decomposed under an artificial higher CO_2 pressure. The separate decomposition model, whose mathematical derivation is simpler than that of the simultaneous composition model described in this section, is more convenient for the evaluation of material properties. But generally, the simultaneous model can be applied if dolomite particles are to be decomposed on a moving grate in a gaseous atmosphere with a limited CO_2 pressure. The decomposition behaviour of dolomite in both models will be discussed later.

4. Building of models

4.1 Building of the model LEPOL

From the geometry of the Lepol grate system, which is shown in Figure 2.1, it can be seen that the spaces of gas chamber above and beneath the grate are large. Therefore the pressure drops in the two spaces can be neglected in comparison to that through the limestone bed. In a stable operation, the pressure drop through the bed should be approximately the same along the length direction. The gas flow distribution along the grate length can be then computed iteratively until an equalized pressure drop is obtained.

As mentioned already, there are four physical-chemical processes on the moving grate of limestone pre-heater. It is assumed that the water content, which amounts to about 1.1% after washing, will begin immediately to evaporate as soon as the limestone enters the hot gas chamber. The drying process is described by module EVAPORATION. In this module the whole heat transferred from the gas to the particle will be consumed exclusively to cover the evaporation enthalpy. Therefore the solid temperature stays unchanged. Having been dried completely, the solid temperature begins to increase. This is calculated by the module PREHEATING. In this module a homogeneous solid temperature is assumed for a whole particle. The effective heat transfer coefficient is adopted by correction of true heat transfer coefficient with a transient factor. As soon as the decomposition temperature, which corresponds to the partial pressure of CO_2 in gas atmosphere, is reached, the limestone begins to dissociate. A one-dimensional pseudo-stationary shrinking core model is described in module DECOMPOSITION. As the internal enthalpy of limestone or lime is relative small, compared with the reaction enthalpy, the supplied heat will be mostly consumed by reaction. For simplicity, it is assumed the increase of internal enthalpy during reaction stage is neglected. Once the decomposition is completed, the lime product will be heated further. This process is calculated in module AFTER-HEATING, which is similar to module PRE-HEATING.

The computation process of program LEPOL is illustrated in the flow chart Figure 4.1.

In the lime industry, two layers of particle size fractions are often used instead of a mixed single layer. The fine fraction lies on the top, and a course fraction on the bottom. The purpose of this operation is to reduce the pressure drop. A sharp size distribution means a larger porosity, which will lead to a more even penetration of hot gas. In this two-layer operation, the two fractions with different mean diameters must be computed separately with the four modules described above.

In the program LEPOL, the gas temperature distribution on the grate will be investigated for the purpose of protection the grate from high temperature. On the other hand, the enthalpy of the input gas must be utilized as much as possible to decompose more limestone on the grate.

The two-dimensional models, LEPOL and CLINKER, are divided geometrically into 20000 small cells, to obtain high computation accuracy with cell method.

4.2 Building of the model CLINKER

In comparison to the model LEPOL, the model CLINKER is simpler because there is no evaporation or chemical reaction on the grate. Only the heat transfer between air and clinker particles is considered in the same way as in model LEPOL. The air flow distribution along the grate is also internally computed, until an equalised pressure drop is obtained. In this model, it is more important to concentrate on the real air velocity and the minimal fluidisation velocity. But on the other hand, a large cooling rate of clinker should be ensured to obtain a good cement quality.

4.3 Calculation of pure heat transfer

As mentioned already before, the whole particle bed can be simulated with cell method. Although inside the whole bed the mass flows, temperatures and temperature-depending material properties

vary, they can be assumed as constant for each small cell. If the cell number is large enough, this treatment will deliver a satisfying accuracy.

A single cell, where only heat transfer takes place without evaporation or reaction, can be regarded as an ideal cross flow heat exchanger, and simulated by corresponding NTU- ϵ -method. The solid particle bed is treated as one fluid and the gas or air, which penetrating nearly perpendicularly through the void channels in the packed bed, as another. The transferred heat from gas to particle will be consumed exclusively for the changing of internal enthalpy of the solid.

Many researchers, such as Nusselt [25] and Mason [26], have determined the effectiveness values for cross flow heat exchanger with both fluids unmixed. The result from Mason, in the form of an infinite series by employing the Laplace transformation, converges more rapidly and is more readily adaptable for computational programming. The heat exchange effectiveness from the solid side, P_s , can be calculated as following:

$$P_s = \frac{1}{R_s \cdot NTU_s} \cdot \sum_{m=0}^{\infty} \left[\left(1 - e^{-NTU_s} \cdot \sum_{j=0}^m \frac{NTU_s^j}{j!} \right) \cdot \left(1 - e^{-R_s \cdot NTU_s} \cdot \sum_{j=0}^m \frac{R_s^j \cdot NTU_s^j}{j!} \right) \right] \quad (4.1)$$

where m is the number of summation term, which should be theoretically infinite to obtain the precise result. In the program, the relative error for every increasing term number is checked until a preset accuracy is satisfied.

The heat capacity flow ratio between solid and gas sides, R_s , is given as:

$$R_s = \frac{\dot{M}_s \cdot c_{PS}}{\dot{M}_G \cdot c_{PG}} \quad (4.2)$$

The number of transfer unit for solid side, NTU_s , is calculated by:

$$NTU_s = \frac{\alpha \cdot A}{\dot{M}_s \cdot c_{PS}} \quad (4.3)$$

where α is the heat transfer coefficient for this cell, which can be calculated with Nußelt number introduced before, and A the total heat transfer area in a cell.

The heat transfer area in a cell is obtained from particle and bed geometry:

$$A = N \cdot (\pi \cdot d^2) \quad (4.4)$$

where N the number of particle in a cell, and d the Sauter diameter of the particles.

The heat exchange effectiveness expressed for solid side, P_s , is:

$$P_s = \frac{T_s'' - T_s'}{T_G' - T_s'} \quad (4.5)$$

where T_s' , T_s'' and T_G' are the input temperature of solid, the output temperature of solid and the input temperature of gas.

Figure 4.2 from VDI-Wärmeatlas [3] shows the calculation diagram of a cross flow heat exchanger, as result of the equation system described above. Given the heat capacity flow ratio between solid particle and gas, R_s , and the number of transfer unit calculated with the heat capacity flow of solid side, NTU_s , the effectiveness for the solid side, P_s , can be easily find from the diagram. In the figure some values of a typical gas-solid-system on a Lepol grate are given, which will be detailed later on.

In Figure 4.3 the calculation strategy for a single cell of pure hart transfer is shown. Known the input mass flows and temperatures, the material properties can be obtained. The heat transfer coefficient and heat transfer area for this cell are calculated. Then R_s and NTU_s can be calculated and inserted into the Equation (4.1). The number of the term in the equation, m , is chosen as 10, which gives a good

computation precision. Finally, from Equation (4.5), the unknown T_S'' can be obtained from P_S , T_S' and T_G' .

As the equation system above holds for solid side as well, exchanging the index S and G, the heat exchange effectiveness for the gas side, P_G , and then the output temperature for the gas, T_G'' , can be similarly calculated. Or from energy conservation the same result can be easily obtained.

4.4 Calculation involving evaporation or reaction

If water evaporation or decomposition reaction takes place in a cell, the heat transferred from gas to solid is assumed to be consumed exclusively for the evaporation or reaction enthalpy. During the evaporation or reaction, the temperature of the solid particle will stay constant. Therefore the method for cross flow heat exchanger mentioned above can not be applied in this case.

Taking decomposition reaction of limestone as an example, Figure 4.4 shows the computation strategy for such a cell. Given the gas temperature for this cell, T_G' , and the partial pressure of CO_2 in the gas, P_G' , the equation system (3.55) to (3.62) can be applied to calculate the decomposition velocity $\frac{dX}{dt}$ and the temperature of reaction front T_F . From these two parameters, other desired values after the time interval Δt are calculated.

The conversion degree of limestone after Δt :

$$X'' = X' + \frac{dX}{dt} \cdot \Delta t \quad (4.6)$$

The mass of produced CO_2 from one particle:

$$M_{CO_2} = K_{CO_2} \cdot \left(\frac{4}{3} \pi \cdot r_s^3 \right) \cdot (X'' - X') \quad (4.7)$$

The mass flow of produced CO_2 from one particle:

$$\dot{M}_{CO_2} = \frac{M_{CO_2}}{\Delta t} \quad (4.8)$$

The increased mass flow of gas is obtained from mass conservation, considering N limestone particles are in one cell:

$$\dot{M}_G'' = \dot{M}_G' + N \cdot \dot{M}_{CO_2} \quad (4.9)$$

The heat is obtained from CO_2 mass via reaction enthalpy:

$$Q = \frac{\Delta \tilde{H}_R}{\tilde{M}_{CO_2}} \cdot M_{CO_2} \quad (4.10)$$

The heat flow is then:

$$\dot{Q} = \frac{Q}{\Delta t} \quad (4.11)$$

Taking the quasi-stationary assumption, the surface temperature T_S of particles can be calculated from the front temperature T_F and heat flow:

$$\dot{Q} = \frac{4\pi \cdot \lambda \cdot (T_S - T_F)}{\frac{1}{r_F} - \frac{1}{r_S}} \quad (4.12)$$

From energy conservation the output temperature of the gas T_G'' , can be then calculated, taking into account that N limestone particles are in one cell:

$$\dot{Q} \cdot N = \dot{M}_G' \cdot c_{PG} \cdot (T_G' - T_G'') \quad (4.13)$$

5. Material properties

5.1 Material properties in limestone decomposition

5.1.1 Equilibrium pressure

The rate and direction of a chemical reaction depends upon the deviation from the equilibrium state. Among all three educts and products only CO₂ is in the gaseous form. The equilibrium state is thus determined only by the pressure of CO₂. The equilibrium pressure, or so called decomposition pressure, which was measured by different authors, are plotted in Figure 5.1. It has no discernible dependence upon the genesis and nature of the limestone. The equilibrium pressure can be approximated by the Arrhenius law:

$$p_{eq} = p_{eq0} \cdot \exp\left(-\frac{\Delta\tilde{H}_R}{\tilde{R} \cdot T}\right) \quad (5.1)$$

where $\Delta\tilde{H}_R$ is the molar reaction enthalpy, 168 kJ/mol at 900°C,

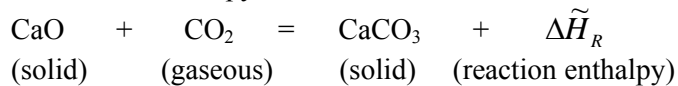
\tilde{R} the universal molar gas constant, 8.314 J/(mol·K),

T the reaction temperature, K, and

p_{eq0} the pre-exponential coefficient, or frequency factor, $2.15 \cdot 10^7$ bar.

When limestone is decomposed in industrial kilns the decomposition temperature depends on the CO₂ partial pressure in the kilns. This dependence is shown in Figure 5.2. Depending on the fuel, the CO₂ in kilns can vary from 20 to 40%(v), which results in a corresponding decomposition temperature of between 820 and 862°C. When heated in an atmospheric environment, whose CO₂ concentration is about 367ppmv, the limestone will begin to decompose at 542°C.

The reverse reaction of limestone decomposition is called recarbonization. When the partial pressure of CO₂ in the ambience exceeds the equilibrium pressure, lime can combine CO₂ to get CaCO₃, giving off reaction enthalpy.



For example, when lime is exposed in an atmospheric environment at a temperature lower than 542°C, it will absorb atmospheric CO₂ to produce CaCO₃.

5.1.2 Evaluation method for k, D^P and λ

Cheng and Specht [27] have investigated the equilibrium pressure of CO₂, the material properties during thermal decomposition of different types of limestone, namely their reaction coefficient, the pore diffusivities and the thermal conductivities.

In order to study the decomposition behaviours of limestone, magnesite and dolomite, it is necessary to know the material properties of the reaction coefficient k, the effective pore diffusivity D^P and thermal conductivity λ. However, the experimental measurement of these properties proves to be very difficult due to the high temperature. In following, an indirect method of evaluation method is described. Under some special conditions, this method is valid not only for limestone, but also for magnesite and dolomite.

In decomposition experiments of limestone, to be demonstrated later, it will be shown that the temperature at the reaction front T_F changes only slightly during decomposition under constant ambient conditions (P_G and T_G), especially when 0.1 < X < 0.9. Therefore the corresponding equilibrium pressure P_{eq} and resistances R_i remain virtually constant during decomposition. Taking T_F as constant, an analytical solution of this system can be achieved by integrating Equations (3.55) and (3.56):

$$t = R_\alpha \cdot f_3(X) + R_\lambda \cdot f_4(X), \quad (5.2)$$

$$t = R_{\beta} \cdot f_3(X) + R_D \cdot f_4(X) + R_k \cdot f_5(X), \quad (5.3)$$

where the form functions $f_3(X)$, $f_4(X)$ and $f_5(X)$ are summarized in Table 5.1.

Table 5.1 Form functions for different geometries

f	Plate	Cylinder	Sphere
$f_3(X)$	$f_3(X) = X$		
$f_4(X)$	$f_4(X) = X^2$	$f_4(X) = X + (1 - X) \cdot \ln(1 - X)$	$f_4(X) = 3 \left[1 - (1 - X)^{\frac{2}{3}} \right] - 2 \cdot X$
$f_5(X)$	$f_5(X) = X$	$f_5(X) = 1 - (1 - X)^{\frac{1}{2}}$	$f_5(X) = 1 - (1 - X)^{\frac{1}{3}}$

Given an experimentally determined decomposition progress X and measured T_F , the desired material properties (λ , D^p and k) can be derived. The Equations (5.2) and (5.3) can be transformed into two linear equations:

$$\frac{t}{f_3(X)} = R_{\alpha} + R_{\lambda} \cdot \frac{f_4(X)}{f_3(X)}, \quad (5.4)$$

$$\frac{t - R_{\beta} \cdot f_3(X)}{f_5(X)} = R_k + R_D \cdot \frac{f_4(X)}{f_5(X)}. \quad (5.5)$$

The resistance R_{β} , which is usually very small compared with the other four, can be calculated separately and can therefore be presumed to be known. Then R_{α} , R_k , R_{λ} and R_D can be easily obtained from the intercepts and slopes. Similar linearized equations can be derived if the Equations (5.2) and (5.3) are divided by $f_4(X)$ instead of by $f_3(X)$ and $f_5(X)$. However, Equations (5.4) and (5.5) are more convenient for evaluation. Finally, the required material properties (λ , D^p and k) can then be determined from the Equations (3.58), (3.60) and (3.59).

The experimental determination of desired values requires constant ambient conditions and measurement of time-dependent progress of the conversion degree (by weighing, for example) and the front temperature (by thermal couples, for example).

5.1.3 Experimental apparatus

The evaluation of the above equations requires particles of cylindrical or spherical shape. Cylinders were prepared from large limestone pieces using hollow drillers. From some of these cylinders spheres were drilled. The experimental apparatus for measuring the decomposition behaviour is shown schematically in Figure 5.3.

The limestone specimens were suspended from a balance with which the weight loss and therefore the conversion degree could be recorded continuously. In order to have well-defined flow conditions around the specimen and to be able to determine the convective heat and mass transfer, the specimen was enclosed within a cylindrical flow channel mounted in an electrically heated chamber furnace whose temperature was kept constant. Hot gas was introduced at the top of the channel and sucked off at a defined rate from the bottom. This prevented an enrichment of CO_2 in the channel, so that the ambient partial pressure of CO_2 was kept constant. In the centre of the specimen small holes were drilled. The temperatures inside the specimen were measured by thermocouples inserted in the holes. These were mounted at the centre for all the specimens involved, and also at the periphery for some specimen. The wall temperature of the channel was measured at various positions with thermocouples, whose measurements showed that the channel had a uniform temperature. An infrared absorption gas analyzer continuously indicated the concentration of CO_2 .

The tests were performed using spheres with diameters of 25 and 46 mm, and cylinders with diameters of 20, 25 and 46 mm. The length/diameter ratios of the cylinders ranged from 5 to 12, so that they could be regarded as infinitely long and treated as one-dimensional cases.

The chemical composition of the limestone investigated is given in Table 5.2.

Table 5.2 Chemical composition and bulk density of the types of limestone investigated

Chemical composition (%)	Cretaceous limestone		Jurassic limestone		Devonian limestone			Marble
	Lägerdorf	Langelsheim	Regensburg	Blaustein	Winterberg	Stromberg	Diez	Cercos
CaO	54.240	52.47	55.11	55.70	54.29	55.41	55.510	55.34
MgO	0.260	0.30	0.400	0.190	0.39	0.43	0.400	0.59
SiO ₂	1.860	4.68	0.340	0.240	1.83	0.26	0.100	0.08
Fe ₂ O ₃	0.080	0.24	0.090	0.032	0.21	0.06	0.010	0.05
Al ₂ O ₃	0.27	0.63	0.12	0.043	0.08	0.13	0.013	0.01
K ₂ O	0.046	0.08	0.017	0.007	0.02	-	0.005	0.004
Na ₂ O	0.041	0.03	0.018	0.013	0.01	-	0.013	0.01
BaO	0.01	0.01	0.011	0.012	0.02	-	0.008	0.01
SrO	0.036	0.03	0.005	0.004	0.02	-	0.009	0.01
Mn _x O _y	0.016	0.03	0.024	0.013	0.02	0.02	0.011	0.004
SO ₃	0.055	0.05	0.043	-	0	-	-	-
Weight loss	42.81	41.50	43.62	43.51	43.05	43.78	43.54	43.97
Sum.	99.72	100.06	99.80	99.76	99.94	100.09	99.64	100.08
Density (g/cm ³)	2.57	2.51	2.68	2.61	2.68	2.69	2.70	2.71

5.1.4 Decomposition behaviour

The decomposition behaviours recorded experimentally were similar for both spherical and long cylindrical samples. In both cases the front temperatures stayed nearly constant. Using different form functions in Table 5.1, the same linearized decomposition diagrams could be plotted. But for the purpose of material property evaluation, cylindrical geometry had advantage because the samples were easier to prepare. When the length/diameter ratio of cylinder was greater than 5, no more discernible influence of it could be observed. The volume of sample, as well as the ambient temperature, affected the front temperature. Because of larger resistance for heat supply a bigger specimen demonstrated a smaller reaction velocity, therefore a lower front temperature. In the evaluation, however, the conversion curves could be linearized satisfactorily, independent of the front temperature.

As an example, Figure 5.4 shows typical curves of X and T_F for two cylindrical limestone specimens with a diameter of 47 mm at different ambient temperatures of 1000 and 910°C. At temperatures below 750°C, the equilibrium pressure was so low that no substantial decomposition occurred. The heat supplied was first used only for raising the internal energy of the specimen. In comparison with the total decomposition time the heating-up of the specimen occurred very rapidly. After the heating-up of the specimen had been accomplished, the equilibrium pressure and the decomposition rate became so great that the heat transported to the specimen was consumed virtually only by reaction. The temperature in the carbonate core was then nearly uniform. Only within the oxide layer did the temperature become higher towards the surface. When several thermocouples were positioned at different locations inside the specimen, the progress of the reaction front could be observed. Once the reaction front passed the measuring point, the temperature underwent a significant increase. After completion of decomposition the core temperature finally rose until the ambient temperature was reached and a steady state was established.

The measured conversion curves for the decomposition degree were linearized in accordance with Equations (5.4) and (5.5). As an example, Figure 5.5 shows such diagrams for a cylindrical specimen (diameter 20 mm and length 100 mm) made of limestone from Winterberg. It is obvious that the measured values can be satisfactorily approximated by straight lines, and thus in turn confirms the validity of the equations established above. From the ordinate intercept the reaction rate coefficient and the overall heat transfer coefficient can be determined using Equations (3.59) and (3.57), respectively, and from the slopes the effective pore diffusivity and the thermal conductivity can be

calculated using Equations (3.60) and (3.58), respectively. The overall heat transfer coefficient in the experimental apparatus is of no further interest. The other three values will now be discussed.

5.1.5 Reaction coefficients

The reaction rate coefficients determined from the linearized conversion curves are represented in Figure 5.6. It is obvious that they are not strongly, if at all, dependent on the temperature. The main dependence of the decomposition time on the temperature is therefore due to the exponential temperature dependence of the equilibrium pressure. There is also no ascertainable influence of the CO₂ partial pressure on the reaction coefficient. It may further be shown that the reaction rate coefficient of the limestone investigated depends more on its type than its geographical origin. Jurassic limestone has the lowest reaction rate coefficients, cretaceous limestone the highest and Devonian limestone is somewhere between the two. The reaction rate coefficient averages 0.005 m/s, ranging from 0.003 to 0.012 m/s, that is to say, with a factor of 4.

In the literature the reaction rate coefficient is defined differently, with different dimensions. Most authors assumed the expressions of reaction kinetics according to Zawadski [28]:

$$\dot{N} = k_1 \cdot A_F \cdot \left(1 - \frac{P_F}{P_{eq}}\right) \quad (5.6)$$

where \dot{N} is the molar flow rate of produced CO₂, mol/s.

For comparison, the reaction rate coefficient k expressed in Equation (3.51) can be converted to k_1 in Equation (5.6) by:

$$k_1 = \frac{k \cdot P_{eq}}{\widetilde{R} \cdot T_F} \quad (5.7)$$

Values thus converted are represented in Figure 5.10 as well.

Using the definition in Equation (5.6), Ingraham and Marier [29] examined the decomposition of 6.4 mm pellets of reagent CaCO₃ in air. Borgwardt [30] measured the reaction rate of limestone particles ranging in size from 1 to 90 μm, over the temperature range from 516 to 1000°C. He used two naturally occurring types of limestone, representing markedly different physical and geological properties. One stone is Fredonia Valley White, and the other is Georgia Marble. Fuertes et al. [20] studied the decomposition of limestone particles, ranging in size from 0.25 to 1.85 mm, in a fluidized bed, over temperatures between 1034 and 1173K, at different CO₂ concentrations from 0 to 15%. His samples came from Riosa, Asturias, Spain. Rao [31] carried out experiments with a thermogravimetric analyzer under non-isothermal conditions with different heating rates (10 to 100 K/min). His sample was Analar grade calcium carbonate (May and Bakerm Ltd., Dagenham, England), with an average grain size of 10.7 μm. Considering CO₂ adsorption on the reaction interface under different total pressure, Garcia-Labiano et al. [32] used a similar definition to evaluate the decomposition kinetics of limestone sample Blanca with a size between 0.4 and 2 mm, in a temperature range from 1048 to 1173K. Ar and Dogu [33] investigated the calcination reaction of 10 different samples with average size of 1 mm, which were taken from different regions of Turkey, using thermogravimetric analysis. Their values of reaction rate coefficients are summarized in Figure 5.7.

It is clear that the values obtained by the above-mentioned authors are within the range of our results, irrespective of grain size. This indicates that the variation of reaction rate coefficients in previous works can probably be explained by different types or origins of limestone rather than the possible difference in methods or experimental errors.

5.1.6 Effective pore diffusivity

The effective pore diffusivity determined from the slope of the linearized decomposition diagrams in Figure 5.5 is represented in Figure 5.8. The effective pore diffusivity varies with sample origin with a factor of 10. It has considerable temperature dependence as well.

The magnitude of the pore diffusivity is substantially determined by the developed pore structure. Immediately after the decomposition, the pore size distribution in the formed oxide was measured with a mercury porosimeter with a pressure range of 0 to 2000 bar. The values of the mean diameter were in the range of 0.1 to 1 μm , which were smaller than the free path length of CO_2 . The higher the temperature in the oxide layer was, the stronger was the sintering effect, which resulted in a larger pore size and a smaller specific surface. The pore size depended both on the origin of the limestone and on the temperature at which the decomposition took place. Hence the transport of CO_2 through the oxide took place entirely by Knudsen diffusion, and the diffusivity was proportional to the pore diameter.

5.1.7 Thermal conductivity

Similarly, the thermal conductivity was estimated from the slope of the linearized conversion curve in Figure 5.9. The values were in the range of 0.55 to 0.85 $\text{W}/(\text{m}\cdot\text{K})$. The thermal conductivity here demonstrated no discernible dependence on temperature or material. In Fig.8 our results are compared with some values from the literature, using special direct measurement methods. Both values lie in the same range, which demonstrates that our evaluation method is reliable.

5.1.8 Heat capacity

The specific heat capacities of lime and limestone are temperature dependent. In Table 5.3 the specific heat capacities of pure CaCO_3 and CaO by Barin [34] are taken. They may differ somewhat from the real limestone and lime product, which can contain some impurities. Because the impurities are of very small amount, this deviation can not be very large.

Table 5.3 Specific heat capacities of CaCO_3 and CaO

T in K	c_p in $\text{J}/(\text{mol}\cdot\text{K})$	
	CaCO_3	CaO
298.15	83.471	42.122
300	83.817	42.239
400	96.985	46.628
500	104.547	48.981
600	109.872	50.479
700	114.144	51.555
800	117.863	52.401
900	121.266	53.111
1000	124.474	53.735
1100	127.554	54.302
1200	130.541	54.830
1300		55.330
1400		55.810

In some literatures these values are given as a polynomial function of temperature. But for the purpose of programming, exponent functions are formulated. Taking into account that the mole mass of CaCO_3 and CaO are 100.087 and 56.077 g/mol respectively, following exponential correlation can be obtained for the average specific heat capacity of CaCO_3 in $\text{J}/\text{K}/\text{kg}$ with a reference temperature of 20°C :

$$c_p(T_F) = 180 \cdot T_F^{0.26} \quad (5.8)$$

where T_F is the temperature of the unreacted limestone core.

For the average specific heat capacity of CaO in $\text{J}/(\text{kg}\cdot\text{K})$ with a reference temperature of 20°C :

$$c_p(T_{OX}) = 303 \cdot T_{OX}^{0.16} \quad (5.9)$$

where T_{OX} is the averaged temperature of the decomposed lime layer.

5.2 Material properties in magnesite decomposition

5.2.1 Equilibrium pressure

Specht et al. [35] have investigated the equilibrium pressure of CO₂, the material properties during thermal decomposition of different magnesites, namely the reaction coefficient, the pore diffusivities and the thermal conductivities.

Figure 5.10 shows the equilibrium pressure which have been measured by Goldsmith and Heard [36], Graf and Goldsmith [37], Harker and Tuttle [38], and Marc and Simek [39], as well as the computed equilibrium pressures from thermodynamic values by Haul and Markus [40] and Barin et al. [41]. This figure further contains some values, which have been determined with the aid of the experimental apparatus, explained by Kainer et al. [23]. The distribution of the measuring points is considerably large. From our own measurements of the equilibrium pressure, which have been executed only beneath 1 bar, because of the conception of the experimental apparatus, it has been the result that the reaction rate of the magnesite decomposition is very slow at these low temperatures. A change of the pressure will not be perceptible until a few days. The slow decomposition rate has also been reported by other authors. Experiments with high temperatures and therefore with high pressures are very difficult, so that the measured values have this scattering.

Similar to limestone, the Equation (5.1) holds for the CO₂ equilibrium pressure for all magnesites, only the pre-exponent coefficient and the reaction enthalpy are different. In magnesite decomposition, $P_{eq0} = 2.7 \cdot 10^8$ bar and $\Delta\tilde{H}_R = 117$ kJ/mol.

Because of the scattering of the measured points it cannot be ascertained whether any influence of the genesis and origin of the magnesites is available on the equilibrium pressure. Because on the one hand very pure magnesites have been investigated and on the other hand in the case of limestone it has been proven that there is no influence of the origin of the limestone upon equilibrium pressure according to Kainer et al. [23], it will be postulated, this equation is valid for all kinds of magnesite. If a certain magnesite should have a different equilibrium pressure, it will be necessary to multiply the following discussed properties corresponding to be applied equations with the ratio of the postulated to the real equilibrium pressure.

For the application in industry, the decomposition pressure is shown in Figure 5.11. The minimum decomposition pressure is 242°C corresponding to current atmospheric CO₂ concentration of 367 ppm(v). With a CO₂ concentration range of 20 - 40% in the furnace gas, the decomposition pressure of magnesite is between 396 and 419°C, which are significantly lower than carbonate.

The chemical composition of the magnesites investigated is given in Table 5.4.

Table 5.4 Chemical composition and bulk density of the magnesites investigated

Chemical composition (%)	Crypto crystalline				crystalline		
	Greece				Austria		Turkey
	Euböa	Euböa	Euböa	Euböa	Millstatt	Breitenau	-
CaO	0.28	-	0.99	0.69	0.38	0.84	1.89
MgO	46.12	-	45.90	47.15	45.45	42.50	45.40
SiO ₂	0.45	-	0.61	0.064	1.27	0.58	0.35
Fe ₂ O ₃	1.19	-	0.06	0.13	1.71	4.34	0.08
Al ₂ O ₃	0.06	-	1.13	0.016	0.07	0.40	0.19
K ₂ O	0.012	-	-	0.003	0.008	-	-
Na ₂ O	0.01	-	-	0.014	0.023	-	-
BaO	0.002	-	-	0.002	0.003	-	-
SrO	0.001	-	-	0.001	0.001	-	-
Mn ₂ O ₃	0.11	-	-	0.005	0.095	-	-
SO ₃	0.00	-	-	0.003	0.00	-	-
Weight loss	51.78	51.60	51.0	51.50	51.03	51.1	51.6

Sum.	99.42	-	99.69	99.58	100.04	99.79	99.51
Density (g/cm ³)	2.95	2.80	2.54	2.36	2.96	3.00	2.80

5.2.2 Decomposition behaviour

Typical curves of the decomposition of magnesite have often been represented in the literature. This is the reason why here only four measured curves of decomposition are plotted in Figure 5.12, with the corresponding ambient temperature and core temperature, and that, beginning with a very low ambient temperature of 550°C, at which the decomposition just starts and continuing with a gradual temperature rise of 50K in each case. From these four examples it can be drawn that the temperature at the reaction layer is only increasing a little bit during the decomposition process after a short starting period. Because of the slight temperature increase the decomposition temperature T , and the equilibrium pressure P_{eq} may be regarded as approximately constant. The assumption of constant resistances is therefore met, which is necessary for the linearizing action of the curves of the decomposition degree. The level of the decomposition temperature and of the CO₂ partial pressure in the oxide layer will be considered in detail later on.

The measured behaviour curves for the degree of decomposition have been linearized. As an example, Figure 5.13 shows such linearized diagrams for some magnesite cylinders. It is apparent that the measured values may be very satisfactorily approximated by straight lines, which confirms the validity of the equations established. From the ordinate intercept values we can now determine the reaction coefficient and the effective heat transfer coefficient via corresponding equations mentioned above, and from the gradients we can determine the diffusion coefficient and the heat conduction coefficient via corresponding equations. The effective heat transfer coefficient in the experimental apparatus is of no further interest here. The three material values will now be discussed.

5.2.3 Reaction rate coefficients

The reaction coefficients determined from the linearized decomposition behaviour curves are represented in Figure 5.14. It is apparent that they differ from one kind of magnesite to another. Their values nevertheless exhibit nearly the same dependence on the temperature responding to the Arrhenius equation with activation energy of 55 kJ/mol. Only the frequency factors differ between the kinds of magnesite. The scattering of the obtained values around the compensation line can be considered as small. Values of reaction coefficients of magnesite are not known in literature.

5.2.4 Effective pore diffusivity

The pore diffusion coefficients determined from the gradient of the linearized decomposition behaviour curves are represented in Figure 5.15. The various investigated magnesites have partially differing values, which scatter range extends about the factor 10. It is remarkable, that the Breitenauer magnesite with the lowest pore diffusion coefficients shows the biggest hardness while preparing the test specimen, in comparison to this the Euböa magnesite with the density 2.54 g/cm³ could be prepared easily. The pore diffusion coefficients depend very much on temperature. For all magnesites the same dependence on temperature may be assumed for their pore diffusion coefficients, with an approximation by the exponential function:

$$D_{eff}^p = D_0^p \cdot e^{(0.0165 \cdot T_{ox})} \quad (5.10)$$

where D_0^p is a material dependent coefficient,
and T_{ox} the mean absolute oxide temperature.

The CO₂ partial pressures at the reaction layer resulted from the equations mentioned previously are plotted in Figure 5.12. The partial pressure increases with the duration of decomposition, because the diffusion path length becomes longer and longer, so that a higher partial pressure difference is needed for the mass transport. It can be seen, even for the Euböa magnesite with the highest pore diffusion coefficients, which the partial pressure lays far above 1 bar. Therefore it will be researched whether

the CO₂ transport through the oxide layer is caused by diffusion or by flow proceeding from the total pressure gradient.

5.2.5 Thermal conductivity

The thermal conduction coefficients, determined from the linearized curves of the decomposition behaviour, are represented in Figure 5.16. According to Equation (3.58) the thermal conductivity is proportional to the temperature difference between the ambience and the reaction front, which has been only a few Kelvin during most of the experiments. So the heat conduction coefficient can not be determined very exactly with the thin specimen used here, because on the one hand, the temperatures of the ambience (wall temperature of the channel) exhibit differences of up to 5K and, on the other hand, the temperature of the reaction front rises a few degrees during the decomposition. There is no discernible dependence of the measured values on the temperature of material.

5.2.6 Heat capacity

In Table 5.5 the specific heat capacities of pure MgCO₃ and MgO by Barin [34] are shown. They may differ somewhat from the real magnesite and its decomposition product, which can contain some impurities. Because the impurities are of very small amount, this deviation can not be very large.

Table 5.5 Specific heat capacities of MgCO₃ and MgO

T in K	c _p in J/(K·mol)	
	MgCO ₃	MgO
298.15	75.520	37.110
300	75.868	37.245
400	90.102	42.560
500	99.793	45.543
600	107.694	47.430
700	114.750	48.748
800		49.741
900		50.538
1000		51.209
1100		51.796
1200		52.324
1300		52.809
1400		52.264
1500		53.695

In some literatures these values are given as a polynomial function of temperature. But for the purpose of programming, exponent functions are formulated. Taking into account that the mole mass of MgCO₃ and MgO are 84.314 and 40.304 g/mol respectively, following exponential correlation can be obtained for the average specific heat capacity of MgCO₃ in J/(kg·K) with a reference temperature of 20°C:

$$c_p(T_F) = 239 \cdot T_F^{0.26} \quad (5.11)$$

where T_F is the temperature of the unreacted magnesite core.

For the average specific heat capacity of MgO in J/(kg·K) with a reference temperature of 20°C:

$$c_p(T_{OX}) = 426 \cdot T_{OX}^{0.14} \quad (5.12)$$

where T_{OX} is the averaged temperature of the decomposed oxide layer.

5.3 Material properties in dolomite decomposition

5.3.1 Equilibrium pressure

As mentioned before, both the CO₂ equilibrium pressures for limestone and magnesite decompositions can be described with Equation (5.1), only with different the pre-exponent coefficient and the reaction

enthalpy. To investigate the equilibrium pressure for dolomite decomposition, measured values from literatures [36] to [42] are plotted in Figure 5.17, for both decomposition stages respectively. The solid lines in the figure are the equilibrium pressures for decomposition of magnesite and calcite, for comparison. Obviously, there is no discernible difference from the first stage of dolomite decomposition and that of magnesite. The equilibrium pressure in the second stage conforms to that of the calcite very well. Therefore, $P_{eq0} = 2.7 \cdot 10^8$ bar and $\Delta\tilde{H}_R = 117$ kJ/mol can be assumed for the first decomposition stage of dolomite, while $P_{eq0} = 2.15 \cdot 10^7$ bar and $\Delta\tilde{H}_R = 168$ kJ/mol for the second. Furthermore, there is no substantial dependence of the equilibrium pressure of both stages upon the genesis and nature of the dolomite samples concerned.

5.3.2 Simultaneous decomposition behavior of both components

As many researches have mentioned, the decomposition of dolomite under the atmosphere of a smaller CO_2 partial pressure can take place simultaneously. That means, unless the CaCO_3 decomposition is deliberately suppressed during the MgCO_3 decomposition, by a high CO_2 pressure in ambience, the CaCO_3 can begin to decompose before the MgCO_3 in dolomite is consumed completely.

To investigate quantitatively the simultaneous decomposition behavior of both components in dolomite, the mathematical model introduced before is applied. As an example, a simulation is done for the simultaneous decomposition of a spherical piece with a diameter of 40mm in a typical shaft kiln. The gas has an empty tube velocity of 0.3 m/s in normal state, a CO_2 partial pressure of 0.2 bar and a temperature of 1150°C. The calculated temperatures at particle surface and at both reaction fronts are shown in Figure 5.18. The calculated partial pressure of CO_2 at particle surface and at both reaction fronts are shown in Figure 5.19. As comparison, the equilibrium pressure at CaCO_3 decomposition front is drawn in this figure as well. The calculated conversion degrees of both components and of dolomite in total are shown in Figure 5.20.

From the simulation results, it is obvious, that the MgCO_3 component will begin to decompose earlier than CaCO_3 , at a temperature of 642°C, which corresponds to the CO_2 partial pressure in the ambience. During the decomposition, the temperature at the surface increases from 640 to 850°C in the first 5.4 minutes, while the temperature at the first reaction front increases slowly from 640 to 680°C. The CO_2 partial pressure at the surface, on the contrary, decreases from 0.7 to 0.6 bar, which is still lower than the theoretical equilibrium pressure of CaCO_3 decomposition. This prohibits any possible CaCO_3 decomposition thermodynamically. At the time of about 5.4 minutes, the conversion of MgCO_3 reaches 51%, which means 26% of total dolomite conversion.

After 5.4 minutes, the temperature of solid surface is higher than 850°C, which corresponds to an equilibrium pressure of larger than 0.6 bar for CaCO_3 decomposition. The positive value of pressure difference, $P_{eq,F,Ca} - P_{F,Ca}$, can then lead to CaCO_3 decomposition. In this period, both reaction fronts exist simultaneously and progress to wards the core with different velocities. In this period, the temperature at the first reaction front stays nearly constant by about 680°C, while the temperature at the second front increases.

At the time of 22.5 minutes, the first reaction front of MgCO_3 decomposition reaches the core of dolomite sphere. Then the MgCO_3 component is completely converted into MgO , while the CaCO_3 conversion is still 32% and the total dolomite conversion is 66%. After 22.5 minutes, all the heat supply from the hot gas is used for CaCO_3 decomposition. It takes another 50 minutes to complete the total decomposition and to reach total conversion of 1.

5.3.3 Separate decomposition behavior of both components

Under some special conditions, for instance when the ambient CO_2 pressure is 1 bar, both MgCO_3 and CaCO_3 components in dolomite can be separately decomposed. This is more convenient if the evaluation method introduced above will be applied to evaluate the material properties in dolomite decomposition, similar to limestone or magnesite decomposition.

To investigate the first decomposition stage, the dolomite samples were burnt in pure CO₂ gas. Because the ambient partial pressure of CO₂ was higher than the equilibrium pressure for calcium carbonate, its decomposition could not take place. However, as Figure 5.17 has shown, the partial pressure of CO₂ in MgCO₃ decomposition is far above 1 bar, so magnesite decomposition could begin quickly, and the ambient CO₂ pressure had slight influence upon the CO₂ transport. Figure 5.21 shows the measured progress of conversion and temperature in a dolomite cylinder during the first stage. It should be noticed that the front temperature stays approximately constant with small conversion, especially when 0.1 < X < 0.5.

If the conversion curves are linearized as described before, diagrams in Figure 5.22 were obtained. The measured points can be approximated by a straight line only when $f_1(X)/f_2(X)$ is below about 0.4. This value corresponds to a conversion degree smaller than 0.5, corresponding to the region of constant front temperature. Only inside this range the decomposition can be described by the analytical methods from the shrinking core model. For the total decomposition this analytical solution is only a rough estimation. It should be mentioned that for pure magnesite and pure calcite the front temperature remains approximately constant during the whole decomposition, as shown by Cheng and Specht [27] and Specht et al. [35]. For these pure carbonates the shrinking core model fits well and the linearization method is proper to determine the material properties. That is the reason why the linear analysis method is used here as well, especially to compare the material properties with those from the pure carbonates.

The progress of the conversion and the front temperature during the second decomposition stage of a 47mm cylindrical half-burnt dolomite are shown in Figure 5.23 at two different ambient temperatures. The half-burnt samples were decomposed in air. Although the starting material before decomposition was porous, the front temperature during the second stage keeps nearly constant.

The linearized conversion courses according to the Equations (5.4) and (5.5) are plotted in Figure 5.24, as an example for half-burnt dolomite cylinders with diameter 25mm from Scharzfeld. Obviously, the measured values can be approximated well by straight lines, which in return prove that the shrinking model referring to a sharp reaction front can be applied to describe the decomposition behavior of the CaCO₃ component in dolomite. The microscopic pictures of a decomposing sample and numerical calculation demonstrate, the reaction zone inside the porous material is so small, in comparison to the dimension of sample, that it can be treated as an inwards contracting sharp reaction front.

5.3.4 Reaction rate coefficients

The reaction coefficients determined from the linearized conversion curves are represented in Figure 5.25. The coefficients for MgCO₃ component in first decomposition stage have a range of $3 \cdot 10^{-5}$ to $5 \cdot 10^{-4}$ m/s between 520 and 730°C, slightly increasing with temperature. The values for dolomite from Hagen-Halden are somewhat smaller than the other two. Specht et al. [35] have investigated the thermal decomposition of 6 different magnesites. Their results agree to the values for the first stage in this study. Both reaction coefficients can be approximated by:

$$k = 5 \cdot 10^{-2} \sim 5 \cdot 10^{-1} \cdot e^{-\frac{55000}{R \cdot T}} \quad (5.13)$$

The coefficients for the second stage in the temperature range of 780 to 900°C are between 0.02 and 0.05 m/s. The temperature dependence is very slight, if any. Cheng and Specht [27] have investigated decomposition of lumpy limestone samples of 10 different origins. Their reaction coefficients vary with a factor of 4, ranging from 0.003 to 0.012 m/s, without temperature dependence. In comparison, the reaction coefficients for the second stage in this work are about 10 times higher than those for pure limestone. This discrepancy can be explained by the difference between raw limestone and half-burnt dolomite. Limestone is very dense and the reaction front is more or less sharp, while half-burnt dolomite is porous and the decomposition takes place in a reaction zone. Therefore, the reaction coefficient is different, when referred to the same apparent reaction area.

5.3.5 Effective pore diffusivity

The effective pore diffusivities of dolomite oxides were evaluated with the linearized diagram, after the first or second decomposition stage, respectively. The values are summarized in Figure 5.26. For the first stage whose decomposition temperatures are between 520 and 730°C, the effective pore diffusivities are found in the range of $1.5 \cdot 10^{-8}$ to 10^{-6} m²/s for the half-burnt oxides. A higher temperature leads to a higher diffusivity, which can also be explained by the enlargement of pore size due to sintering. The values for Hagen-Halden dolomite are much smaller than the other two origins at a same temperature. Compared with the effective pore diffusivity for pure magnesite decomposition according to Specht et al. [35], whose values are between $5 \cdot 10^{-8}$ and $3 \cdot 10^{-6}$, the diffusivity for the first stage of dolomite decomposition are about one third. The reason could be that the porosity of the half-burnt dolomites is lower than that of the magnesite.

For the second stage whose decomposition temperatures are between 780 to 900°C, the diffusivities are larger than those for half-burnt oxides, because after the second stage, the porosity and pore size must be bigger than before. The effective pore diffusivities are between $7 \cdot 10^{-6}$ and $3 \cdot 10^{-5}$ m²/s, fluctuating with a factor of 5. They show temperature dependence as well, and increase slightly with the decomposition temperature because of the sintering effect. These results have the same range with those for pure limestone decomposition in [27].

5.3.6 Thermal conductivity

The heat conductivity of dolomite oxide after the second decomposition stage is evaluated and shown in Figure 5.27. After decomposition at temperature from 780 to 900°C, the dolomite oxide has a thermal conductivity in the range of 0.3 to 0.6 W/(m·K), with a factor of 2. These values are nearly the same as those of magnesite oxide in [35], but slightly smaller than those of carbonate oxides in [27], which is between 0.55 and 0.85 W/(m·K). A clear temperature dependence can not be observed from the results.

5.3.7 Heat capacity

In Table 5.6 the specific heat capacities of pure CaMg(CO₃)₂ and MgO·CaO by Barin [34] are shown. They may differ somewhat from the real dolomite and the decomposed product, which can contain some impurities. Because the impurities are of very small amount, this deviation can not be very large.

Table 5.6 Specific heat capacities of CaMg(CO₃)₂ and MgO·CaO

T in K	c _p in J/(mol·K)	
	CaMg(CO ₃) ₂	MgO·CaO
298.15	157.531	79.583
300	157.978	79.850
400	176.523	89.483
500	189.431	94.353
600	200.119	97.349
700	209.760	99.459
800	218.843	101.097
900	227.601	102.461
1000	236.158	103.654
1100	244.582	104.737
1200	252.917	105.743
1300		106.696
1400		107.611
1500		108.496

In some literatures these values are given as a polynomial function of temperature. But for the purpose of programming, exponent functions are formulated. Taking into account that the mole masses of CaMg(CO₃)₂ and MgO·CaO are 184.401 and 96.382 g/mol respectively, following exponential

correlation can be obtained for the average specific heat capacity of dolomite in J/(kg·K) with a reference temperature of 25°C:

$$c_p(T_F) = 257 \cdot T_F^{0.21} \quad (5.14)$$

where T_F is the temperature of the unreacted dolomite core.

For the average specific heat capacity of the decomposed product of dolomite, MgO·CaO:

$$c_p(T_{OX}) = 349 \cdot T_{OX}^{0.15} \quad (5.15)$$

where T_{OX} is the temperature of the oxide layer.

5.4 Clinker

The approximate chemical constituents of Portland cement clinker are listed in Table 5.7.

Table 5.7 Chemical constituents of Portland cement clinker [4]:

Constituent	Percent (%)
CaO	58-67
SiO ₂	16-26
Al ₂ O ₃	4-8
Fe ₂ O ₃	2-5
MgO	1-5
Mn ₂ O ₃	0-3
SO ₃	0.1-2.5
P ₂ O ₅	0-1.5
K ₂ O+Na ₂ O	0-1
TiO ₂	0-0.5
Lost of ignition	0.5-3

Clinker minerals are not pure compounds but mixed crystal phases, which contain constituents of other phases in small amounts as combinations of mixed crystals; these crystals contain also the remaining chemical admixtures of the clinker, which are not able to form separate phases. To characterize the difference between the pure compounds and the clinker minerals, the designations for the main clinker compounds are used in the practice, namely alite for C₃S (3CaO·SiO₂), and belite for C₂S (2CaO·SiO₂).

The density of Portland cement clinker is estimated as about 2700 kg/m³, the thermal conductivity about 0.65 W/(m·K), and the mean specific heat capacity about 920 J/(kg·K).

5.5 Gas and air

If the temperature dependence of the material properties cannot be neglected they can be calculated with the following equations according to Specht [43]:

$$\lambda = \lambda_0 \cdot \left(\frac{T}{T_0} \right)^{n_\lambda} \quad (5.16)$$

$$\eta = \eta_0 \cdot \left(\frac{T}{T_0} \right)^{n_\mu} \quad (5.17)$$

$$a = a_0 \cdot \left(\frac{T}{T_0} \right)^{n_a - n_c + 1} \quad (5.18)$$

$$\rho = \rho_0 \cdot \left(\frac{T}{T_0} \right)^{-1} \quad (5.19)$$

$$c_p = c_{p0} \cdot \left(\frac{T}{T_0} \right)^{n_c} \quad (5.20)$$

$$\nu = \nu_0 \cdot \left(\frac{T}{T_0} \right)^{n_\nu+1} \quad (5.21)$$

where $T_0 = 273$ K.

Material properties of gases in temperature $T_0 = 273$ K are gathered in Table 5.8.

Table 5.8 Material properties of gases in $T_0 = 273$ K [43]

Gas	\tilde{M}	ρ_0	c_{p0}	n_c	λ_0	n_λ	η_0	n_η	Pr
unit	kg/mol	kg/m ³	J/(kg·K)	-	W/(m·K)	-	kg/(m·s)	-	-
N ₂	0.028	1.26	1000	0.11	0.024	0.76	16.8	0.67	0.70
CO	0.028	1.26	1000	0.12	0.024	0.78	16.8	0.67	0.70
Air	0.029	1.29	1000	0.10	0.025	0.76	17.4	0.67	0.70
O ₂	0.032	1.44	0900	0.15	0.025	0.80	19.7	0.67	0.70
CO ₂	0.044	1.98	0840	0.30	0.017	1.04	14.4	0.77	0.73
H ₂ O	0.018	0.81	1750	0.20	0.016	1.42	8.7	1.13	0.95

The properties of gas mixtures can be calculated with the following formulas:

$$\rho_M = \sum \rho_i \cdot \tilde{x}_i \quad (5.22)$$

$$\lambda_M \approx \sum \lambda_i \cdot \tilde{x}_i \quad (5.23)$$

$$c_{PM} = \sum c_{Pi} \cdot x_i = \frac{1}{\rho_M} \cdot \sum c_{Pi} \cdot \tilde{x}_i \cdot \rho_i \quad (5.24)$$

where \tilde{x}_i is the molar or volume fraction of component i in a gas mixture.

and x_i the mass fraction of component i in a gas mixture.

6. Simulation and result with the model LEPOL

6.1 Operation data

Tables 6.1 describes a real Lepol grate facility in the lime industry, which is installed in front of a lime rotary kiln and used for preheating limestone particles. The over-heating problem of the Lepol grate, as explained before, takes place sometimes. The real operation parameters are used as the basic data of the simulation. All the important parameters are to be varied in the model to see their influence upon the gas temperature when it reaches the grate.

Table 6.1 Operation data of a limestone preheating Lepol grate

Parameter	Definition	Unit	Value
Length	Length of the grate	m	23
Width	Width of the grate	m	4
MSFine	Mass throughput of the fine grain fraction	kg/s	10.3
HeightFine	Bed depth of the fine grain fraction	m	0.275
DFine	Equivalent diameter of the fine grain fraction	m	0.0223
PorFine	Porosity of the fine grain fraction	-	0.48
MSBig	Mass throughput of the coarse grain fraction	kg/s	10.3
HeightBig	Bed depth of the coarse grain fraction	m	0.275
DBig	Equivalent diameter of the coarse grain fraction	m	0.0088
PorBig	Porosity of the coarse grain fraction	-	0.48
WaterS00	Water content in limestone particles	-	0.011
TO00	Stone temperature at entrance	°C	20
TRef	Reference temperature	°C	20
Pt	Total gas pressure	Pa	101325
CO200	Volumetric fraction of CO ₂ in gas	-	0.269
CO00	Volumetric fraction of CO in gas	-	0.0005
O200	Volumetric fraction of O ₂ in gas	-	0.0046
Water00	Volumetric fraction of vapour in gas	-	0.0860
Hrm	Reaction enthalpy, as $\Delta\tilde{H}_R$ in Equation (5.1)	J/mol	168000
Pmax	Maximum equivalent partial pressure of CO ₂ , as P_{eq0} in Equation (5.1)	Pa	$2.15 \cdot 10^{12}$
Rc	Gas constant of CO ₂	J/(kg·K)	188.9
HVap	Evaporation enthalpy of water	J/kg	$2.5 \cdot 10^6$
CpWaterIn	Heat capacity of water	J/(kg·K)	4200
CpVapor	Heat capacity of water vapour	J/(kg·K)	2074
Lambda	Thermal conductivity of lime	W/(m·K)	0.65
K	Reaction coefficient	m/s	0.006
K1	A parameter for effective pore diffusivity of CO ₂ in lime, as in $D^p_{eff} = K_1 \cdot T + B_1$	-	0.0161
B1	A parameter for effective pore diffusivity of CO ₂ in lime, as in $D^p_{eff} = K_1 \cdot T + B_1$	-	-28.78
DenS	Density of limestone	kg/m ³	2700
PurS	Purity of CaCO ₃ in limestone	-	1

6.2 Simulation cases

6.2.1 Single-layer operation mode

Some scenarios are simulated for single-layer operation, when the limestone particle of one Sauter diameter is assumed. The parameters and some simulation results are listed in Table 6.2.

Table 6.2 Simulation scenarios of single-layer operation

Case	L (m)	TG00 (°C)	MG00 (kg/s)	MStaub (kg/s)	H (m)	MS (kg/s)	D (mm)	Por (-)	Ave. A (-)	Ave. Alpha (W/(m ² ·K))	Ave. TG (°C)	Eff (-)	TGm (°C)
0	23	1100	28.8	1.67	0.55	20.6	12.7	0.426	0.202	89.9	436.2	0.621	866.01
1	7.67	1100	28.8	1.67	0.55	20.6	12.7	0.426	0.182	143.4	455.4	0.604	860.45
2	11.5	1100	28.8	1.67	0.55	20.6	12.7	0.426	0.193	120.1	446.5	0.612	862.13
3	46	1100	28.8	1.67	0.55	20.6	12.7	0.426	0.201	69.0	432.0	0.625	868.54
4	69	1100	28.8	1.67	0.55	20.6	12.7	0.426	0.195	59.8	430.4	0.626	869.08
5	23	950	28.8	1.67	0.55	20.6	12.7	0.426	0.072	81.6	402.6	0.606	858.98
6	23	1025	28.8	1.67	0.55	20.6	12.7	0.426	0.140	85.8	420.8	0.613	863.57
7	23	1175	28.8	1.67	0.55	20.6	12.7	0.426	0.258	93.8	449.1	0.630	868.40
8	23	1250	28.8	1.67	0.55	20.6	12.7	0.426	0.306	97.7	461.3	0.639	868.59
9	23	1100	9.61	1.67	0.55	20.6	12.7	0.426	0.075	50.1	20.3	1.0	27.83
10	23	1100	14.4	1.67	0.55	20.6	12.7	0.426	0.106	62.7	95.3	0.935	433.87
11	23	1100	57.6	1.67	0.55	20.6	12.7	0.426	0.397	123.9	658.4	0.403	869.04
12	23	1100	86.5	1.67	0.55	20.6	12.7	0.426	0.586	148.7	734.7	0.326	879.36
13	23	1100	28.8	0.834	0.55	20.6	12.7	0.426	0.197	88.0	422.6	0.634	864.24
14	23	1100	28.8	3.33	0.55	20.6	12.7	0.426	0.214	93.6	460.7	0.598	868.16
15	23	1100	28.8	1.67	0.183	20.6	12.7	0.426	0.165	89.5	466.3	0.595	852.61
16	23	1100	28.8	1.67	0.275	20.6	12.7	0.426	0.185	89.8	451.3	0.608	857.46
17	23	1100	28.8	1.67	1.10	20.6	12.7	0.426	0.203	90.0	431.8	0.625	868.69
18	23	1100	28.8	1.67	1.82	20.6	12.7	0.426	0.228	90.1	435.8	0.617	868.60
19	23	1100	28.8	1.67	0.55	6.87	12.7	0.426	0.580	96.2	731.3	0.328	868.66
20	23	1100	28.8	1.67	0.55	10.3	12.7	0.426	0.401	94.9	660.0	0.401	868.40
21	23	1100	28.8	1.67	0.55	41.2	12.7	0.426	0.092	78.7	95.8	0.934	389.72
22	23	1100	28.8	1.67	0.55	61.8	12.7	0.426	0.053	70.8	22.6	0.998	59.55
23	23	1100	28.8	1.67	0.55	20.6	5.00	0.426	0.341	163.0	457.8	0.583	869.20
24	23	1100	28.8	1.67	0.55	20.6	8.00	0.426	0.206	119.2	433.2	0.624	868.42
25	23	1100	28.8	1.67	0.55	20.6	15.0	0.426	0.198	81.4	439.5	0.618	862.59
26	23	1100	28.8	1.67	0.55	20.6	25.0	0.426	0.168	60.3	462.8	0.598	845.56
27	23	1100	28.8	1.67	0.55	20.6	12.7	0.350	0.204	95.4	434.8	0.622	867.61
28	23	1100	28.8	1.67	0.55	20.6	12.7	0.5	0.200	84.5	438.4	0.619	863.80

6.2.2 Two-layer operation mode

Some scenarios are simulated for two-layer operation, when the limestone particle bed consists of two layers of different Sauter diameters. This is done in the practice by using an extra sieve in front of the limestone input of the grate. The larger fraction lays on the grate, while the finer fraction lays on the larger fraction. The parameters and some simulation results are listed in Table 6.3.

Table 6.3 Simulation scenarios of single-layer operation

Case	L (m)	TG00 (°C)	MG00 (kg/s)	MStaub (kg/s)	H (m)	MS (kg/s)	D (mm)	Por (-)	Ave. A (-)	Ave. Alpha (W/(m ² ·K))	Ave. TG (°C)	Eff (-)	TGm (°C)		
29	23	1100	28.8	1.67	0.275	10.3	8.8	0.48	0.409	0.205	114.0	86.2	431	0.625	845
					0.275	10.3	22.3	0.48	0.000		57.2				
30	23	950	28.8	1.67	0.275	10.3	8.8	0.48	0.153	0.077	104.6	78.4	403	0.605	831
					0.275	10.3	22.3	0.48	0.000		51.2				
31	23	1025	28.8	1.67	0.275	10.3	8.8	0.48	0.290	0.145	109.4	82.4	418	0.615	839
					0.275	10.3	22.3	0.48	0.000		54.2				
32	23	1175	28.8	1.67	0.275	10.3	8.8	0.48	0.511	0.256	118.4	89.9	442	0.635	849
					0.275	10.3	22.3	0.48	0.000		60.2				
33	23	1250	28.8	1.67	0.275	10.3	8.8	0.48	0.595	0.298	122.7	93.5	453	0.644	853
					0.275	10.3	22.3	0.48	0.000		63.2				

34	23	1100	9.61	1.67	0.275	10.3	8.8	0.48	0.180	0.090	74.5	51.0	28	0.993	107
					0.275	10.3	22.3	0.48	0.000		26.9				
35	23	1100	14.4	1.67	0.275	10.3	8.8	0.48	0.222	0.111	87.3	62.0	115	0.916	448
					0.275	10.3	22.3	0.48	0.000		36.0				
36	23	1100	57.6	1.67	0.275	10.3	8.8	0.48	0.774	0.396	149.2	117.4	653	0.407	871
					0.275	10.3	22.3	0.48	0.017		83.9				
37	23	1100	86.5	1.67	0.275	10.3	8.8	0.48	0.978	0.557	175.1	140.1	735	0.325	906
					0.275	10.3	22.3	0.48	0.136		103.0				
38	23	1100	28.8	1.67	0.275	10.3	22.3	0.48	0.331	0.171	64.7	83.2	462	0.599	868
					0.275	10.3	8.8	0.48	0.010		99.8				
39	23	1100	28.8	1.67	0.193	7.24	7.5	0.48	0.584	0.205	127.7	85.3	428	0.626	843
					0.357	13.4	20.5	0.48	0.000		61.5				

6.3 Rough energy balance

As mentioned before, the gas-solid-system on the Lepol grate can be divided into small cell, where the constant material properties and a small ideal cross flow heat exchanger can be assumed. The whole system, furthermore, can be treated as a large cross flow heat exchanger as well, to obtain a rough energy balance. Because the gas heat used for limestone decomposition and water evaporation are low, compared with the internal energy gained by solid particles. The typical one-layer operation of case 0, which is listed in Table 6.2, shows such a rough balance as an example:

The typical hot gas input is 28.8 kg/s at 1100°C, plus 1.67 hot dust at the same temperature. Known composition of the combustion gas, the average heat capacity of the gas mixture at input is obtained as 1216 J/(kg·K). For simplicity, the heat capacity of the small amount of dust is assumed as same as that of the gas. The limestone has a throughput of 20.6 kg/s, an entrance temperature of 20°C and a heat capacity of about 800 J/(kg·K). The heat capacity flow ratio between the solid and the gas, R_S , is therefore 0.44. Gas heat is in substantial excess.

The big dimension of the limestone bed (23m×4m×0.55m) and the small particle diameter (12.7 mm) give a large heat transfer area of $1.37 \cdot 10^4 \text{ m}^2$ for the total bed, taking into account a void fraction of 0.426. The average effective heat transfer coefficient, which includes both convection and heat conduction inside of the particle, amounts to about 90 W/(m²·K) in the case 0. Therefore, a number of transfer unit referring to the solid side, NTU_S , can be obtained as 75.

Known NTU_S of 75 and R_S of 0.44, the effectiveness for the solid side, P_S , can be obtained easily from Figure 3.2 as nearly 1.0. Correspondingly the effectiveness for the gas side, P_G , is only 0.44. Therefore, the heat supply from gas, which has a value of $4.0 \cdot 10^7 \text{ W}$, can not be utilised completely through the heat exchange.

With a CO₂ fraction of 0.269 in the gas atmosphere, the decomposition of limestone begins at a temperature of 837°C. Therefore, only $9.71 \cdot 10^6 \text{ W}$ of gas heat is usable for the reaction. This corresponds to a maximum conversion degree of 0.281. This maximum value can be reached only when the limestone particle stay long enough in the system, because the reaction takes time. The real conversion degree, which will be shown later, is about 20%.

To realise a limestone conversion of 20%, about $6.92 \cdot 10^6 \text{ W}$ gas heat is required. Another part of heat consumption is the evaporation enthalpy of 1.1% water content, which needs $5.67 \cdot 10^5 \text{ W}$. Both parts together make only 18.7% of the total heat supply. Therefore the most gas heat will be consumed to raise the internal energy of the solid particles. This means, the whole system can be treated approximately as one cross flow heat exchanger, without causing significant error.

6.4 Result analysis of case 0

All the simulation results with program LEPOL are given in Attachment A as Excel diagram. As an example, only the results of case 0 are discussed in this chapter.

As mentioned before, the mass flux of gas along the grate length varies, due to the temperature distribution and thus the pressure drop difference. Because the total pressure drop in each column should be approximately the same, the mass flux distribution can be calculated iteratively. Assuming at first an equalized mass flux distribution, the pressure drop for each cell can be obtained from Equation (3.34). Summation gives total pressure drop for each column, whose deviation from average pressure drop is compared. The originally assumed mass flux distribution is modified by this deviation and then used as input for next try. After several iterations, normally from 5 to 10, an equalized total pressure drop for each column can be reached within a satisfied error range. The gas flux distribution thus obtained for case 0 is shown in Figure 6.1. At the right side (limestone entrance), the gas is drastically cooled down and has smaller density. According to Equation (3.34), the mass flux must be larger to produce the same pressure drop as the hot left end. The pressure drop distribution Figure 6.2, whose summation along each column is presented in Figure 6.3. From this figure, it is clear that the gas flux should be much unequalized: at the right end the gas flux reaches $0.75 \text{ kg}/(\text{m}^2 \cdot \text{s})$, which is 2.5 times higher than the left end.

The calculated heat transfer coefficient is shown in Figure 6.4. At the right side, the coefficient decreases drastically along the penetrating direction due to the rapid changes of gas temperature. At the left side, on the contrary, the coefficient stays nearly constant. The 1.1% moisture content in limestone layer will be quickly vaporized by the hot gas, which is shown in Figure 6.5. The conversion degree distribution in Figure 6.6 shows that only a very thin limestone layer at the top can be completely decomposed before exit. The most particles in under layer leave the system without any reaction because the gas temperature is already below the required decomposition temperature.

The temperature distribution of particle surface and gas is shown in Figure 6.7 and Figure 6.8, respectively. As the heat exchange between gas and solid particle in this system is sufficient, which can be seen from the large NTU calculated above, the two temperatures become nearly the same. The hot gas is cooled down quickly at the right side by the entering cold particles; at the same time the cold particles are heated up rapidly. At the left side, as the particles are already hot, the gas temperature can not be reduced significantly. To see the influence of gas heat upon the travelling grate, the gas exiting temperature is extra shown in Figure 6.9. At the right side where cold limestone enters, the gas can be ideally cooled down up to 20°C . At the left end where the particles have been heated up, the gas temperature can not be reduced efficiently. The hot gas reached the grate with a temperature of about 835°C . This leads to the over heating problem of the Lepol grate in the practice.

6.5 Influencing parameters

- Grate length in single-layer operation mode

Case 0, 1, 2, 3 and 4 simulate the influence of the grate length, which varies in the range from 7.7 to 69 m while other parameters are kept unchanged as in Case 0. The gas temperature distributions on the grate, which are important for protection of the grate, are compared in Figure 6.10. Other results of simulations are shown in Figure 6.11.

The gas temperature distributions on the grate are very similar. At the grate head the hot gas can be cooled down till 20°C , while at the grate end a high temperature zone of over 860°C always exists. The average gas temperatures on the grate are between 430 and 455°C , with slight difference; The maximum gas temperatures on the grate are nearly the same, from 860 to 869°C ; The average heat transfer coefficients vary from 143 to $60 \text{ W}/(\text{m}^2 \cdot \text{K})$ with increasing grate length, which can be obviously explained by reduced gas velocity by prolonged grate; The total conversion degrees stay at about 0.20 , not influenced by the grate length; The total gas heat utilisation rates, or the heat exchange effectiveness for gas, are about 0.61 , also independent of the grate length. This means only 61% of the heat supply from gas is consumed for drying, heating up and reaction of limestone.

It can be seen that changing the grate length in above mentioned range has nearly no influence upon the gas temperature distribution on the grate, the maximum temperature, or the total conversion degree. Therefore the grate can not be protected from the high gas temperature by the means of changing the grate length. But as longer grate has no any advantage, it can be recommended to build shorter grate in the future to save cost and place.

- Gas input temperature in single-layer operation mode

Case 0, 5, 6, 7 and 8 simulate the influence of the gas input temperature, which varies in the range from 950 to 1250°C while other parameters are kept unchanged as in Case 0. The gas temperature distributions on the grate, which are important for protection of the grate, are compared in Figure 6.12. Other results of simulations are shown in Figure 6.13.

The gas temperature distributions on the grate are very similar. At the grate head the hot gas can be cooled down till 20°C, while at the grate end a high temperature zone of over 860°C always exists. The average gas temperatures on the grate are between 402 and 461°C, with small difference; The maximum gas temperatures on the grate are nearly the same, from 859 to 869°C; The average heat transfer coefficients vary from 82 to 98 W/m²/K with increasing gas input temperature, which can be obviously explained by increasing gas velocity due to temperature; The total conversion degrees increase from 0.07 to 0.31 with increasing gas input temperature; The total gas heat utilisation rates change from 0.61 to 0.64, with slight difference.

It can be seen that changing the gas input temperature in above mentioned range has large influence only upon the total conversion degree. In another word, the additional heat input due to increased gas temperature will contribute mainly to a better decomposition of limestone. Therefore the gas temperatures on the grate stay more or less the same. The grate can not be protected by only reduce the gas temperature from the rotary kiln.

- Gas input in single-layer operation mode

Case 0, 9, 10, 11 and 12 simulate the influence of the gas input, which varies in the range from 9.6 to 86.5 kg/s while other parameters are kept unchanged as in Case 0. The gas temperature distributions on the grate, which are important for protection of the grate, are compared in Figure 6.14. Other results of simulations are shown in Figure 6.15.

The gas temperature distributions on the grate are very different. With small gas input as 9.6 kg/s, the hot gas can be cooled down till 20°C at whole grate. At another extreme, with gas input of 86.5 kg/s, two third of the grate will be exposed to high gas temperature as 879 °C. The average gas temperatures on the grate increases from 20 to 734°C with increasing gas input; The maximum gas temperatures on the grate increase from 28 to 879°C; The average heat transfer coefficients vary from 50 to 149 W/m²/K with increasing gas input, which can be obviously explained by increasing gas velocity due to gas input; The total conversion degrees increase from 0.08 to 0.59 with increasing gas input; The total gas heat utilisation rates change from 1.0 to 0.33, with very large difference.

It can be seen that changing the gas input in above mentioned range has very large influence upon the whole process, because of the drastic variation range. For the sake of grate protection, the most effective way is to reduce the gas heat input. To reduce the maximum gas temperature on the grate to 800°C, the gas input must be limited by about 24 kg/s, namely 83% of the original input of 28.8 kg/s. The rest 17% hot gas amount must diverted from the rotary kiln head to another facility instead of the grate, or simply set free. If a maximum gas temperature on the grate of 700°C is desired, only 21 kg/s hot gas input is allowed to enter the grate, corresponding to 73% of the original hot gas input. This method, however, will sacrifice some conversion degree.

- Dust input in single-layer operation mode

In the simulation, the input of hot gas is treated similarly as hot gas Case. It is regarded to have the same specific heat capacity. The difference is that dust does not contribute to gas volume, and therefore does not affect the gas velocity.

Case 0, 13 and 14 simulate the influence of the hot dust input with the same temperature as the hot gas, which is introduced by the gas flow. In the simulation, the dust input varies in the range from 0.83 to 3.33 kg/s while other parameters are kept unchanged as in Case 0. The gas temperature distributions on the grate, which are important for protection of the grate, are compared in Figure 6.16. Other results of simulations are shown in Figure 6.17.

Due to the small variation range of dust input, the gas temperature distributions on the grate have slight difference. The influence of dust input is similar to that of gas input temperature. In a zone of about 5 m at the grate head, the hot gas can be cooled down till 20°C, while at the grate end a high temperature zone of over 860°C always exists. The average gas temperatures on the grate increases from 422 to 466°C with increasing dust input; The maximum gas temperatures on the grate are between 864 and 868°C, nearly the same; The average heat transfer coefficients are between 88 and 94 W/(m²·K), nearly the same. The reason is that the dust input does not increase the volume flow rate of gas. The total conversion degrees stay at about 0.20, showing no difference; the total gas heat utilisation rates change from 0.63 to 0.60, decreasing with more dust input.

It can be seen that changing the dust input in above mentioned small range has nearly no influence upon the whole process.

- Stone layer height in single-layer operation mode

Case 0, 15, 16, 17 and 18 simulate the influence of the stone layer height, which varies in the range from 0.18 to 1.8 m while other parameters are kept unchanged as in Case 0. With the same limestone throughput, larger stone layer height means automatic slower grate velocity in the simulation. The gas temperature distributions on the grate, which are important for protection of the grate, are compared in Figure 6.18. Other results of simulations are shown in Figure 6.19.

The gas temperature distributions on the grate are very different. The higher the stone layer, more drastic will be the gas temperature distribution on the grate. With the stone layer height as 1.8 m, the gas distribution has a big cold zone at grate head and a big hot zone at the grate end, which is much undesired for protection of the grate. With smaller stone layer height, the gas temperature distribution on the grate is more equalized. For example in the case of 0.18 m, both the hot and cold zones tend to disappear. The average gas temperatures on the grate decreases from 466 to 435°C with increasing stone layer height; The maximum gas temperatures on the grate increase from 852 to 868°C; The average heat transfer coefficients stay exactly at 90 W/(m²·K), independent on the stone layer height; The total conversion degrees increase from 0.17 to 0.23 with increasing stone layer height; The total gas heat utilisation rates change from 0.60 to 0.62, with small difference.

It can be seen that changing the stone layer height in above mentioned range has pretty significant influence upon the gas distribution on the grate, but not much on average gas temperature, heat transfer or the total gas heat utilisation rate. For the sake of grate protection, it is of advantage to operate the grate with smaller stone layer height and quicker grate velocity. This can reduce the length of the hot gas zone on the grate.

- Limestone throughput in single-layer operation mode

Case 0, 19, 20, 21 and 22 simulate the influence of the limestone input, which varies in the range from 6.9 to 61.9 kg/s while other parameters are kept unchanged as in Case 0. The gas temperature distributions on the grate, which are important for protection of the grate, are compared in Figure 6.20. Other results of simulations are shown in Figure 6.21.

Because of the large variation range, the gas temperature distributions on the grate are very different. With small limestone input as 6.9 kg/s, a big hot gas zone on the grate, as long as 16 m, can be expected. When the limestone input is larger than 21 kg/s, the hot gas zone tends to disappear. With extreme large limestone input as 61.3 kg/s, the whole grate is then cold zone with about 20°C. The average gas temperatures on the grate decreases from 731 to 23°C with increasing limestone input; The maximum gas temperatures on the grate increase from 869 to 60°C with increasing limestone input; The average heat transfer coefficients decreases somewhat from 96 to 70 W/(m²·K) with increasing limestone input; The total conversion degrees decrease from 0.58 to 0.05 with increasing limestone input; The total gas heat utilisation rates change from 0.33 to 1.0, increasing with limestone input.

It can be seen that larger limestone input has a similar effect as smaller gas input. To protect the grate, it is of advantage to increase the limestone throughput as much as possible, if the process in the rotary kiln allows. This operation, theoretically, can reduce the length of the hot gas zone on the grate, or the maximum gas temperature.

- Particle size in single-layer operation mode

Case 0, 23, 24, 25 and 26 simulate the influence of the particle size, which varies in the range from 5 to 25 mm while other parameters are kept unchanged as in Case 0. The gas temperature distributions on the grate, which are important for protection of the grate, are compared in Figure 6.22. Other results of simulations are shown in Figure 6.23.

The gas temperature distributions on the grate are very different. Increasing the particle size has the similar effect as decreasing the stone layer height. The smaller the particle size, more drastic will be the gas temperature distribution on the grate. With the size of 5 mm, the gas distribution has a big cold zone at grate head and a big hot zone at the grate end, which is much undesired for protection of the grate. With a bigger particle size, the gas temperature distribution on the grate is more equalized. For example in the case of 25 mm, both the hot and cold zones tend to disappear. The average gas temperatures on the grate increases slightly from 458 to 462°C with particle size; The maximum gas temperatures on the grate decrease from 869 to 846°C with particle size; The average heat transfer coefficients decrease drastically from 163 to 60 W/(m²·K) with particle size; The total conversion degrees decrease from 0.34 to 0.17 with particle size; The total gas heat utilisation rates change from 0.58 to 0.62, with small variation.

It can be seen that changing the limestone particle size in above mentioned range has pretty significant influence upon the gas distribution on the grate and conversion degree, but not much on average gas temperature, heat transfer or the total gas heat utilisation rate. For the sake of grate protection, it is of advantage to operate the grate with larger particle size. This can reduce the length of the hot gas zone on the grate or the maximum gas temperature.

- Limestone layer porosity size in single-layer operation mode

Case 0, 27 and 28 simulate the influence of the limestone layer porosity, which varies in the range from 0.35 to 0.5 while other parameters are kept unchanged as in Case 0. The gas temperature distributions on the grate, which are important for protection of the grate, are compared in Figure 6.24. Other results of simulations are summarized in Figure 6.25.

The gas temperature distributions on the grate are nearly the same. The average gas temperatures on the grate are between 434 and 438°C, nearly the same; The maximum gas temperatures on the grate decrease from 868 to 864°C, nearly the same; The average heat transfer coefficients decrease slightly from 95 to 85 W/(m²·K) with increasing porosity; The total conversion degrees stay at 0.20; The total gas heat utilisation rates stay at 0.62.

It can be seen that changing the limestone layer porosity in above mentioned range has nearly no influence upon the gas distribution on the process on the grate.

- Gas input temperature in two-layer operation mode

Case 29, 30, 31, 32 and 33 in two-layer operation mode simulate the influence of the gas input temperature, which varies in the range from 950 to 1250°C while other parameters are kept unchanged as in Case 29. The gas temperature distributions on the grate, which are important for protection of the grate, are compared in Figure 6.26. Other results of simulations are summarised in Figure 6.27.

The gas temperature distributions on the grate are very similar. At the grate head the hot gas can be cooled down till 20°C, while at the grate end a high temperature zone of over 830°C always exists. The average gas temperatures on the grate are between 403 and 453°C, with small difference; The maximum gas temperatures on the grate are nearly the same, from 832 to 853°C, which is about 30°C lower than the single-layer operation mode; The top layer consists of smaller particle of 8.8 mm; therefore the average heat transfer coefficient is much bigger (between 105 and 123 W/(m²·K)) than bottom layer of size 22.3 mm (between 51 and 63 W/(m²·K)). The average heat transfer coefficients for whole stone layer vary from 78 to 94 W/(m²·K) with increasing gas input temperature, which can be obviously explained by increasing gas velocity due to temperature; In given condition, only the top layer can be decomposed with an average conversion degree between 0.15 and 0.60, increasing significantly with gas input temperature. The bottom layer can not be decomposed. The total conversion degree, which ranges from 0.08 to 0.30, is the same as single-layer operation; the total gas heat utilisation rates change from 0.61 to 0.64, with slight difference, same as single-layer operation.

It can be seen that changing the gas input temperature in above mentioned range has large influence only upon the total conversion degree. In another word, the additional heat input due to increased gas temperature will contribute mainly to a better decomposition of top layer. Therefore the gas temperatures on the grate stay more or less the same. The grate can not be protected by only reduce the gas temperature from the rotary kiln.

- Gas input in two-layer operation mode

Case 29, 34, 35, 36 and 37 simulate the influence of the gas input, which varies in the range from 9.6 to 86.5 kg/s while other parameters are kept unchanged as in Case 29. The gas temperature distributions on the grate, which are important for protection of the grate, are compared in Figure 6.28. Other results of simulations are shown in Figure 6.29.

The gas temperature distributions on the grate are very different. With small gas input as 9.6 kg/s, the hot gas can be cooled down till 20°C in a cold zone as long as 20m. At another extreme, with gas input of 86.5 kg/s, the half of the grate will be exposed to high gas temperature as over 880°C. The average gas temperatures on the grate increases from 28 to 735 °C with increasing gas input; The maximum gas temperatures on the grate increase from 108 to 869°C; The top layer of small particle of 8.8 mm has a bigger average heat transfer coefficient, ranging from 75 to 175 W/(m²·K); The down layer of big particle of 22.3 mm has a smaller average heat transfer coefficient, ranging from 27 to 103 W/(m²·K); The average heat transfer coefficients in whole layer vary from 51 to 140 W/(m²·K). All the coefficients increase with gas input, which can be obviously explained by increasing gas velocity due to gas input; The conversion degrees of top layer increase from 0.18 to 0.98 drastically with increasing gas input; The conversion degrees of bottom layer increase from 0 to 0.14 with increasing gas input as well; The whole average conversion degrees are between 0.09 and 0.56, same to the single-layer operation. The total gas heat utilisation rates change from 0.99 to 0.33, with very large difference.

It can be seen that changing the gas input in above mentioned range has very large influence upon the whole process, because of the drastic variation range. For the sake of grate protection, the most effective way is to reduce the gas heat input, same as in the single-layer operation.

- Other variations

In Case 38 the top layer consists of big particle of 22.3 mm, the bottom layer is small particle of 8.8mm, which is inverse to Case 29. The comparison shows it is of advantage to put smaller particle on the top, because then the total average heat gas heat utilisation rate is better (0.63 vs. 0.60), the total average conversion degree is bigger (0.21 vs. 0.17), the average gas temperature is lower (431 vs. 463°C) as well as the maximum gas temperature (845 vs. 869°C).

In Case 39 the limestone particles are sieved and separated differently (7.24 kg of 7.5 mm in top layer and 13.37 kg of 20.5 mm in bottom layer) than in Case 29 (10.31 kg of 8.8 mm in top layer and 10.31 kg of 22.3 mm in bottom layer). The result shows no difference, except for the obvious fact that smaller size will have a bigger conversion degree under the same condition.

In Figure 6.30 the distributions of gas temperature on the grate of above mentioned several operation mode are compared. It is obvious that the two-layer operation mode with finer fraction on the top is of advantage, because in this case the gas exit temperature is more averaged and the peak temperature is lower.

6.6 Suggestions

The main purpose of above simulation is try to find some methods to decrease the average temperature or the peak temperature of the hot gas when it reaches the Lepol grate, in order to protect the grate material from the gas heat. According to above simulations, the grate segments can be protected from over heat of the gas by several ways:

- If the grate is operated with larger grate velocity and correspondingly smaller limestone bed height;
- If the grate is operated with two-layer limestone bed with the finer fraction on the top;
- If the limestone particles are larger;
- If the heat introduced by the hot gas is reduced by reduce, for example, the gas input temperature, the hot dust amount, or the hot gas amount. Reducing the hot gas amount is more effective to limit the whole gas heat introduction, and is easier to realize by use a hot gas bypass at the roof of hot gas chamber.

In applying a bypass in hot gas chamber and set free a part of the hot gas will lead to other questions, for example, how to recycle the enthalpy of this gas flow, and how to treat this gas flow to abide by the strict environmental requirements. Because of its high temperature and heavy load of dust, it deserves further discussion.

7. Simulation and result with the model CLINKER

7.1 Operation data

Tables 7.1 describes a real grate cooler for clinker, which is installed at the output end of a clinker rotary kiln and used for cooling down the hot clinker particles.

Table 7.1 Operation data of a grate cooler for clinker

Parameter	Definition	Unit	Value
Length	Length of the grate	m	20
Width	Width of the grate	m	4
MS	Mass throughput of the particles	t/d	3000
Por	Porosity of the particle bed	-	0.4
D	Equivalent diameter of the particles	m	0.01
Wb	Speed of grate	m/min	1.0
Height	Bed depth of the fine grain fraction	m	0.275
TO00	Stone temperature at entrance	°C	1400
TRef	Reference temperature	°C	20
TG00	Air temperature at entrance	°C	20
MG	Mass flow of air	Kg/s	79.68
Pt	Air pressure	Pa	101325
Lambda	Thermal conductivity of clinker	W/(m·K)	0.65
CpS	Heat capacity of clinker	J/(kg·K)	920
DenS	Density of clinker	kg/m ³	2700

7.2 Simulation cases

Some scenarios are simulated for the grate cooler for clinker. The parameters and some simulation results are listed in Table 7.2.

Table 7.2 Simulation scenarios of a grate cooler for clinker

Case	Wb (m/min)	D (mm)	L (m)	MG (kg/s)	MS (kg/s)	Por (-)	Ave. TG (°C)	Ave. TS (°C)	Ave. Alpha (W/(m ² ·K))	CoolRate (K/s)	ΔWG (m/s)	ΔWG/WG (-)
0	1.0	10.0	20.0	79.7	34.7	0.4	55.9	24.4	93.0	1.15	1.90	0.86
1	0.333	10.0	20.0	79.7	34.7	0.4	53.2	20.3	93.2	0.38	1.82	0.81
2	0.5	10.0	20.0	79.7	34.7	0.4	55.0	20.9	93.3	0.57	1.84	0.82
3	2.0	10.0	20.0	79.7	34.7	0.4	52.4	32.9	91.7	2.29	2.02	0.96
4	3.0	10.0	20.0	79.7	34.7	0.4	51.5	42.9	90.2	3.40	2.10	1.06
5	1.0	3.33	20.0	79.7	34.7	0.4	45.6	20.0	190.9	1.15	-1.38	-0.62
6	1.0	5.0	20.0	79.7	34.7	0.4	49.5	20.2	145.5	1.15	0.16	0.07
7	1.0	20.0	20.0	79.7	34.7	0.4	54.0	45.2	59.1	1.13	3.73	1.88
8	1.0	30.0	20.0	79.7	34.7	0.4	51.2	76.0	44.7	1.10	5.13	2.98
9	1.0	10.0	6.67	79.7	34.7	0.4	58.1	34.5	140.4	3.41	-2.66	-0.42
10	1.0	10.0	10.0	79.7	34.7	0.4	56.7	29.4	120.6	2.28	0.12	0.03
11	1.0	10.0	40.0	79.7	34.7	0.4	50.5	21.6	72.5	0.57	2.47	2.22
12	1.0	10.0	60.0	79.7	34.7	0.4	46.2	20.8	63.4	0.38	2.63	3.54
13	1.0	10.0	20.0	26.6	34.7	0.4	87.6	43.1	79.5	1.13	3.63	2.79
14	1.0	10.0	20.0	39.8	34.7	0.4	73.3	33.2	83.2	1.14	2.86	1.78
15	1.0	10.0	20.0	159	34.7	0.4	40.8	20.9	110.0	1.15	0.73	0.24
16	1.0	10.0	20.0	239	34.7	0.4	35.3	20.3	124.3	1.15	-1.26	-0.32
17	1.0	10.0	20.0	79.7	11.6	0.4	32.8	21.3	80.4	1.15	2.03	1.53
18	1.0	10.0	20.0	79.7	17.4	0.4	39.0	21.9	83.8	1.15	1.99	1.28
19	1.0	10.0	20.0	79.7	69.4	0.4	83.0	32.0	107.4	1.14	1.67	0.51
20	1.0	10.0	20.0	79.7	104	0.4	101.5	42.2	118.3	1.13	1.24	0.31

21	1.0	10.0	20.0	79.7	34.7	0.3	53.7	23.6	99.3	1.15	1.88	0.85
22	1.0	10.0	20.0	79.7	34.7	0.5	55.6	25.0	86.6	1.14	1.92	0.88

7.3 Rough energy balance

Similar to the model LEPOL, the whole clinker-air-system on the travelling grate can be treated as a large cross flow heat exchanger for a rough energy balance. There is no reaction or evaporation in the model, therefore the following energy balance should be more close to the numerical results.

In case 0 of Table 7.2, the typical cooling air input is 79.7 kg/s at 20°C. With a heat capacity of 987 J/(kg·K), the heat capacity flow of air is then $7.87 \cdot 10^4$ W/K. Clinker particles enter the system with a mass flow of 34.7 kg/s and an estimated heat capacity of 900 J/(kg·K), which give a heat capacity flow of $3.12 \cdot 10^4$ W/K. The ratio R_S is therefore 40%.

The given clinker throughput and grate speed determines a particle layer of 0.32m. The big dimension of the layer (20m×4m×0.32m) and the small particle diameter (10mm) provide a large heat transfer area of $9.25 \cdot 10^3$ m² for the total bed, taking into account a void fraction of 0.40. The average effective heat transfer coefficient, which includes both convection and heat conduction inside of the particle, amounts to 93 W/(m²·K), similar as in model LEPOL. Therefore, a number of transfer unit referring to the solid side, NTU_S , can be obtained as 27.6. From Figure 3.2, the effectiveness for the clinker side can be obtained easily as 1.0 and that for the gas side as 0.40. From this rough balance, the clinker particles can be cooled down completely till nearly 20°C.

7.4 Result analysis of case 0

All the simulation results with program CLINKER are presented in Attachment B as Excel diagram. For simplicity, only the results of case 0 are discussed in this chapter.

The mass flux distribution of air along the grate length is, similar to model LEPOL, determined iteratively by the criteria of equalized pressure drop. The pressure drop distribution for case 0 is shown in Figure 7.1, whose summation along each column is presented in Figure 7.2. The air flux reaches 0.9 kg/(m²·s) at left end where both clinker and air are cold. At the right hot end, air flux is only about 0.5 kg/(m²·s).

The heat transfer coefficient is shown in Figure 7.3. At the right side, the coefficient decreases drastically along the air direction due to the rapid changes of temperature. The temperature distribution of clinker surface and air is shown in Figure 7.4 and Figure 7.5, respectively. The similarity of both demonstrates a fast ideal heat exchanger.

Figure 7.6 shows the minimal fluidisation velocity (as empty tube velocity), which is mainly decided by the air temperature. As the air from the right end (entrance of hot clinker) exits, it assumes a temperature of 1400°C. Therefore the minimal fluidisation velocity for 10 mm particles is larger (about 6 m/s) than the left side (about 3 m/s). But in Figure 7.7, the real air velocity (as empty tube velocity) has the same tendency, but all under the limit. Where can particle fluidization happen, should be devalued with the velocity difference at the surface, which is depicted in Figure 7.8. It is clear that at the left side the velocity margin, and therefore the potential of particle fluidisation, is more critical than the right side.

7.5 Influencing parameters

- Grate velocity

Case 0, 1, 2, 3 and 4 simulate the influence of the grate velocity, which varies in the range from 0.33 to 3 m/min while other parameters are kept unchanged as in Case 0. With the same clinker throughput, larger rate velocity means smaller clinker layer height in the simulation.

The minimal fluidisation velocity and the real gas velocity distributions on clinker layer surface are compared in Figure 7.9. The fluidisation potentials are summarised in Figure 7.10. The exit temperatures of clinker and air, and the average cooling rate of clinker are illustrated in Figure 7.11. The average heat transfer coefficients are shown in Figure 7.12.

The distributions of both velocities will be more equalized with larger grate velocity. The minimal fluidisation velocities decline along the grate moving direction, independent of the grate velocity. With big grate velocity, the gas velocities decrease also slightly in this direction. But for small grate velocity, for example 0.33 m/min, a maximum gas velocity appears at grate length 7 m. In the whole variation range of the grate velocity, no fluidisation can be observed. The minimal velocity differences are always about 2 m/s, or 100% of the real gas velocity.

The average exit temperature of air remain approximately 55°C, while that of clinker increases from 20 to 43°C with the grate velocity. The average cooling rate of clinker changes from 0.38 to 3.4 K/s.

The heat transfer coefficients remain about 92 W/(m²·K), independent on the grate velocity.

It can be seen that changing the grate velocity in above mentioned range has no influence upon the possibility of clinker fluidisation. But to improve the clinker quality, a large grate velocity has surely advantage.

- Particle size

Case 0, 5, 6, 7 and 8 simulate the influence of the clinker particle size, which varies in the range from 3.3 to 30 mm while other parameters are kept unchanged as in Case 0.

The minimal fluidisation velocity and the real gas velocity distributions on clinker layer surface are compared in Figure 7.13. The fluidisation potentials are summarised in Figure 7.14. The exit temperatures of clinker and air, and the average cooling rate of clinker are illustrated in Figure 7.15. The average heat transfer coefficients are shown in Figure 7.16.

The minimal fluidisation velocities decline slightly along the grate moving direction. Big particles need a higher minimal fluidisation velocity. At the grate length 10 m, for example, particles of 3.3 mm need 2.2 m/s, while particles of 30 mm need 7.4 m/s as minimal fluidisation velocity. The real gas velocities, however, remain more or less the same, independent of the particle size. For small particles, for example 3.3 mm, a maximum gas velocity appears at grate length 10 m. Under given conditions the clinker particles smaller than 5 mm will be fluidised by the air.

The average exit temperature of air remain approximately between 45 and 55°C, while that of clinker increases from 20 to 75°C with the particle size. The average cooling rate of clinker does not change, remaining 1.2 K/s.

The heat transfer coefficients decrease drastically from 191 to 45 W/(m²·K) with increasing particle size.

It can be seen that the particle size is decisive for the phenomena of clinker fluidisation. Under given conditions the clinker particle smaller than 5 mm will be fluidised by the air. Although the heat transfer coefficient is affected drastically by the particle size, the average cooling rate does not. This leads to the same clinker quality formation.

- Grate length

Case 0, 9, 10, 11 and 12 simulate the influence of the grate length, which varies in the range from 6.7 to 60 m while other parameters are kept unchanged as in Case 0.

The minimal fluidisation velocity and the real gas velocity distributions on clinker layer surface are compared in Figure 7.17. The fluidisation potentials are summarised in Figure 7.18. The exit temperatures of clinker and air, and the average cooling rate of clinker are illustrated in Figure 7.19. The average heat transfer coefficients are shown in Figure 7.20.

The minimal fluidisation velocities decline along the grate moving direction, from about 6.1 m/s at grate head to about 3.2 m/s at the grate end, independent of the grate length. Because of different cross section for air flow, the real air velocities decrease with the given grate length correspondingly. Therefore a short grate, when it is shorter than 10 m under the given conditions, will lead to clinker fluidisation.

The average exit temperature of air decreases slightly from 58 to 46°C, while that of clinker decreases from 35 to 21°C with the grate length. The average cooling rate of clinker declines drastically from 3.4 to 0.4 1.2 K/s with increasing grate length.

The heat transfer coefficients decrease from 140 to 62 W/(m²·K) with increasing grate length, which can be explained by the air velocity as well.

It can be seen that the grate length is also important for the phenomena of clinker fluidisation. Under given conditions the clinker particle will be fluidised by the air if the grate is shorter than 10 m. However, a shorter grate will bring quicker cooling down of clinker particle, which means better product quality.

- Air input

Case 0, 13, 14, 15 and 16 simulate the influence of the air input amount, which varies in the range from 26.6 to 239 kg/s while other parameters are kept unchanged as in Case 0.

The minimal fluidisation velocity and the real gas velocity distributions on clinker layer surface are compared in Figure 7.21. The fluidisation potentials are summarised in Figure 7.22. The exit temperatures of clinker and air, and the average cooling rate of clinker are illustrated in Figure 7.23. The average heat transfer coefficients are shown in Figure 7.24.

Generally, with increasing air input, the minimal fluidisation velocities decrease while the real gas velocities increase. With large air input more than 190 kg/s the fluidisation of clinker particles will take place, especially near the grate head.

The average exit temperature of air decreases from 88 to 35°C, while that of clinker decreases from 42 to 20°C with the increasing air input amount. The average cooling rate of clinker, however, remains 1.2, independent of air input amount.

The heat transfer coefficients increase from 80 to 123 W/(m²·K) with increasing air input amount, which can be explained by the air velocity.

It can be seen that the air input amount is also important for the phenomena of clinker fluidisation. Under given conditions the clinker particle will be fluidised by the air if the air input amount exceeds 190 kg/s. Therefore, to reduce the air input amount can help avoid particle fluidisation. A reduction up to 26.6 kg/s will not worsen significantly the clinker quality.

- Clinker throughput

Case 0, 17, 18, 19 and 20 simulate the influence of the clinker throughput, which varies in the range from 11.6 to 104 kg/s while other parameters are kept unchanged as in Case 0.

The minimal fluidisation velocity and the real gas velocity distributions on clinker layer surface are compared in Figure 7.25. The fluidisation potentials are summarised in Figure 7.26. The exit

temperatures of clinker and air, and the average cooling rate of clinker are illustrated in Figure 7.27. The average heat transfer coefficients are shown in Figure 7.28.

Different than the effect of air input, both the minimal fluidisation velocities and the real gas velocities increase with increasing clinker input amount. In the whole variation range of the clinker input, no fluidisation will take place. The differences between the gas velocity and the minimal fluidisation velocity are between 1.2 and 2 m/s, decreasing slightly with the clinker input.

The average exit temperature of air increases from 34 to 102°C, while that of clinker increases from 21 to 41°C with the increasing clinker input amount. The average cooling rate of clinker, however, remains 1.2, independent of clinker input amount.

The heat transfer coefficients increase from 80 to 119 W/(m²·K) with increasing air input amount.

To the contrary of the air input amount, the clinker throughput is not so important for avoiding fluidisation. It has either no influence upon the cooling rate or quality of clinker particles.

- Clinker layer porosity

Case 0, 21 and 22 simulate the influence of the clinker layer porosity, which varies in the range from 0.3 to 0.5 while other parameters are kept unchanged as in Case 0.

The minimal fluidisation velocity and the real gas velocity distributions on clinker layer surface are compared in Figure 7.29. The fluidisation potentials are summarised in Figure 7.30. The exit temperatures of clinker and air, and the average cooling rate of clinker are illustrated in Figure 7.31. The average heat transfer coefficients are shown in Figure 7.32.

It can be seen that the clinker layer porosity in above mention variation range has nearly no influence on fluidisation or cooling rate of clinker. Only the heat transfer coefficients decrease from 100 to 86 W/m²/K with increasing porosity.

7.6 Suggestions

The purpose of the simulation of above grate clinker-cooling system is to find some methods to avoid the fluidisation of smaller clinker particles, which is a limiting factor for increasing the cooling capacity of a given apparatus. On the other hand the rapid cooling of hot clinker must be reached by the system to obtain a desired crystal structure inside the clinker, which means a good quality for cement.

The cooling effect of clinker particles can be improved by a prolonged grate, a smaller grate velocity (means correspondingly a bigger clinker particle bed height), an increased air input amount, a smaller clinker throughput or smaller clinker particles.

The fluidisation phenomena of smaller clinker particles can be avoided by a prolonged grate, a rapid grate velocity (means correspondingly a smaller clinker particle bed height), smaller air input amount, smaller clinker throughput or bigger clinker particle size.

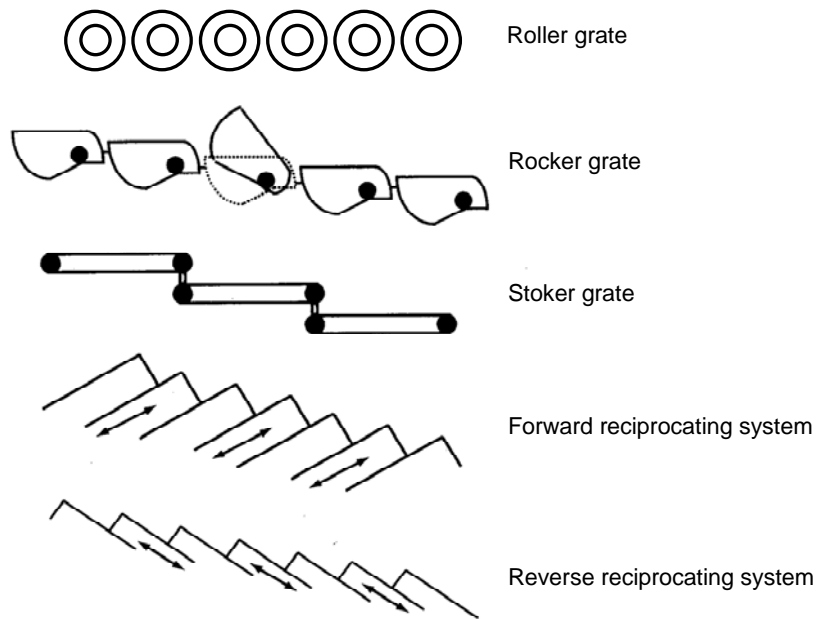


Figure 1.1 Some types of moving grate (modified from Clayton et al. 1991)

1

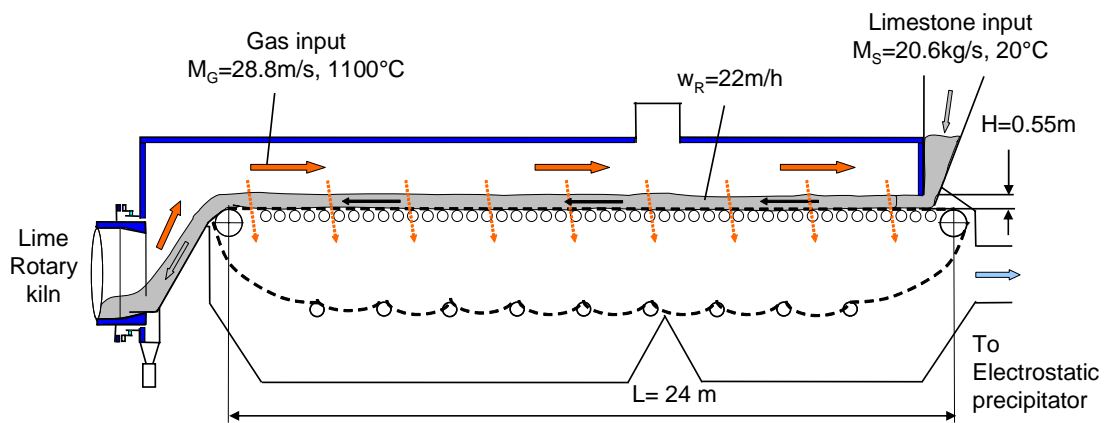


Figure 2.1 A typical Lepol grate for preheating of limestone before rotary kiln

2

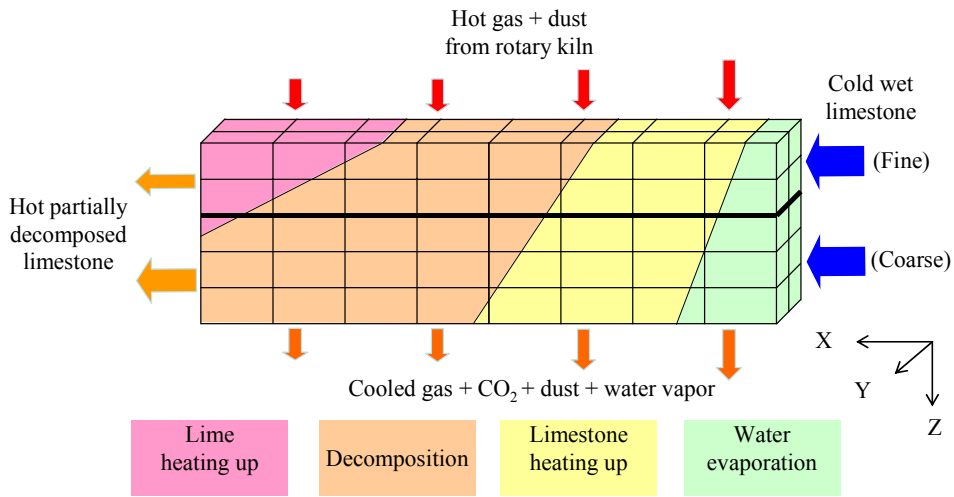


Figure 2.2 Processes on the Lepol grate for preheating of limestone

3

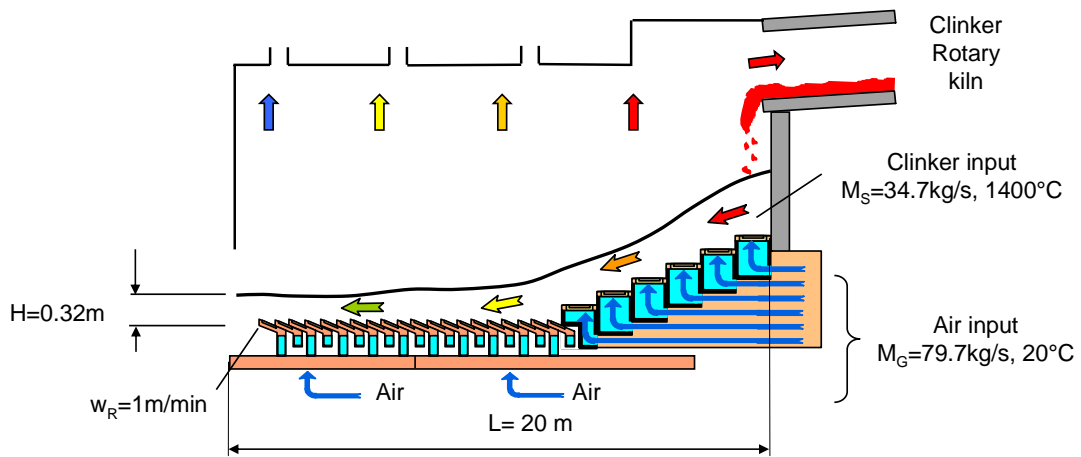


Figure 2.3 A typical clinker grate cooler

4

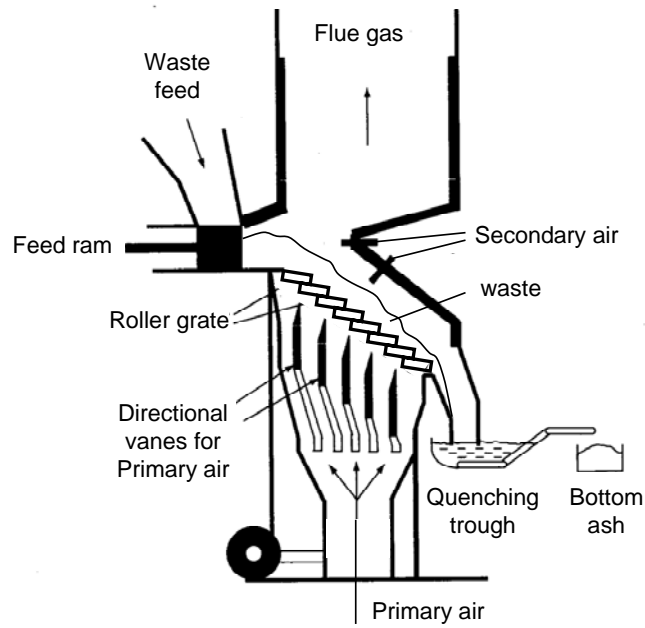


Figure 2.4 A typical grate incineration system for municipal solid waste (modified from Clayton et al. 1991)

5

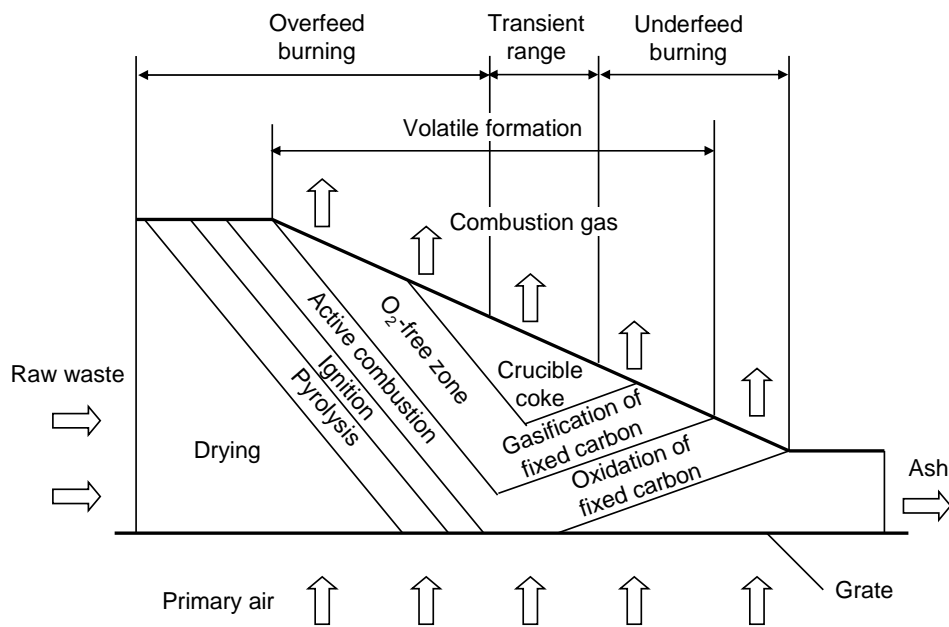


Figure 2.5 Processes on a grate incineration for municipal solid waste (modified from Clayton et al. 1991)

6

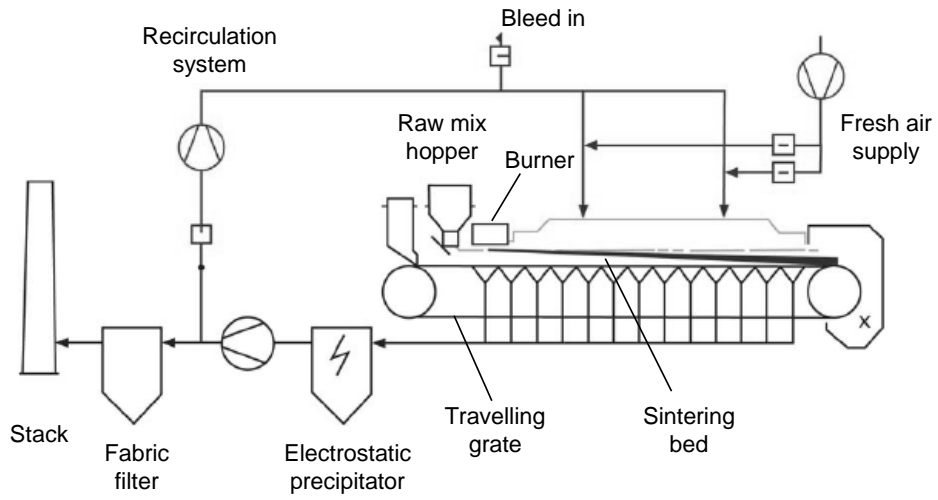


Figure 2.6 A typical sintering plant of iron raw mix

7

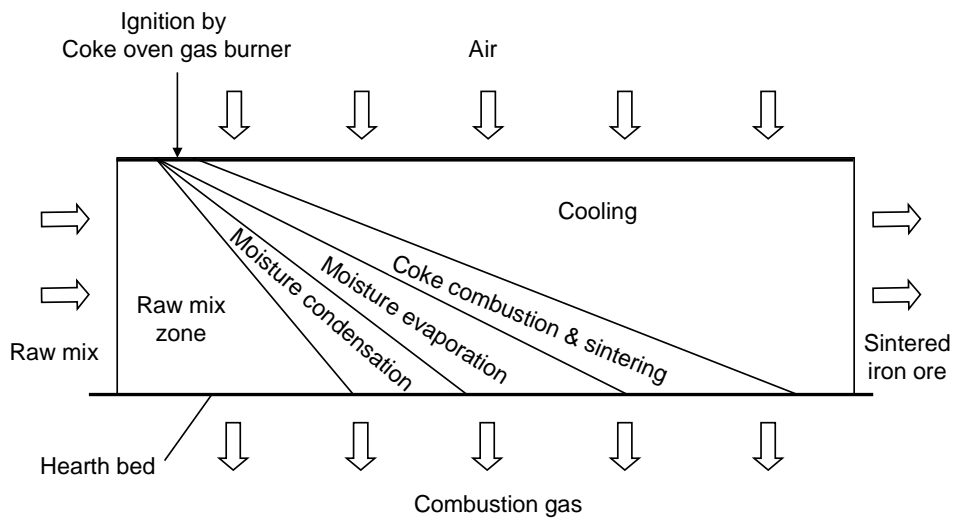


Figure 2.7 Processes on a sintering grate for iron raw mix (modified from W. Yang et al. 2003)

8

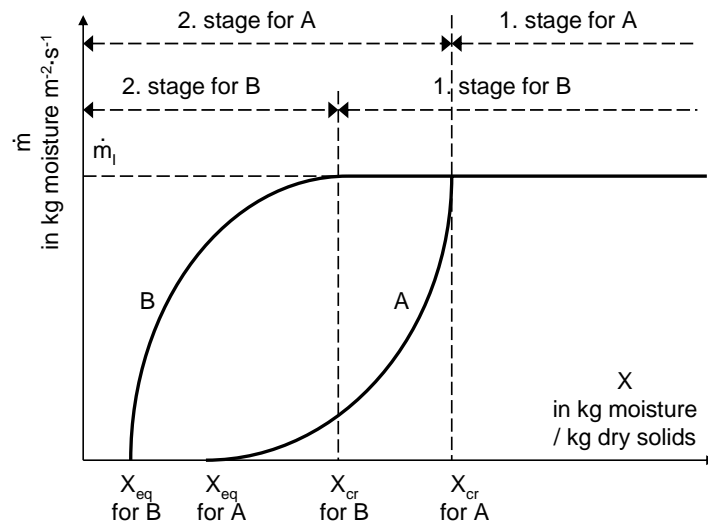


Figure 3.1 Drying behaviour of two types of solid

9

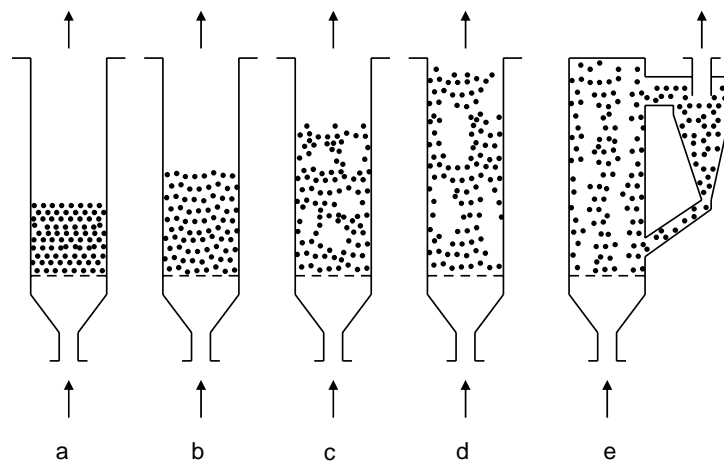


Figure 3.2 Fluidisation of solid particle bed

10

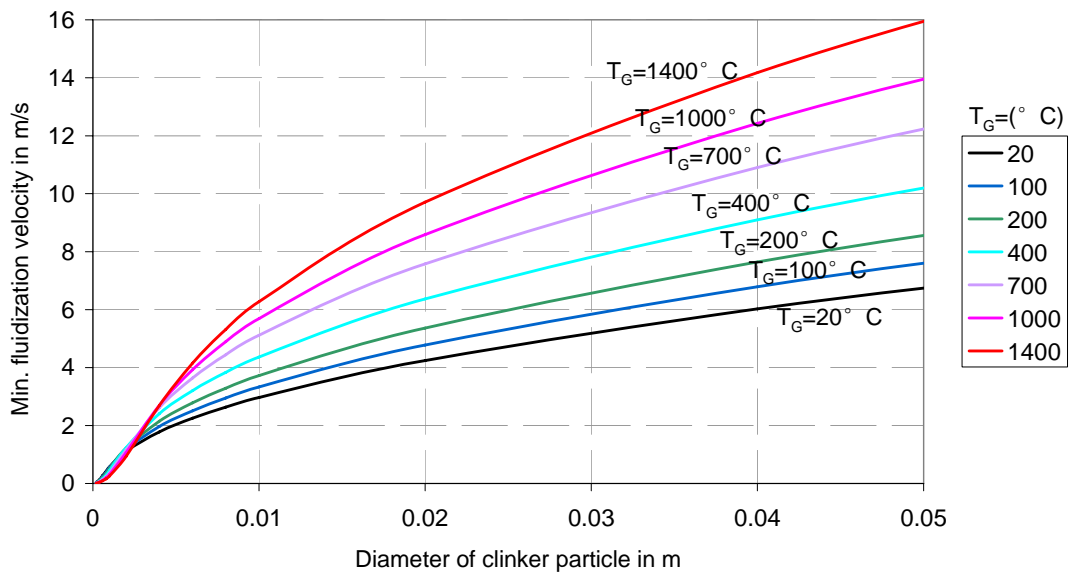


Figure 3.3 Minimal fluidisation velocity of clinker particle

11

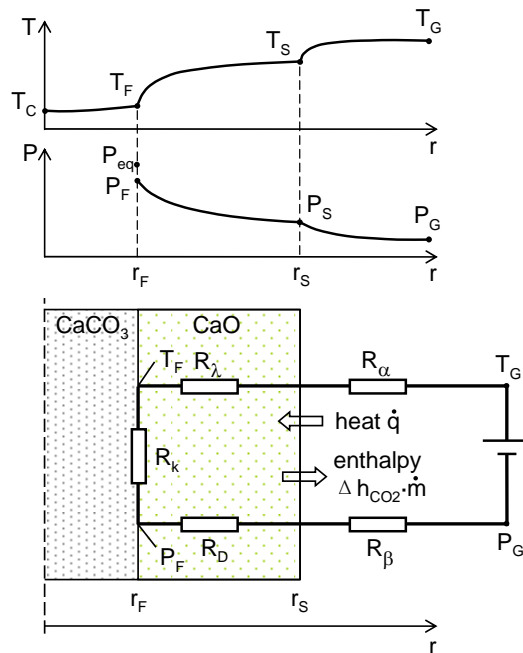


Figure 3.4 Model of limestone decomposition

12

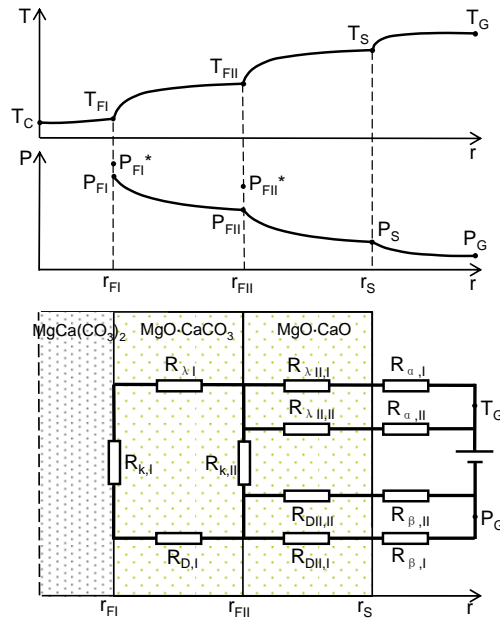


Figure 3.5 Model of simultaneous dolomite decomposition

13

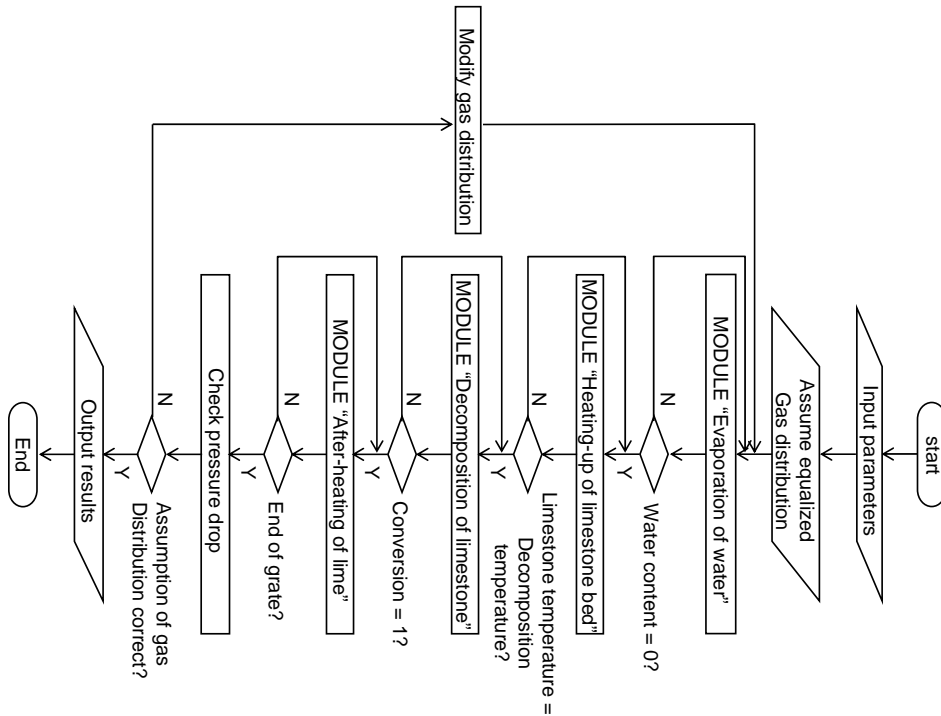


Figure 4.1 Flow chart of program LIMESTONE

14

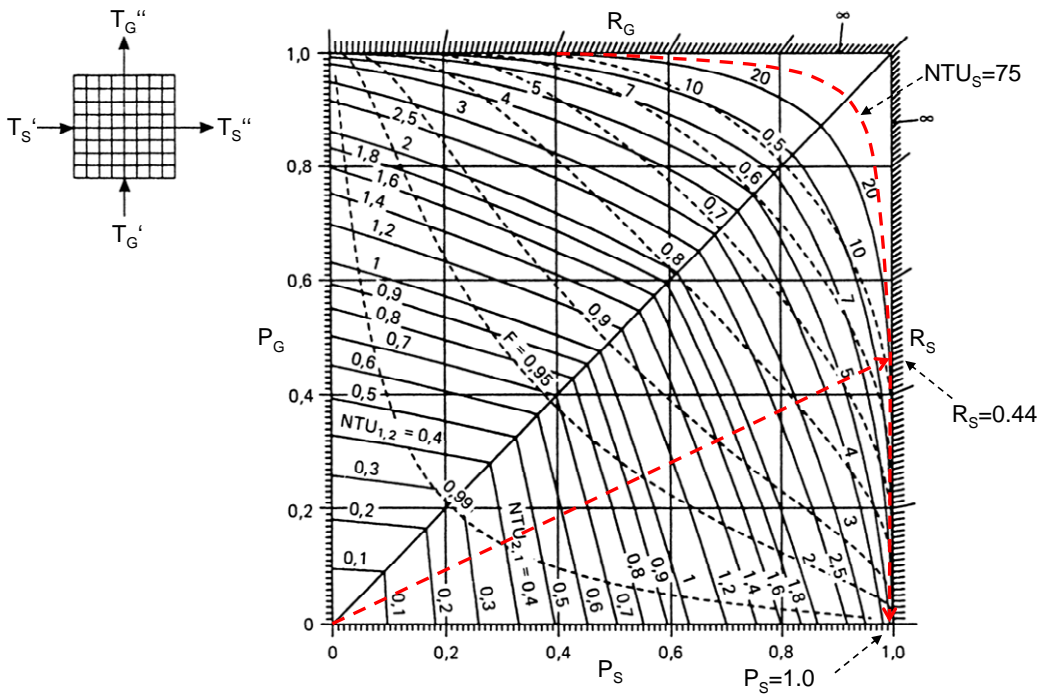


Figure 4.2 Calculation diagram of cross flow heat exchanger (VDI-Wärmetlas)

15

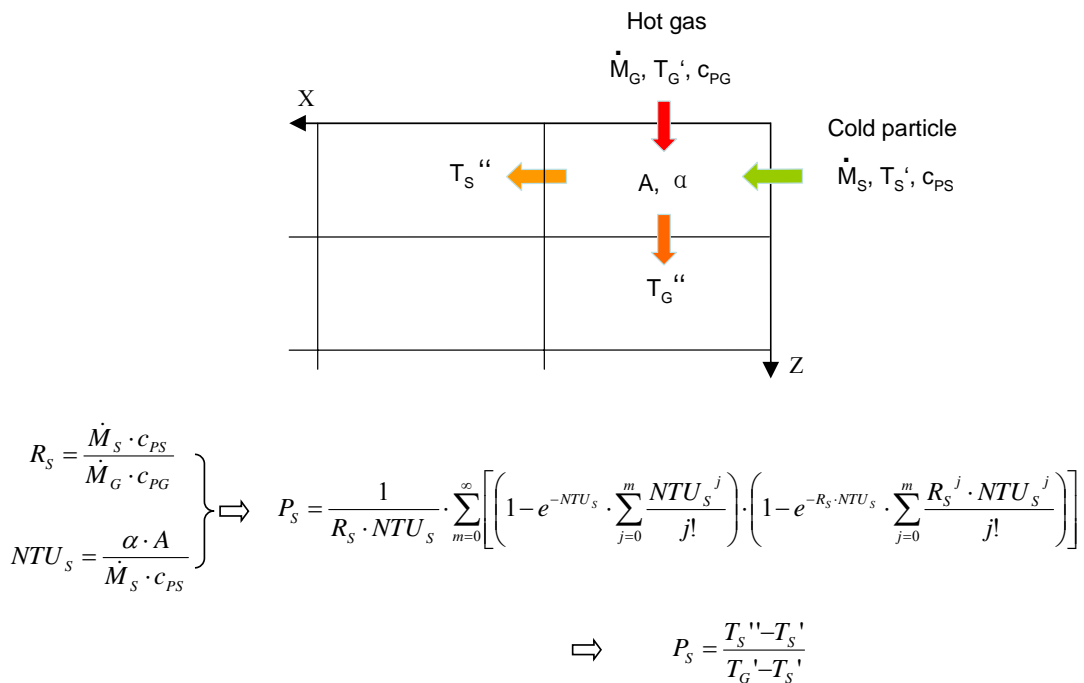


Figure 4.3 Calculation of a single cell with pure heat transfer

16

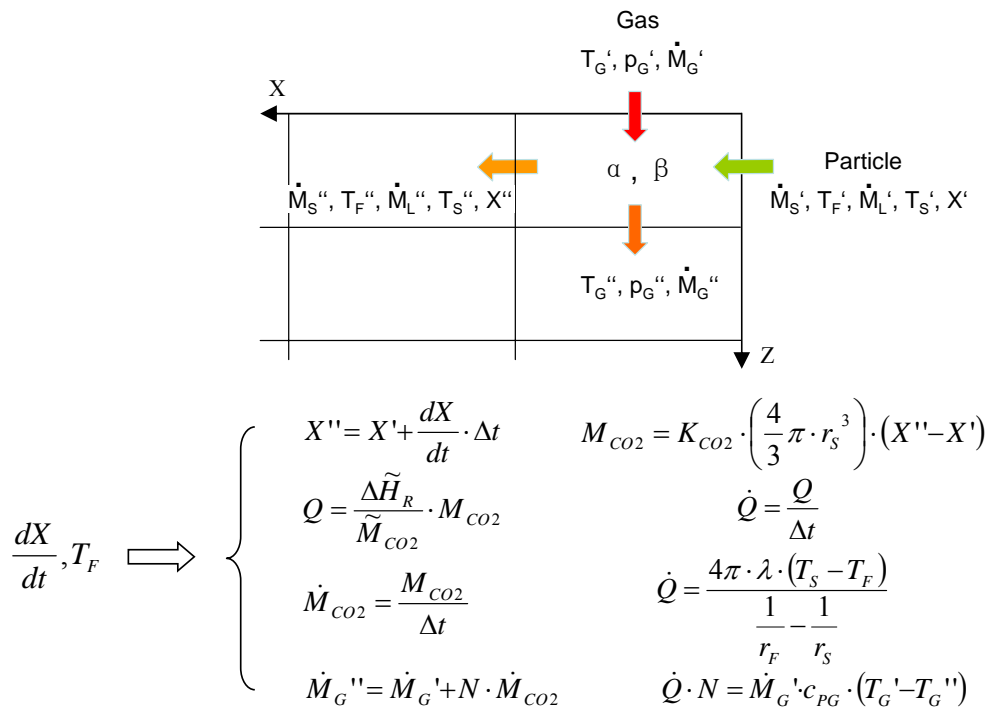


Figure 4.4 Calculation of a single cell with reaction

17

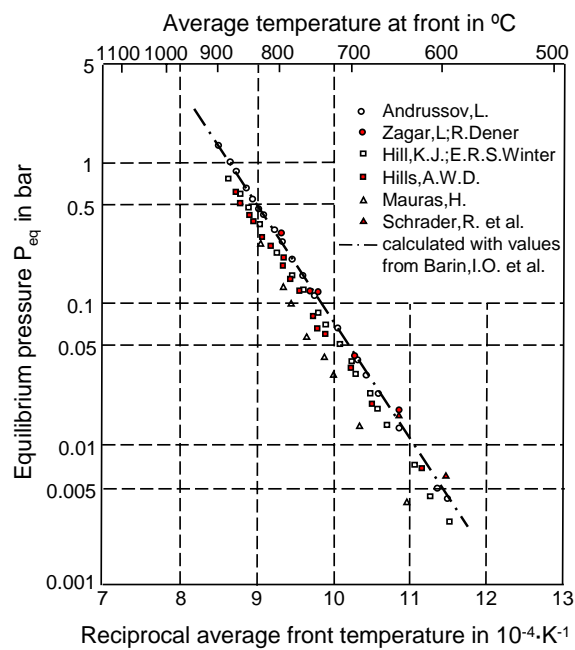


Figure 5.1 Equilibrium decomposition pressure of limestone

18

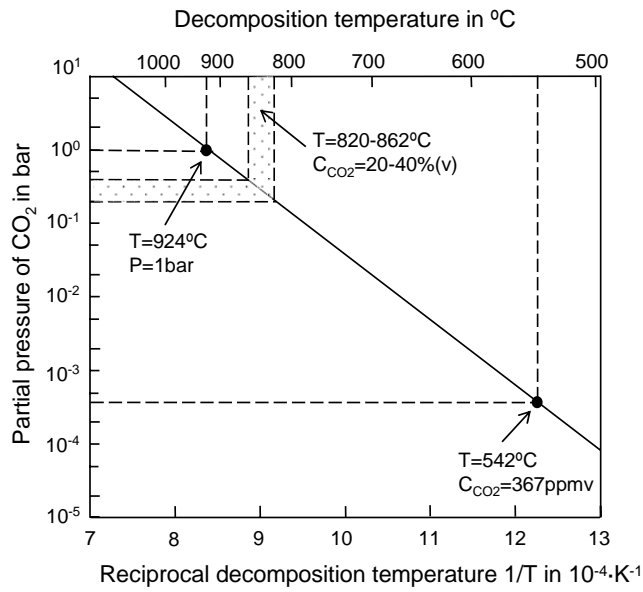


Figure 5.2 Equilibrium decomposition pressure of limestone in furnace

19

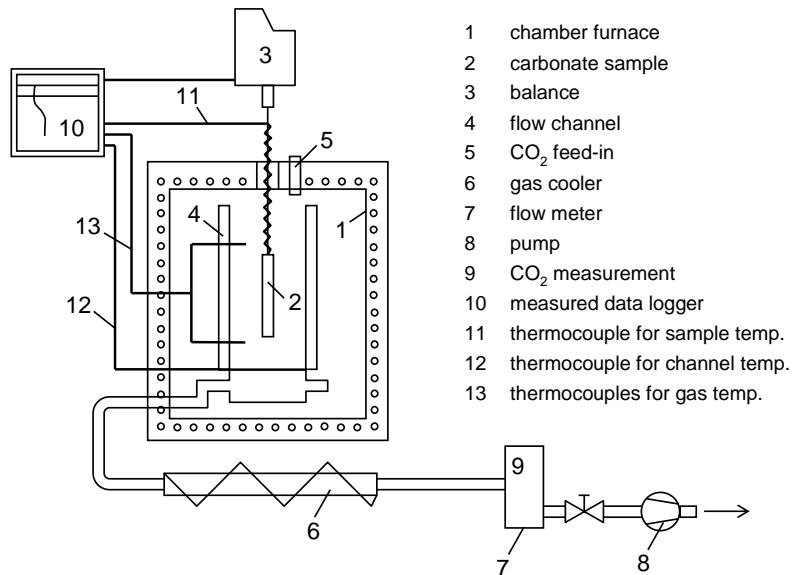


Figure 5.3 Experimental apparatus for measuring decomposition

20

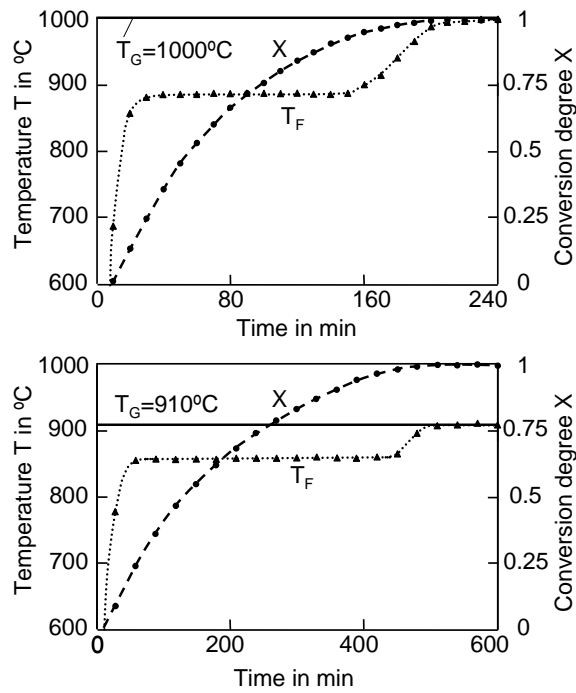


Figure 5.4 Typical conversion curves of limestone

21

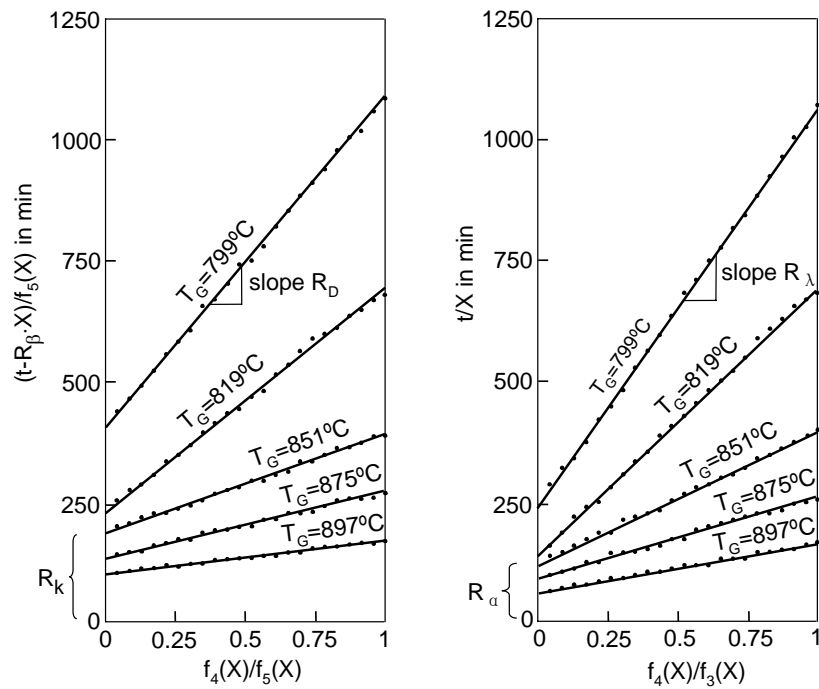


Figure 5.5 Linearized decomposition diagrams of limestone

22

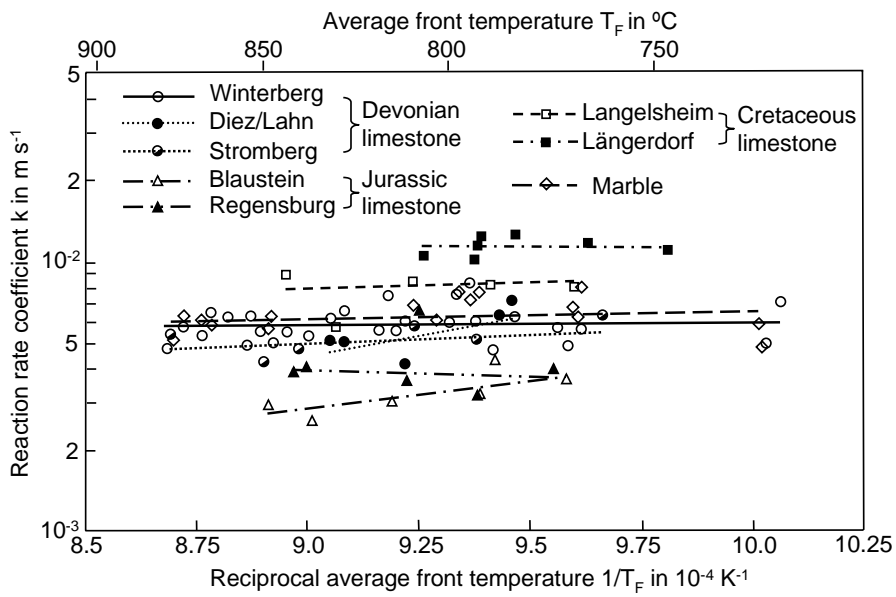


Figure 5.6 Reaction coefficient of limestone decomposition

23

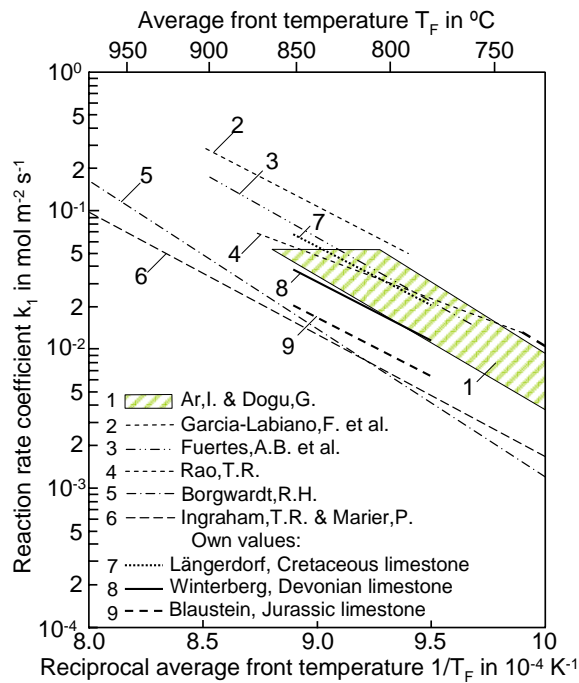


Figure 5.7 Reaction coefficient comparison of limestone decomposition

24

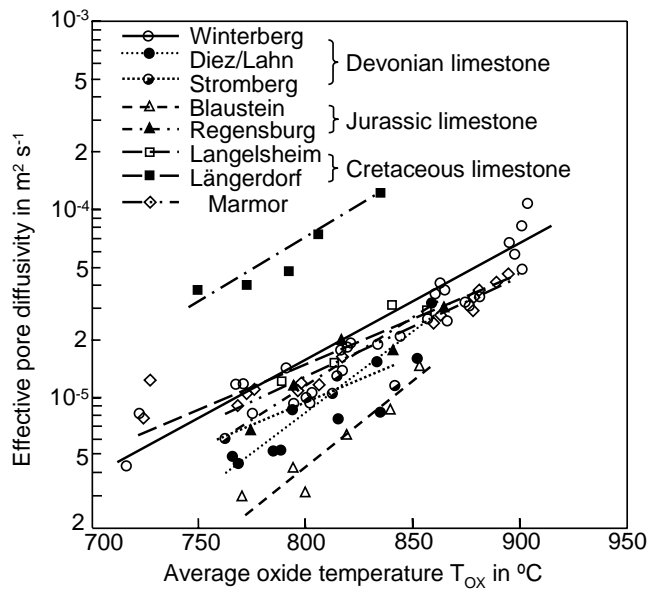


Figure 5.8 Effective pore diffusivity of limestone decomposition

25

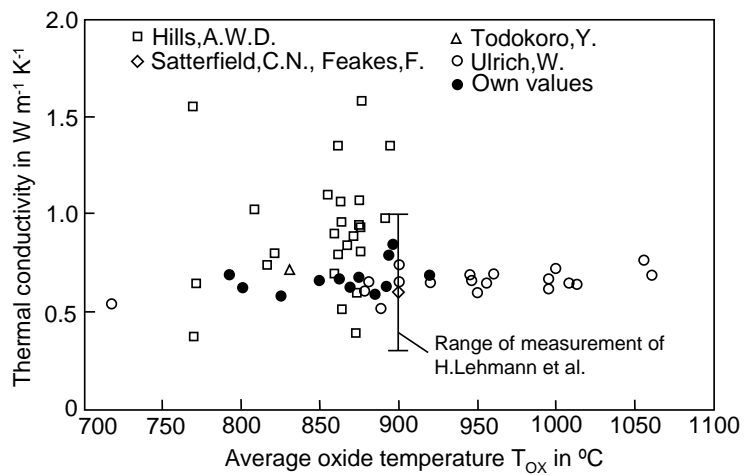


Figure 5.9 Thermal conductivity of limestone decomposition

26

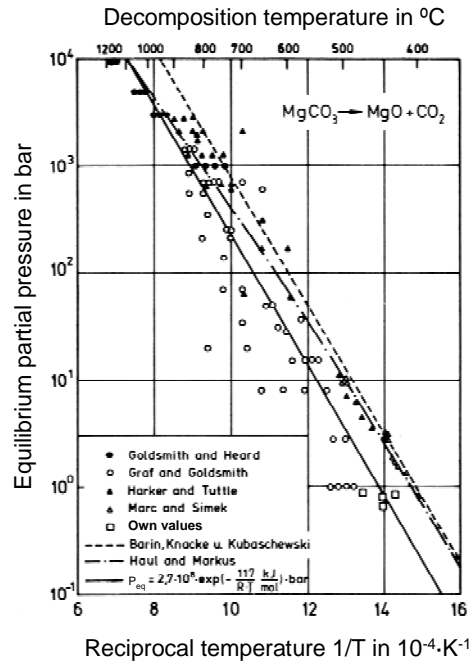


Figure 5.10 Equilibrium decomposition pressure of magnesite

27

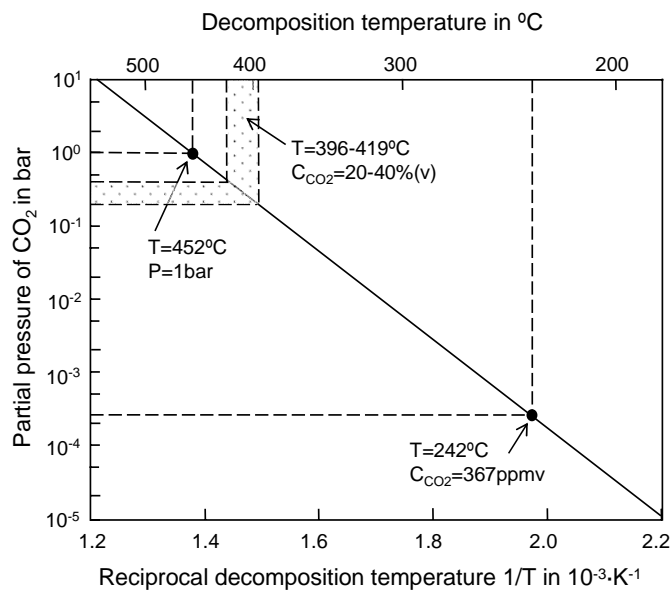


Figure 5.11 Equilibrium decomposition pressure of magnesite in furnace

28

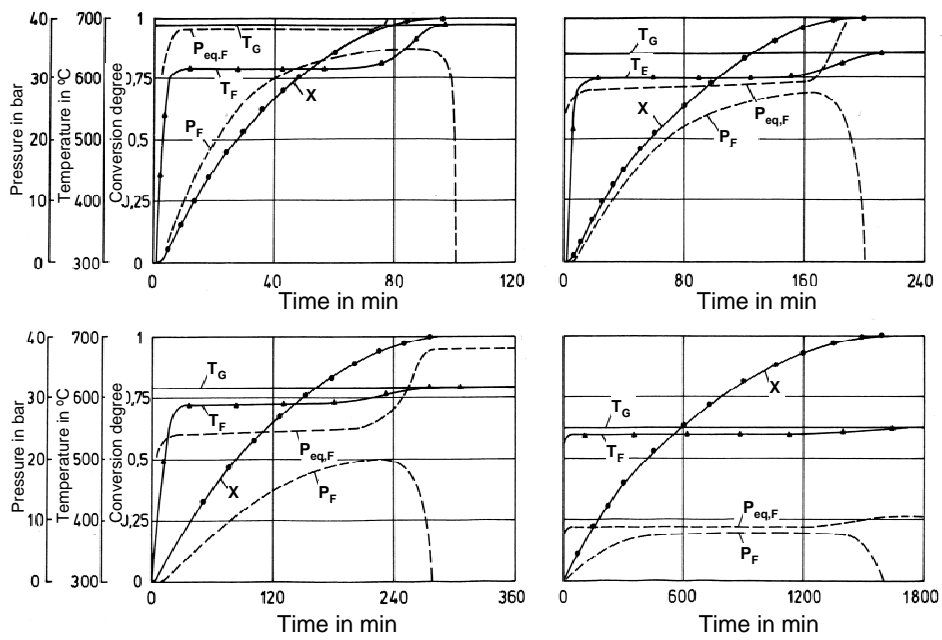


Figure 5.12 Conversion curves of magnesite decomposition

29

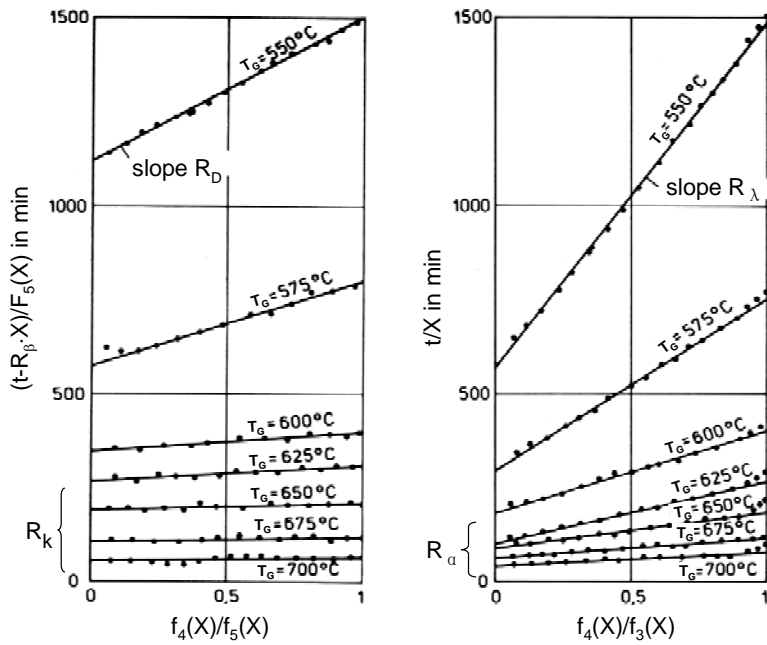


Figure 5.13 Linearized decomposition diagrams of magnesite

30

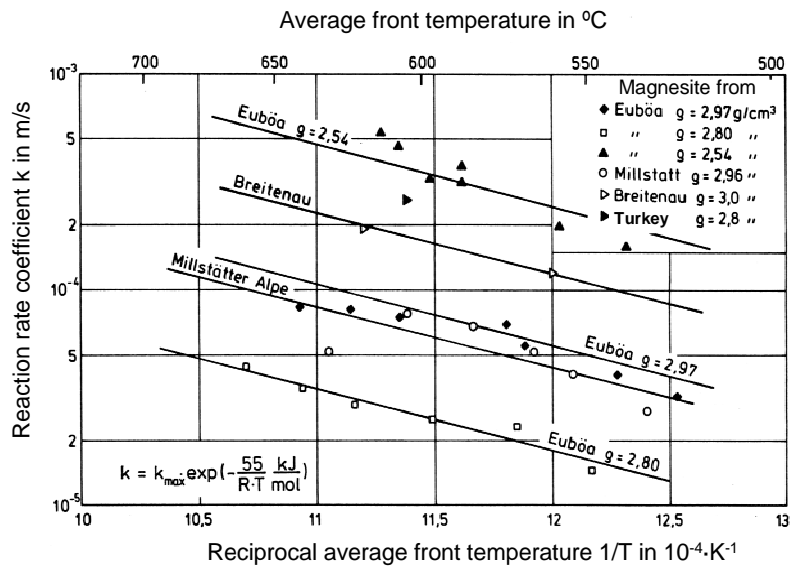


Figure 5.14 Reaction coefficients of magnesite decomposition

31

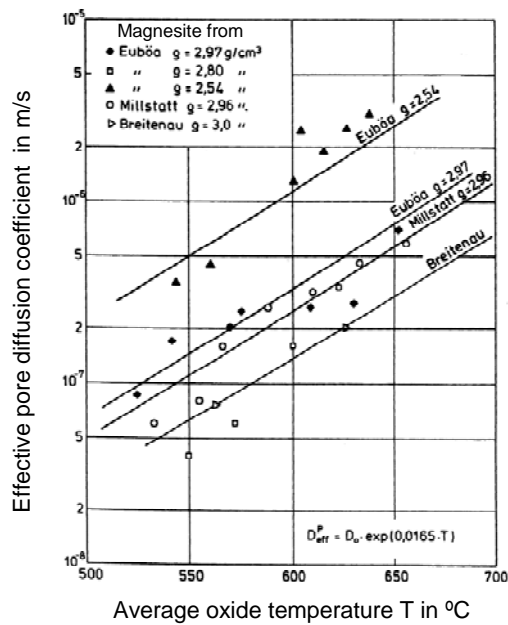


Figure 5.15 Effective pore diffusivity of magnesite decomposition

32

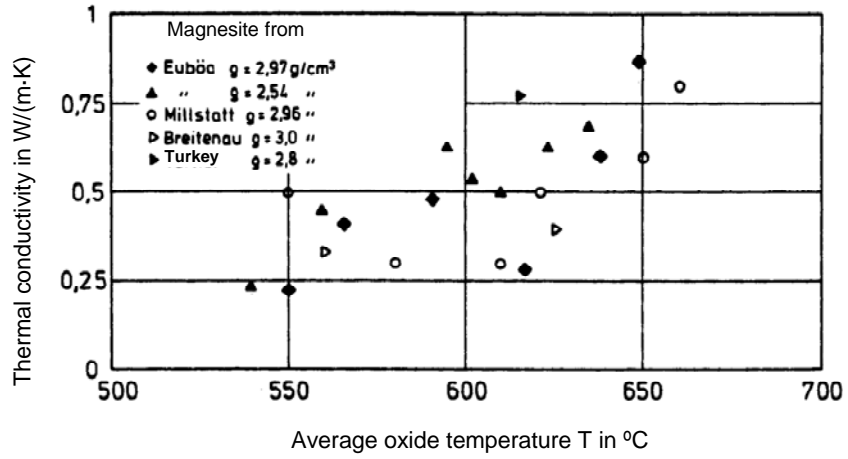


Figure 5.16 Thermal conductivity of magnesite decomposition

33

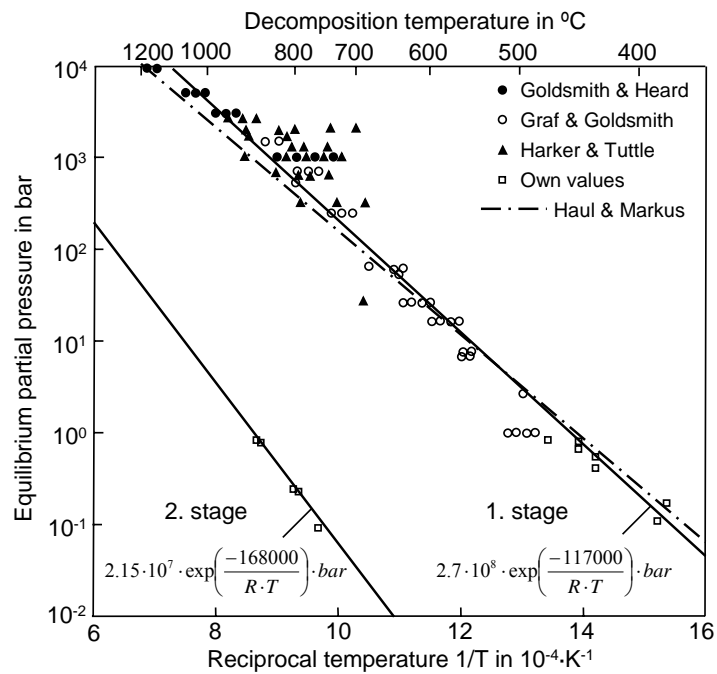


Figure 5.17 Equilibrium decomposition pressure of dolomite

34

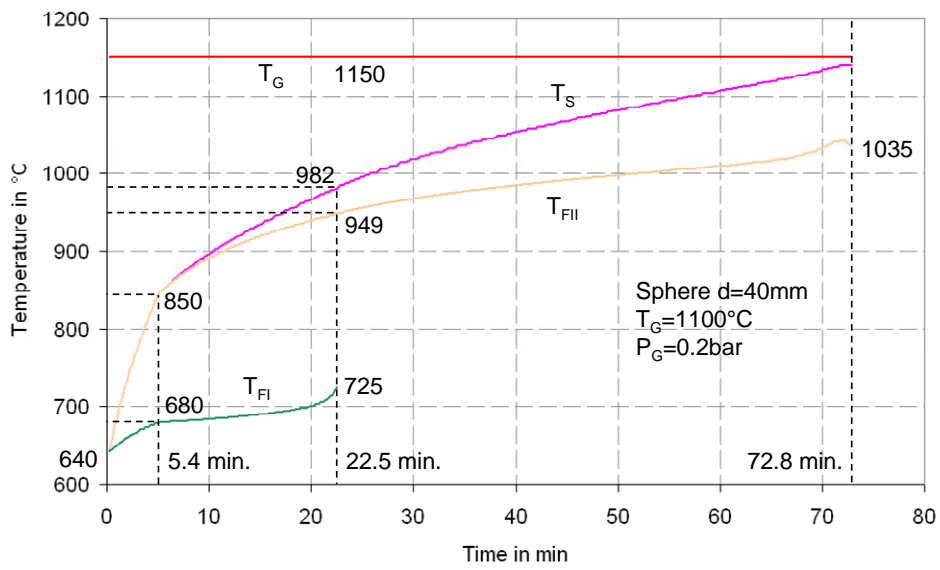


Figure 5.18 Calculated temperature curves in simultaneous decomposition of dolomite

35

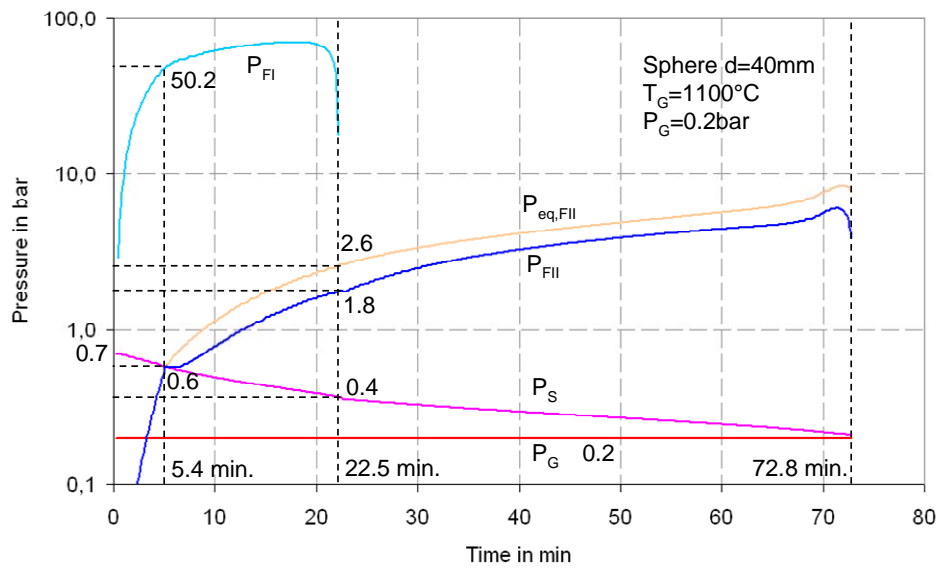


Figure 5.19 Calculated pressure curves in simultaneous decomposition of dolomite

36

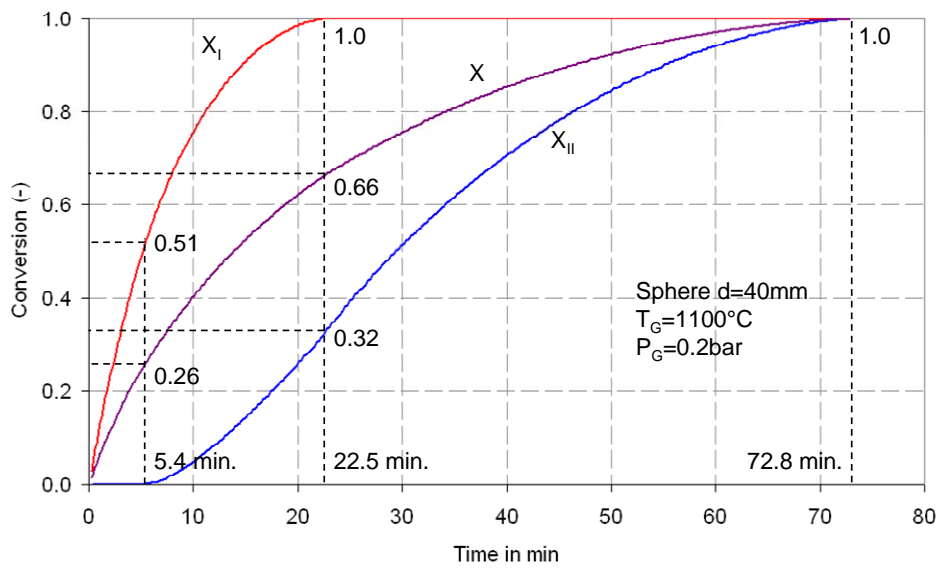


Figure 5.20 Calculated conversion curves in simultaneous decomposition of dolomite

37

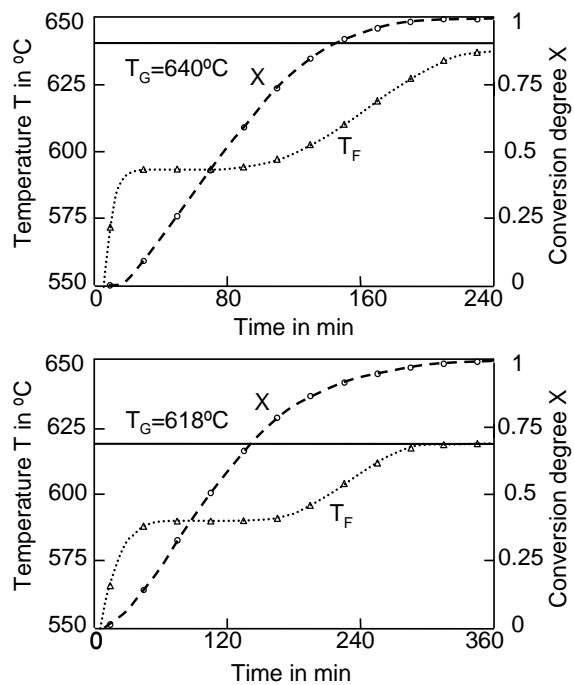


Figure 5.21 Conversion curves of dolomite decomposition (1. stage)

38

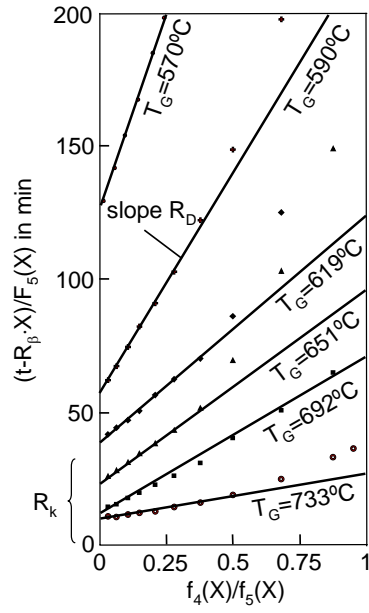


Figure 5.22 Linearized decomposition diagrams of dolomite (1. stage)

39

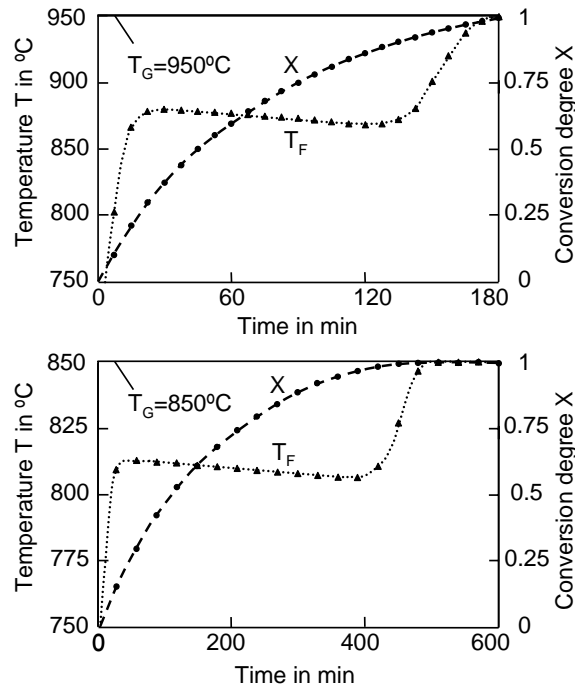


Figure 5.23 Conversion curves of dolomite decomposition (2. stage)

40

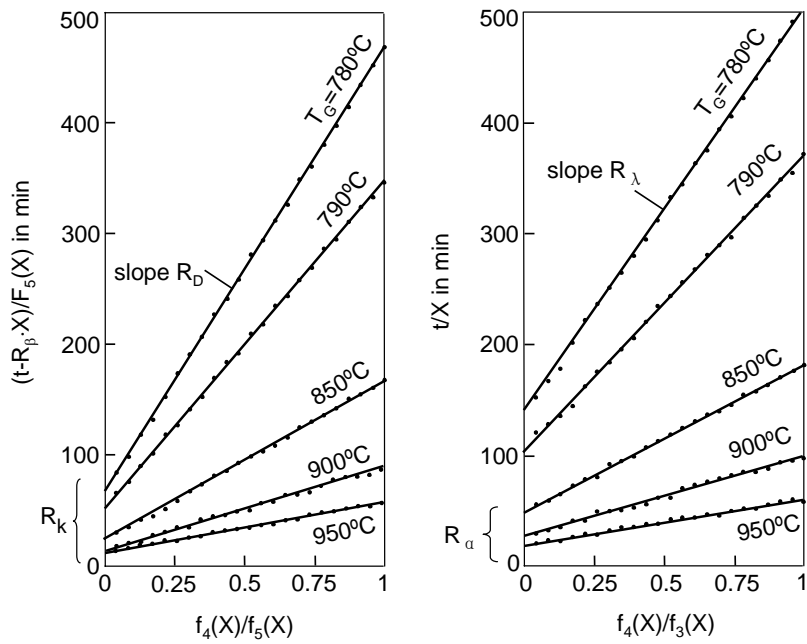


Figure 5.24 Linearized decomposition diagrams of dolomite (2. stage)

41

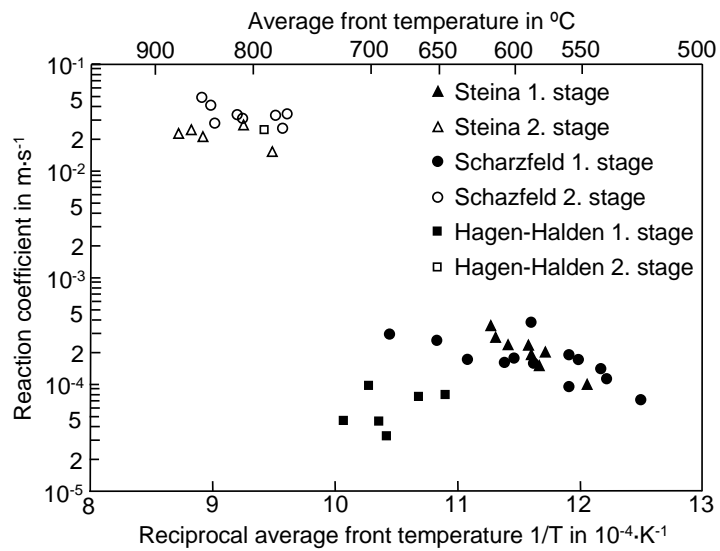


Figure 5.25 Reaction coefficient of dolomite decomposition

42

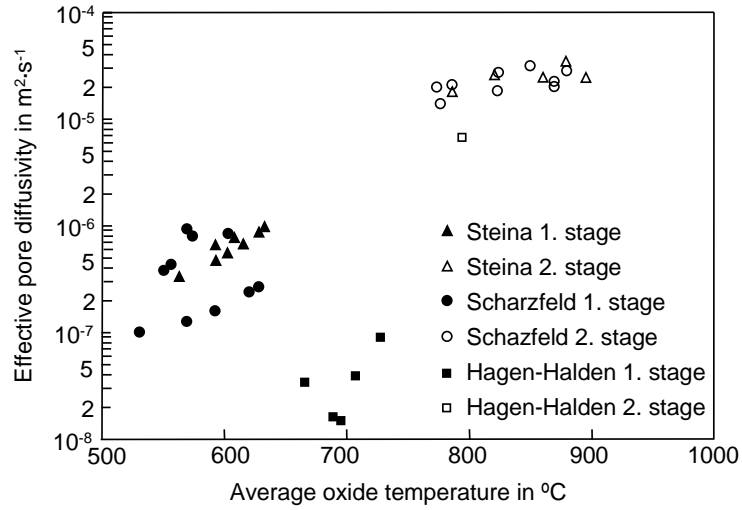


Figure 5.26 Effective pore diffusivity of dolomite decomposition

43

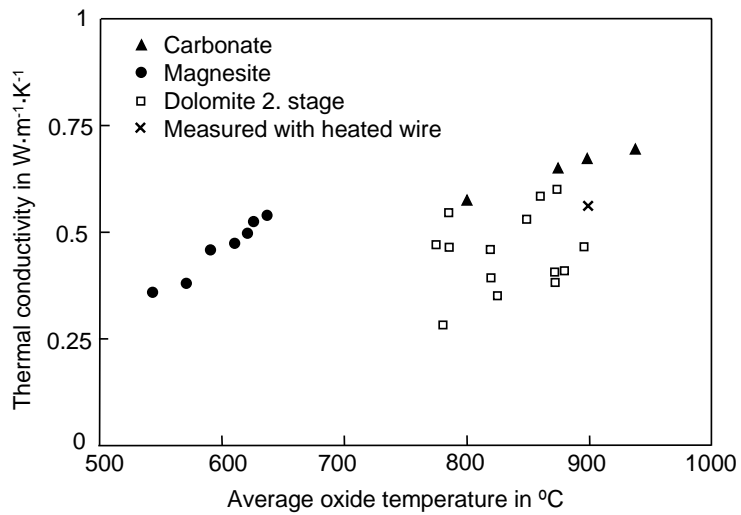


Figure 5.27 Thermal conductivity of dolomite decomposition

44

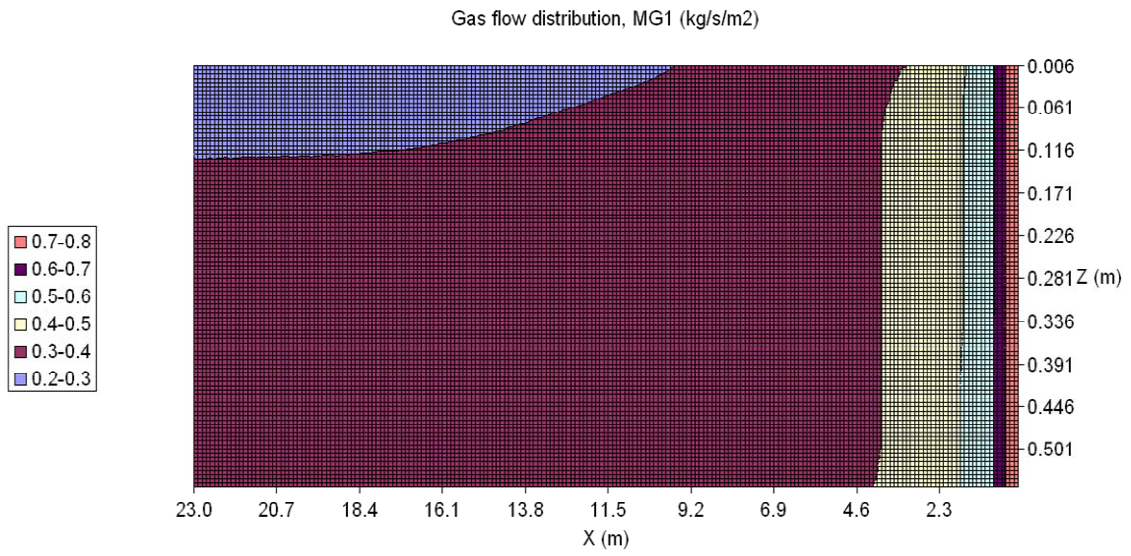


Figure 6.1 LEPOL-case 0: Gas flux distribution

45

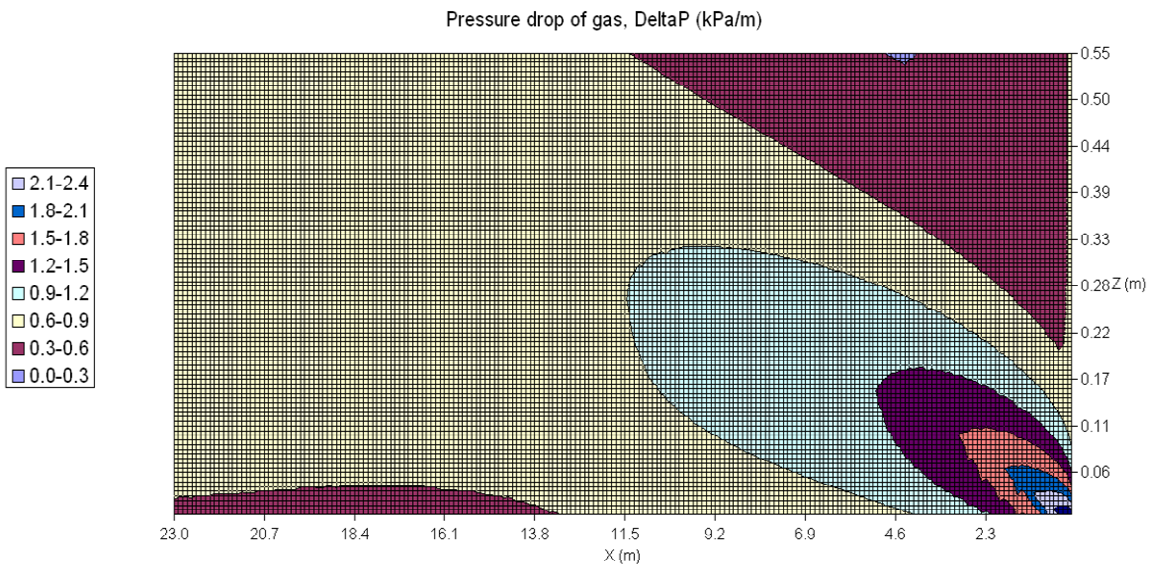


Figure 6.2 LEPOL-case 0: Pressure drop distribution

46

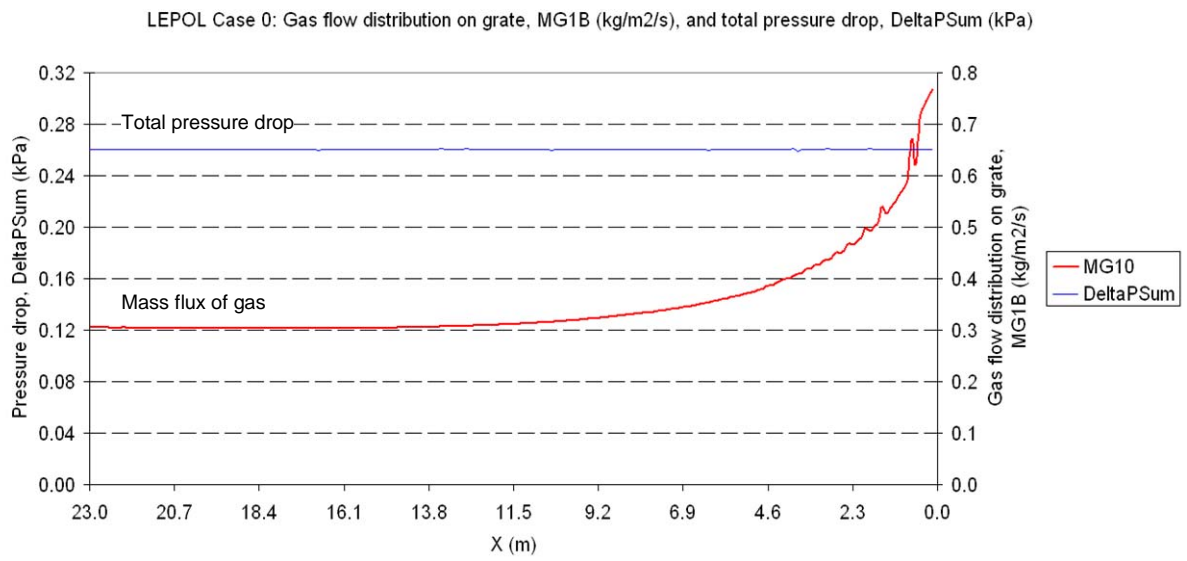


Figure 6.3 LEPOL-case 0: Total pressure drop

47

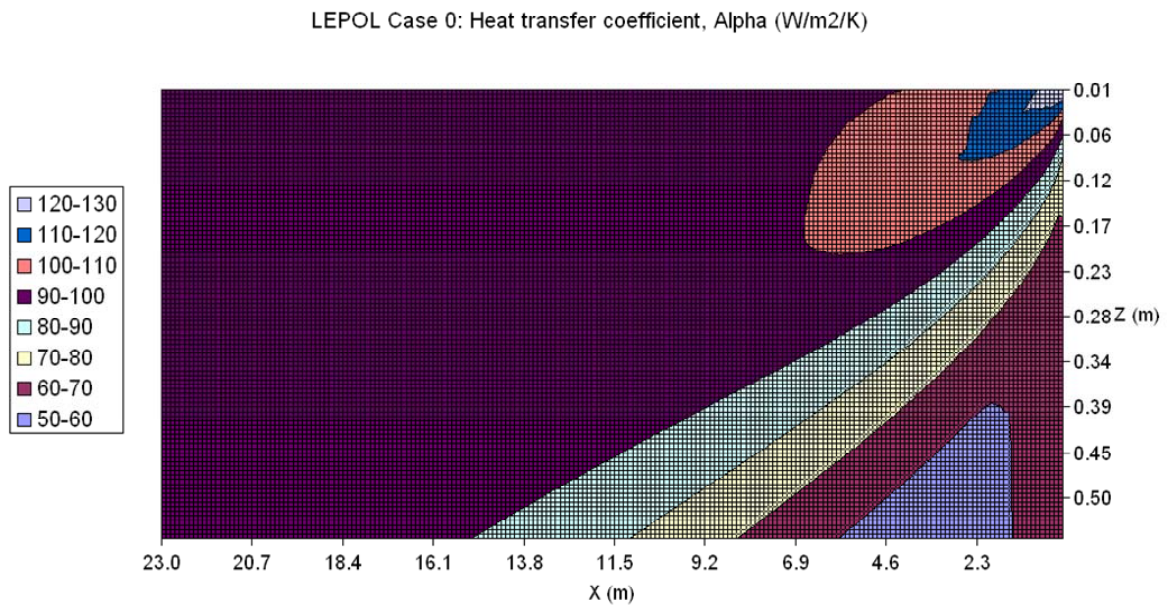


Figure 6.4 LEPOL-case 0: Heat transfer coefficient

48

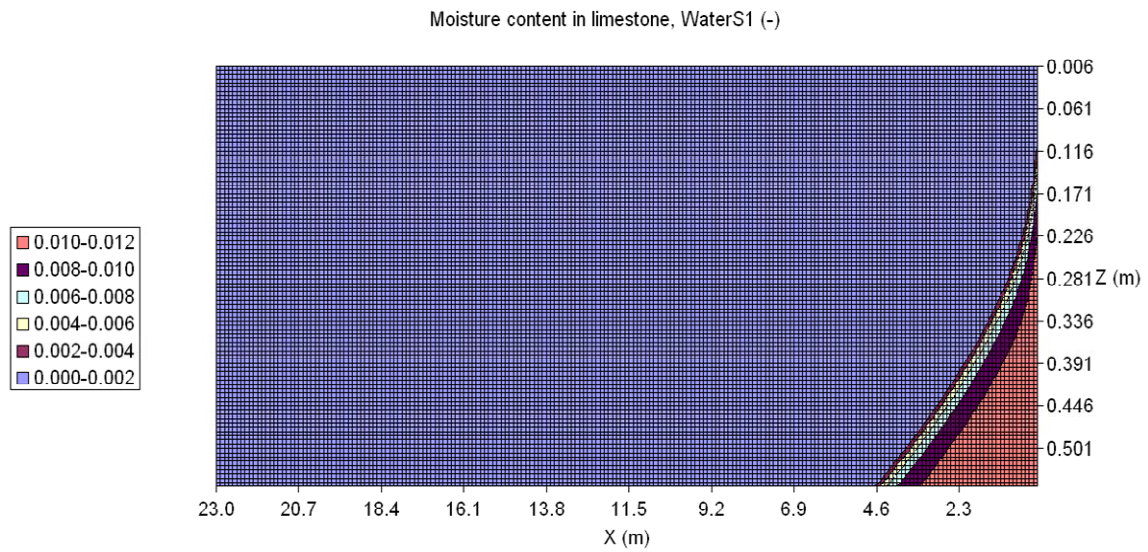


Figure 6.5 LEPOL-case 0: Moisture content

49

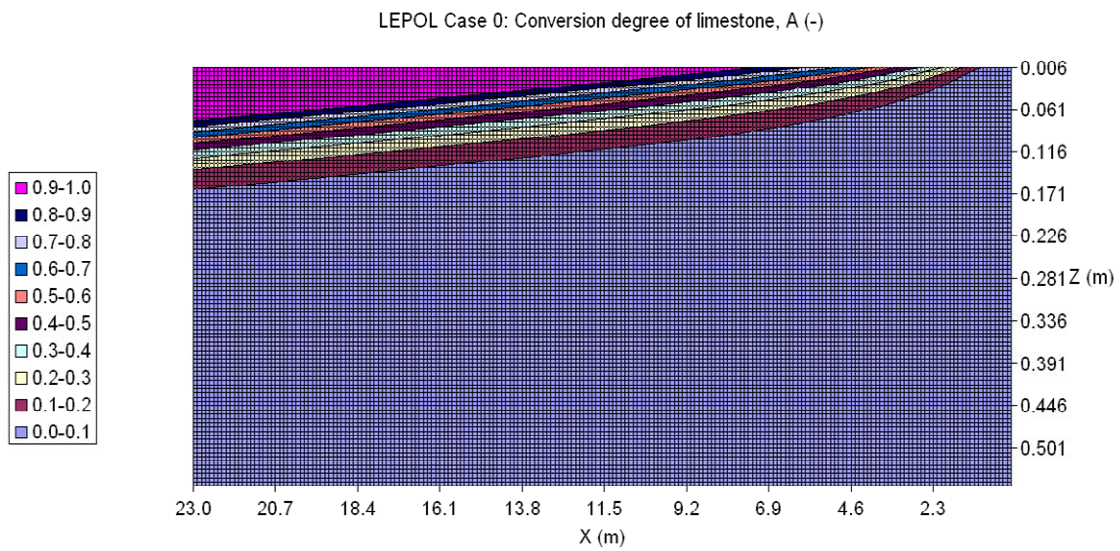


Figure 6.6 LEPOL-case 0: Conversion degree

50

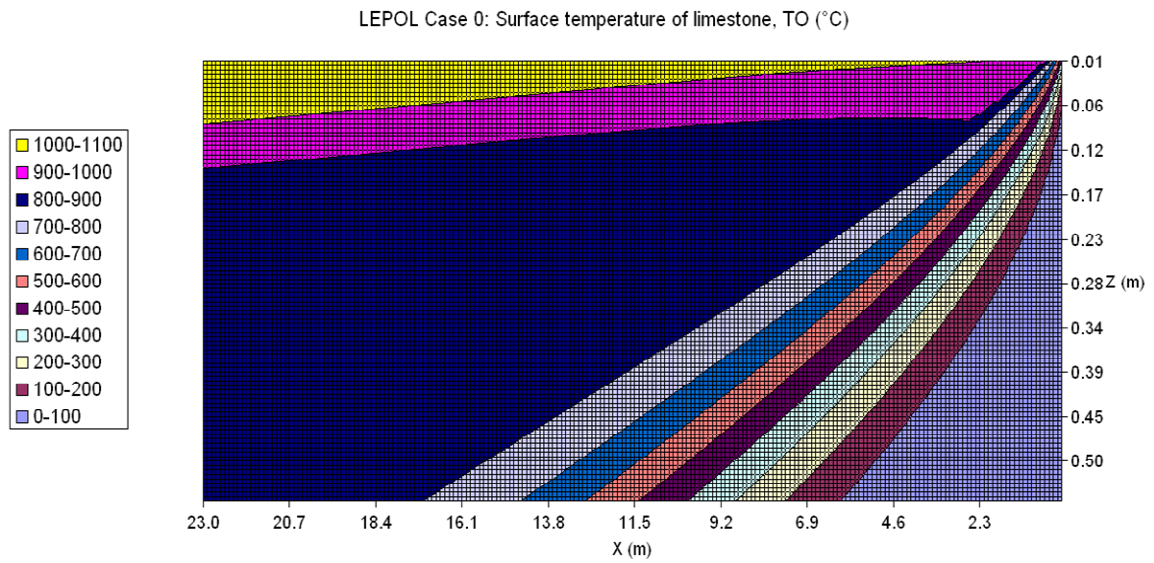


Figure 6.7 LEPOL-case 0: Particle surface temperature

51

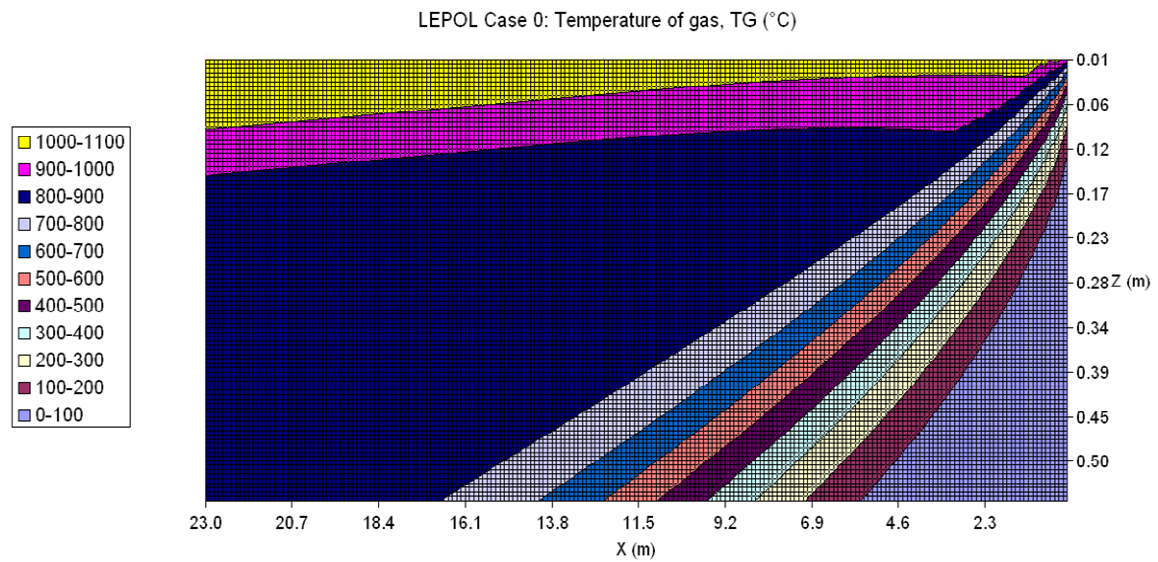


Figure 6.8 LEPOL-case 0: Gas temperature

52

LEPOL Case 0: Gas temperature at input, TGI (°C) and on grate, TGB (°C)

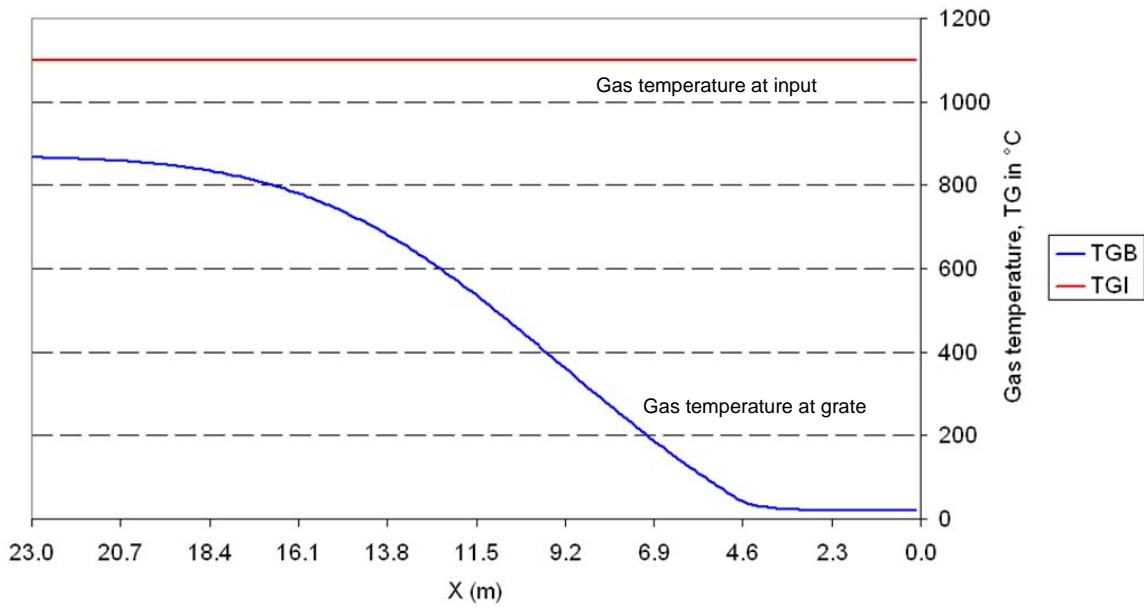


Figure 6.9 LEPOL-case 0: Gas exiting temperature

53

Gas temperature on grate, TG vs Grate length, L (m)

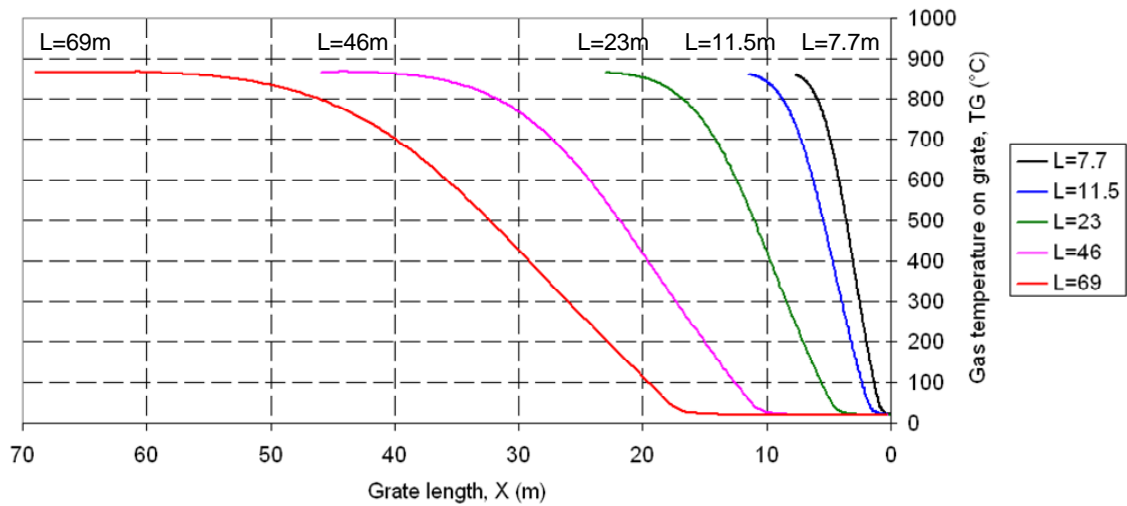


Figure 6.10 Influence of grate length on gas temperature

54

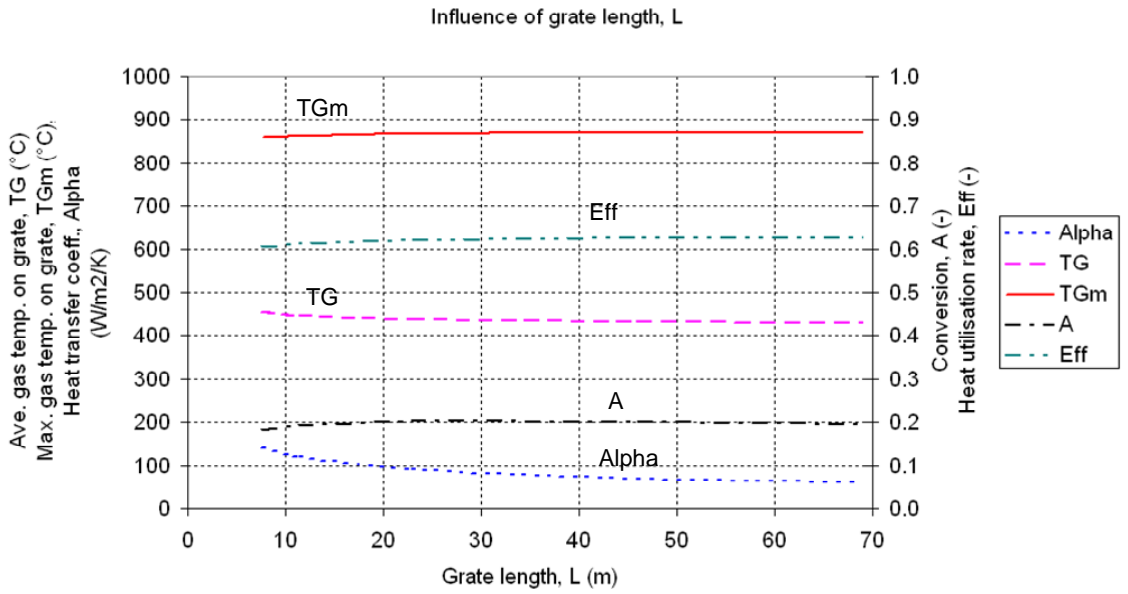


Figure 6.11 Influence of grate length

55

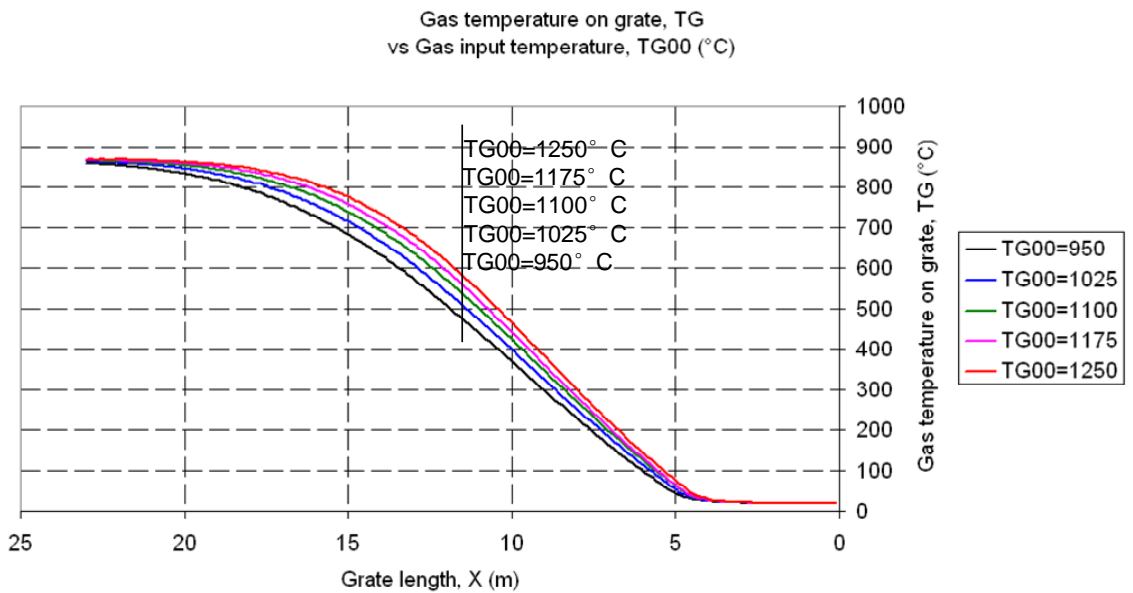


Figure 6.12 Influence of gas input temperature on gas temperature

56

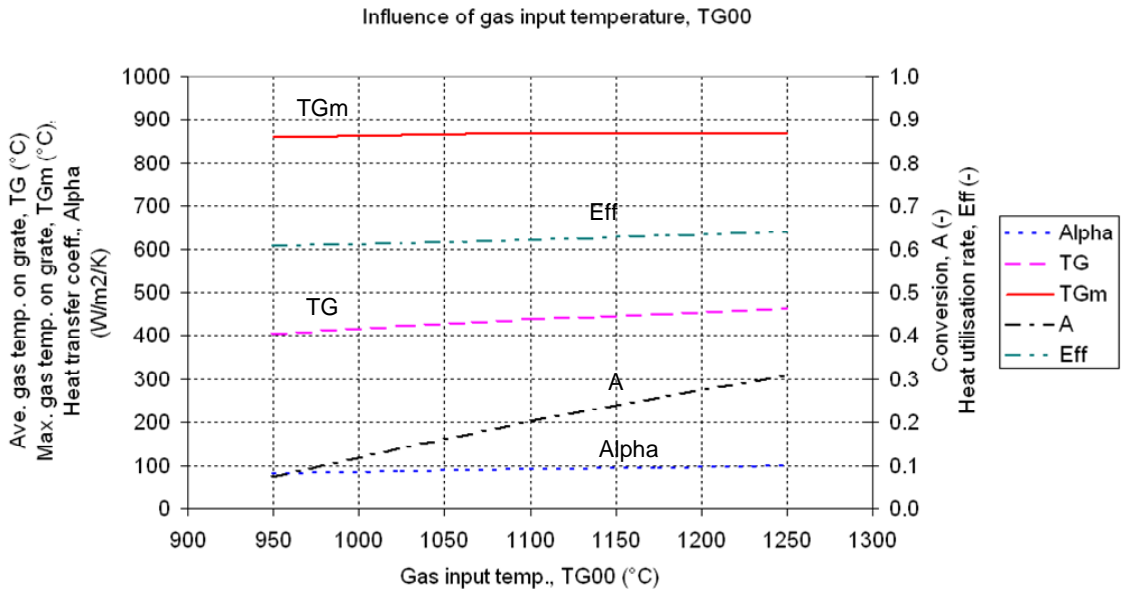


Figure 6.13 Influence of gas input temperature

57

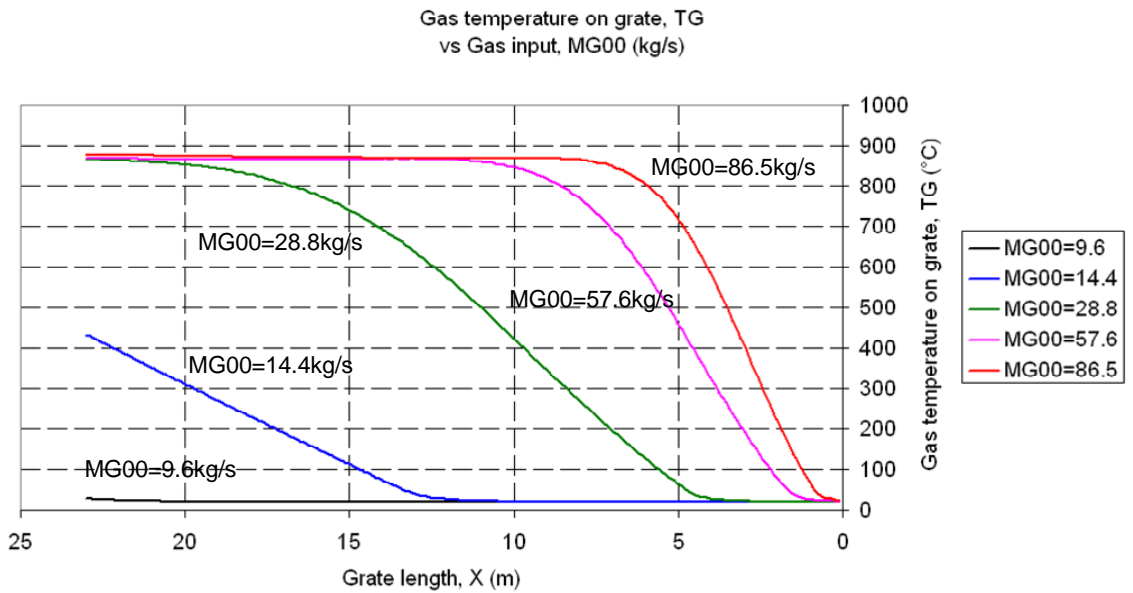


Figure 6.14 Influence of gas amount on gas temperature

58

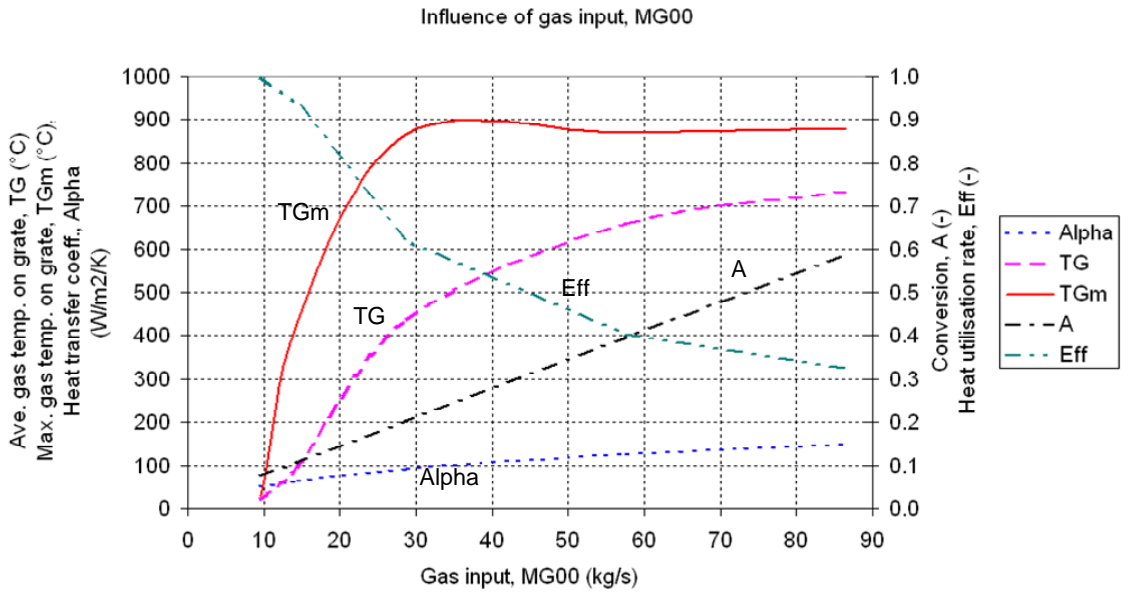


Figure 6.15 Influence of gas amount

59

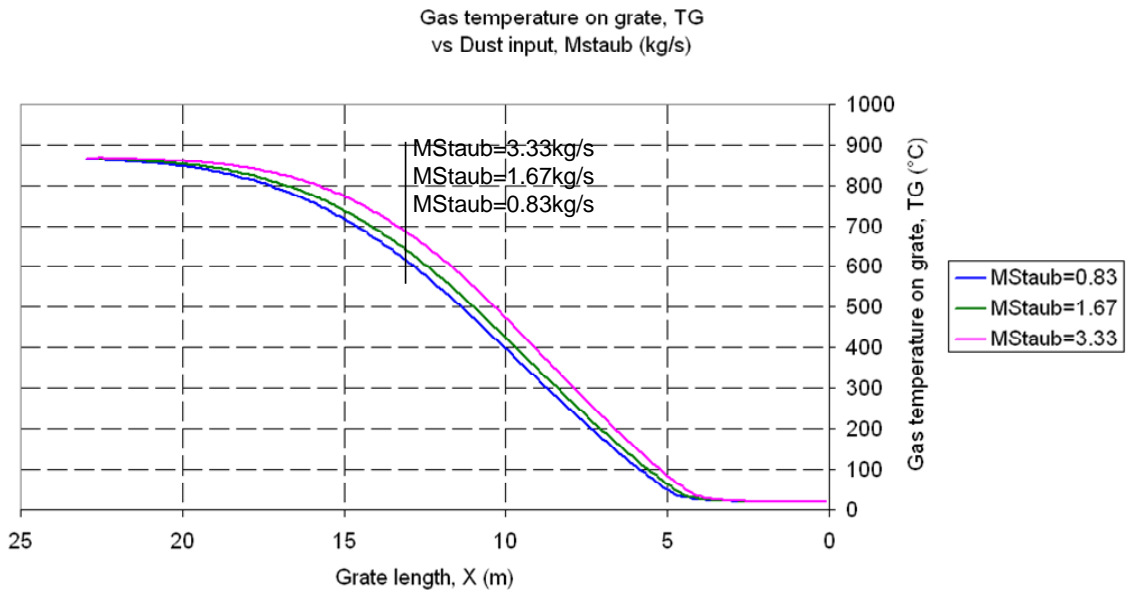


Figure 6.16 Influence of dust amount on gas temperature

60

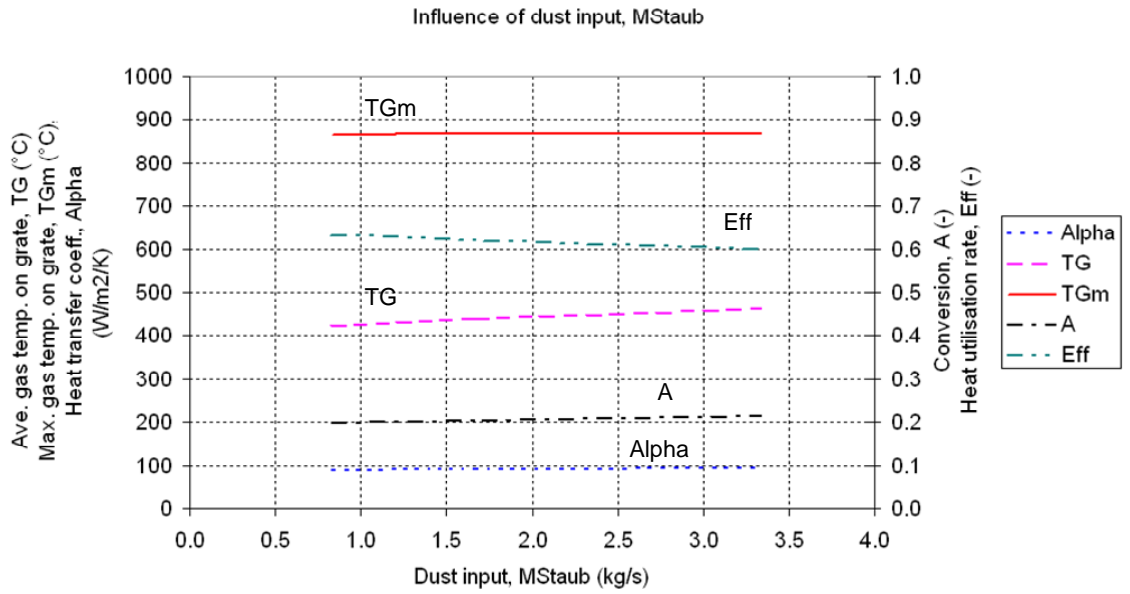


Figure 6.17 Influence of dust amount

61

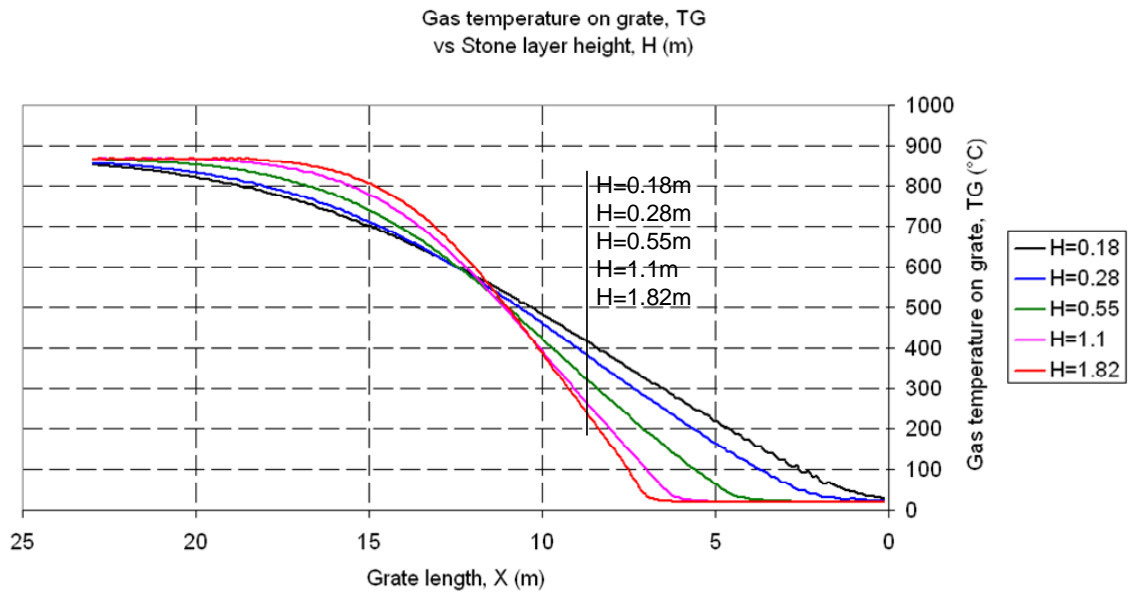


Figure 6.18 Influence of stone layer height on gas temperature

62

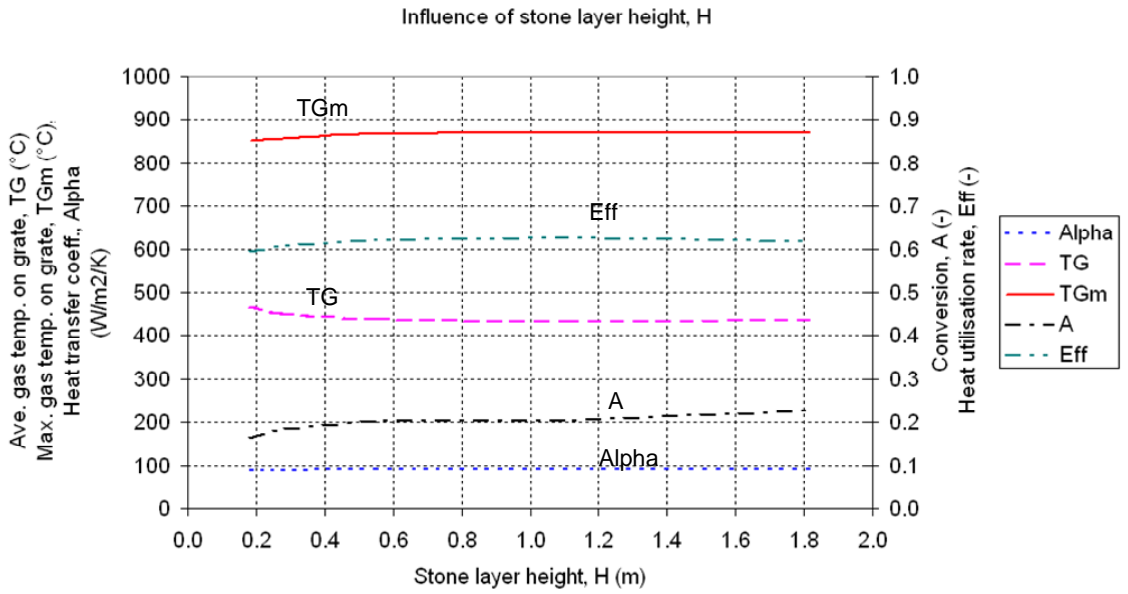


Figure 6.19 Influence of stone layer height

63

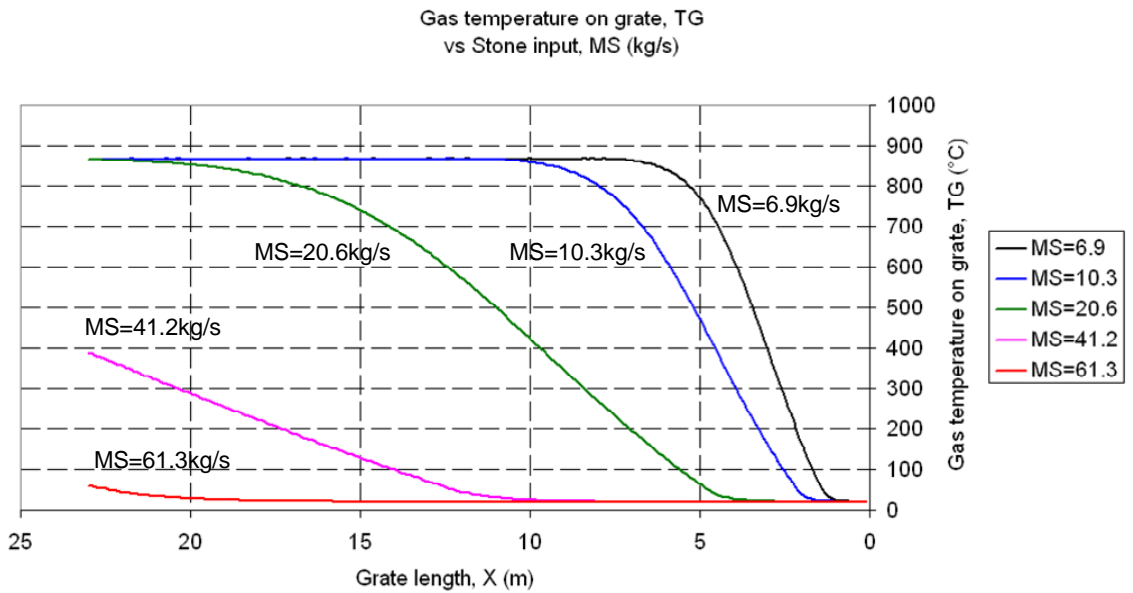


Figure 6.20 Influence of limestone amount on gas temperature

64

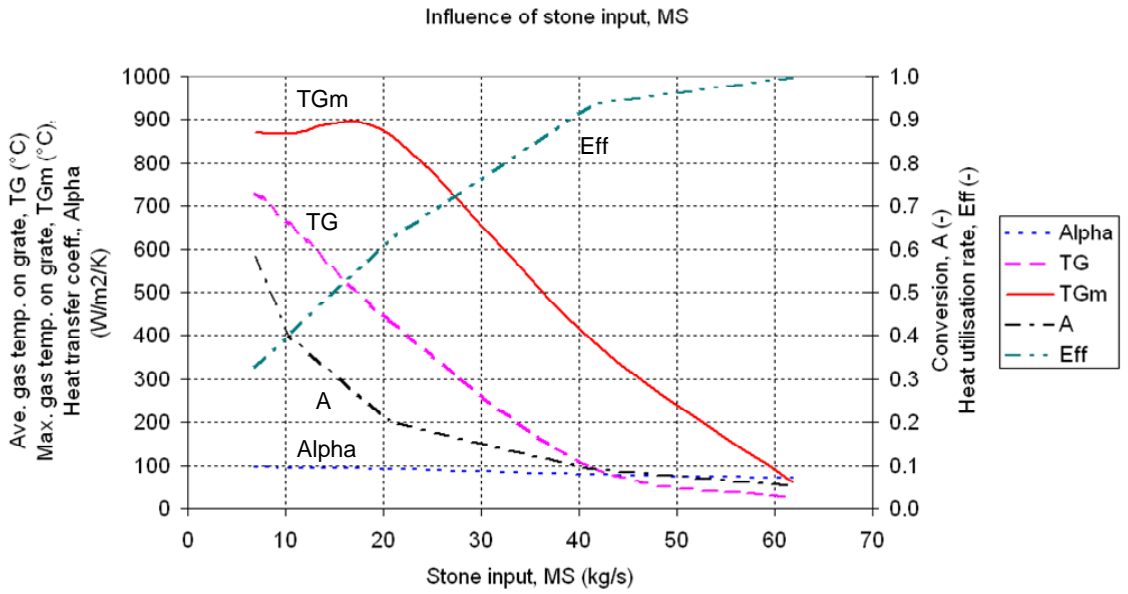


Figure 6.21 Influence of limestone amount

65

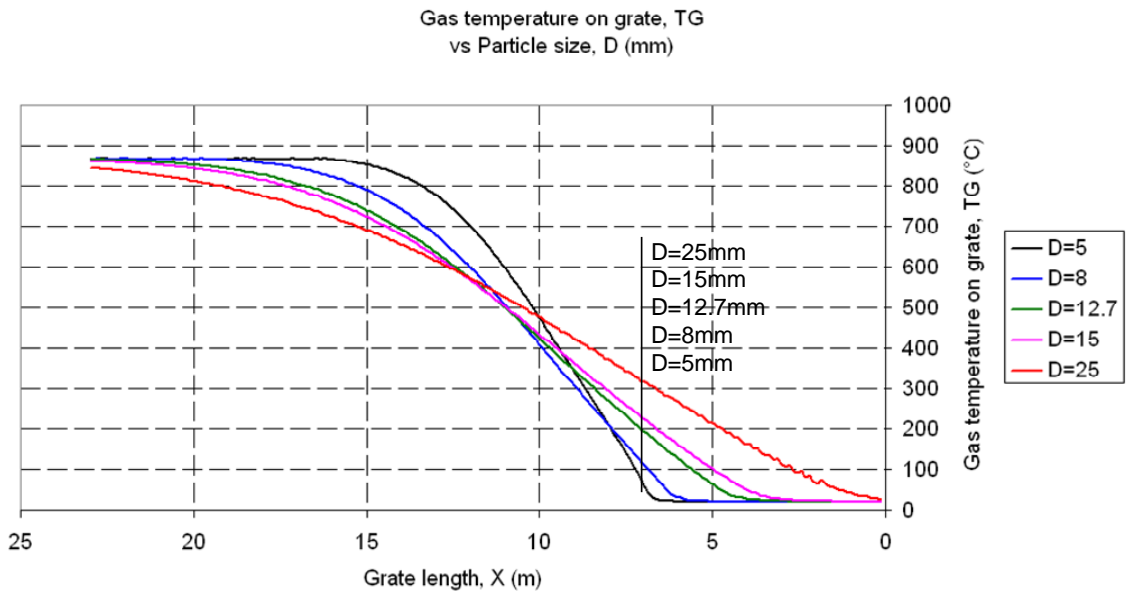


Figure 6.22 Influence of particle size on gas temperature

66

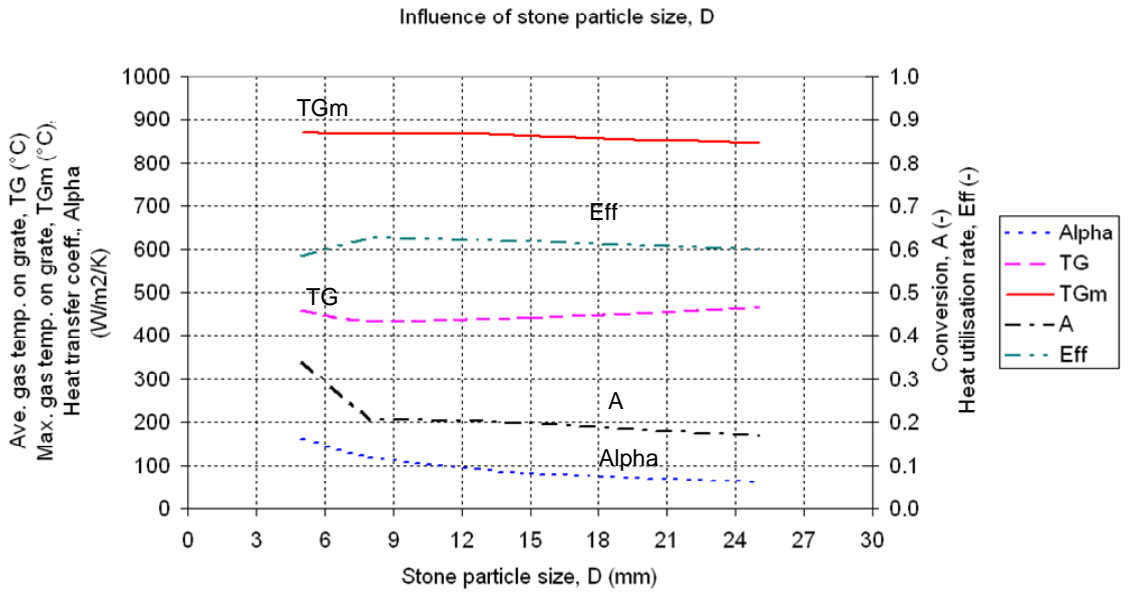


Figure 6.23 Influence of particle size on gas temperature

67

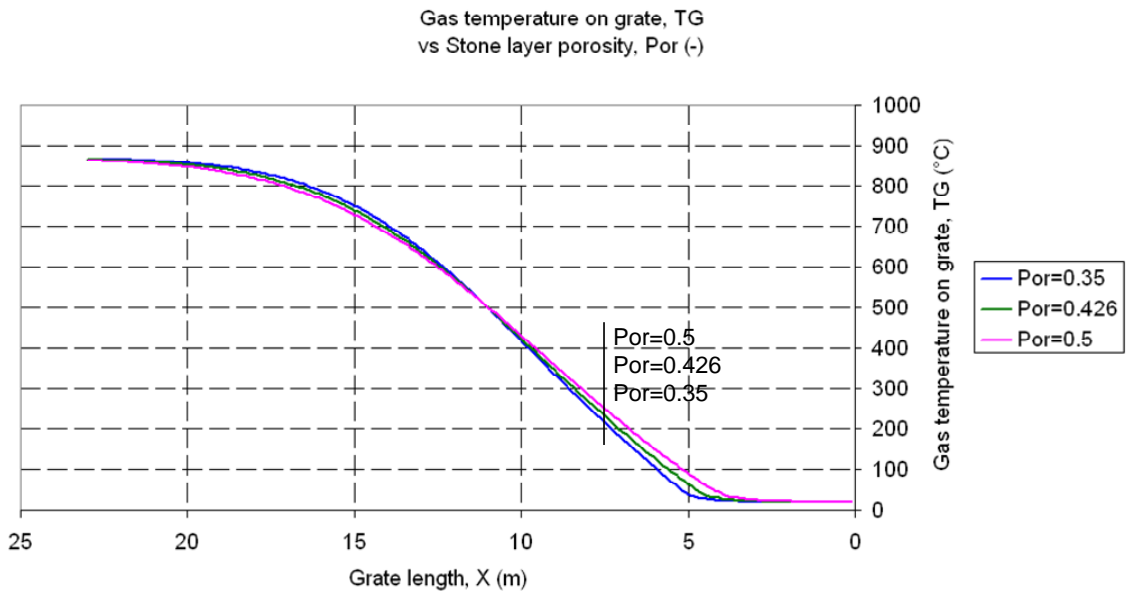


Figure 6.24 Influence of porosity on gas temperature

68

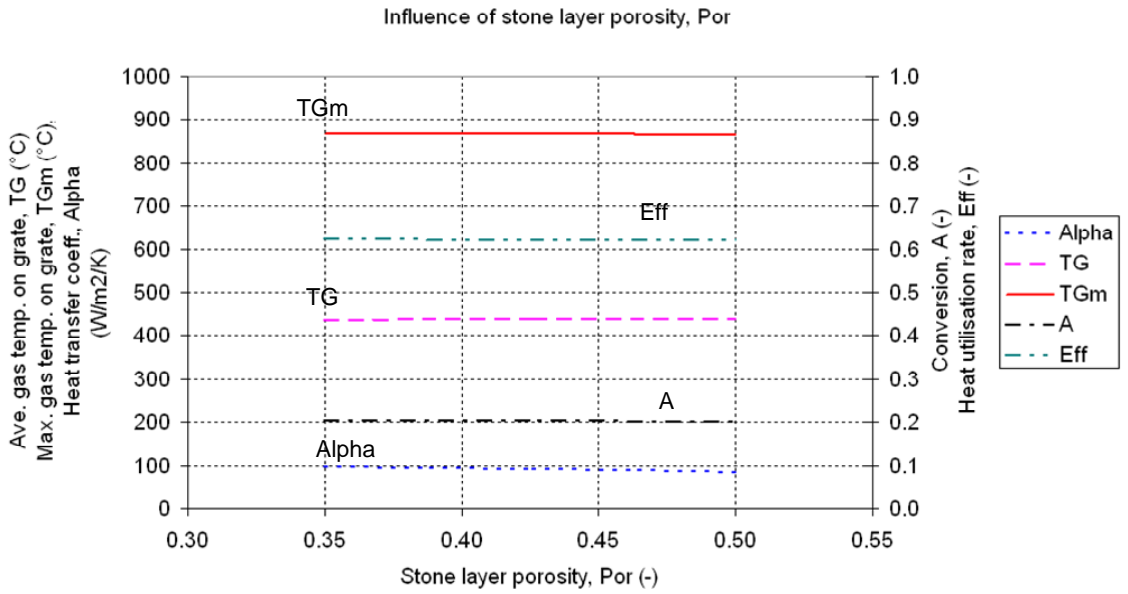


Figure 6.25 Influence of porosity

69

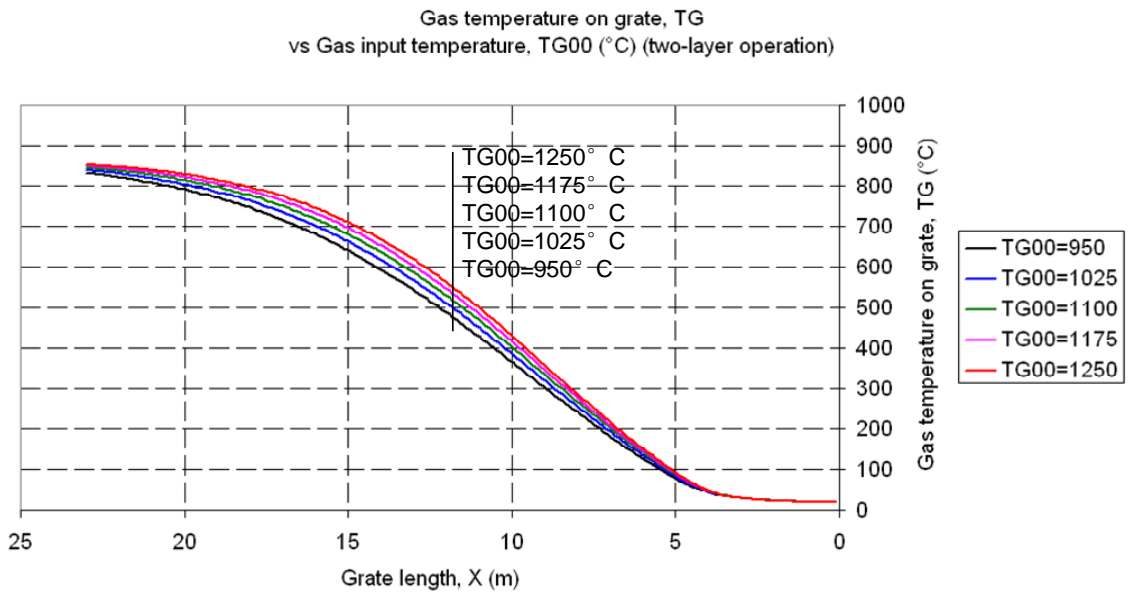


Figure 6.26 Influence of gas input temperature on gas temperature (two-layer)

70

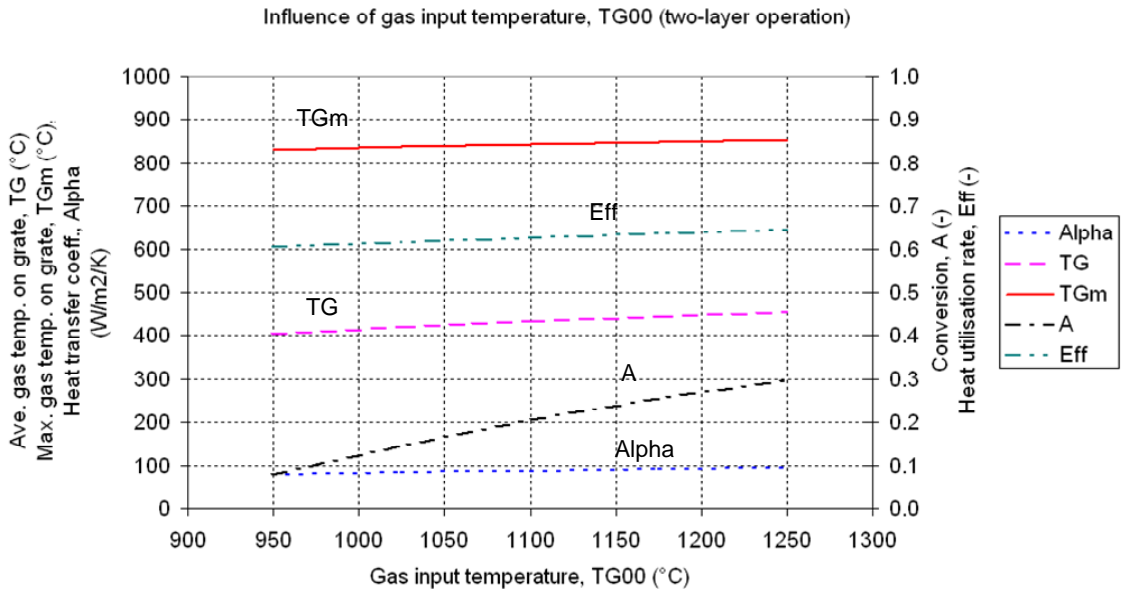


Figure 6.27 Influence of gas input temperature (two-layer)

71

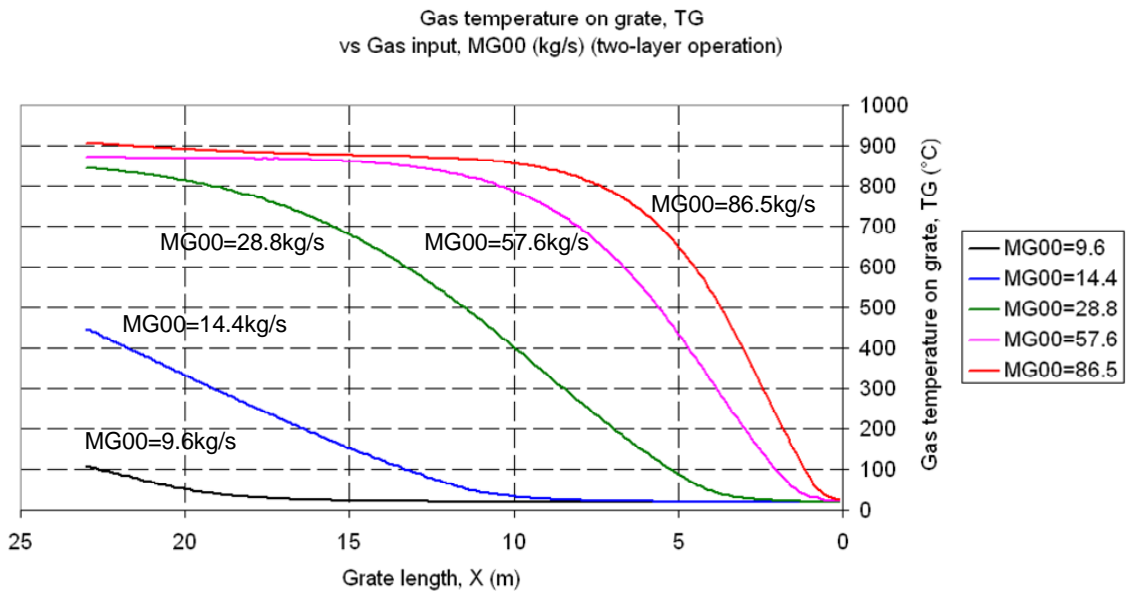


Figure 6.28 Influence of gas amount on gas temperature (two-layer)

72

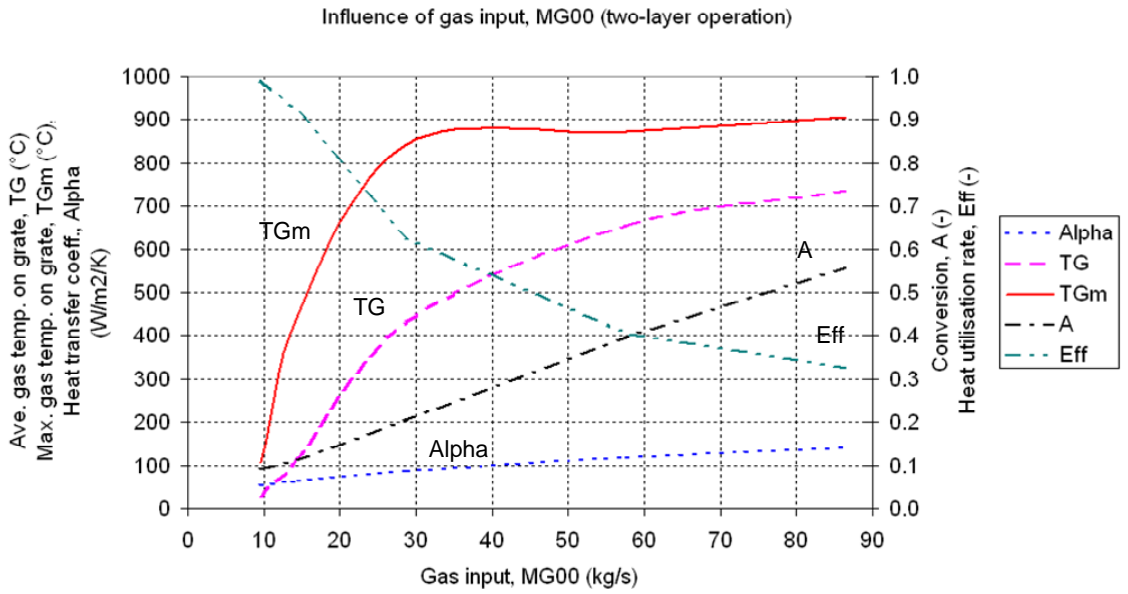


Figure 6.29 Influence of gas input temperature (two-layer)

73

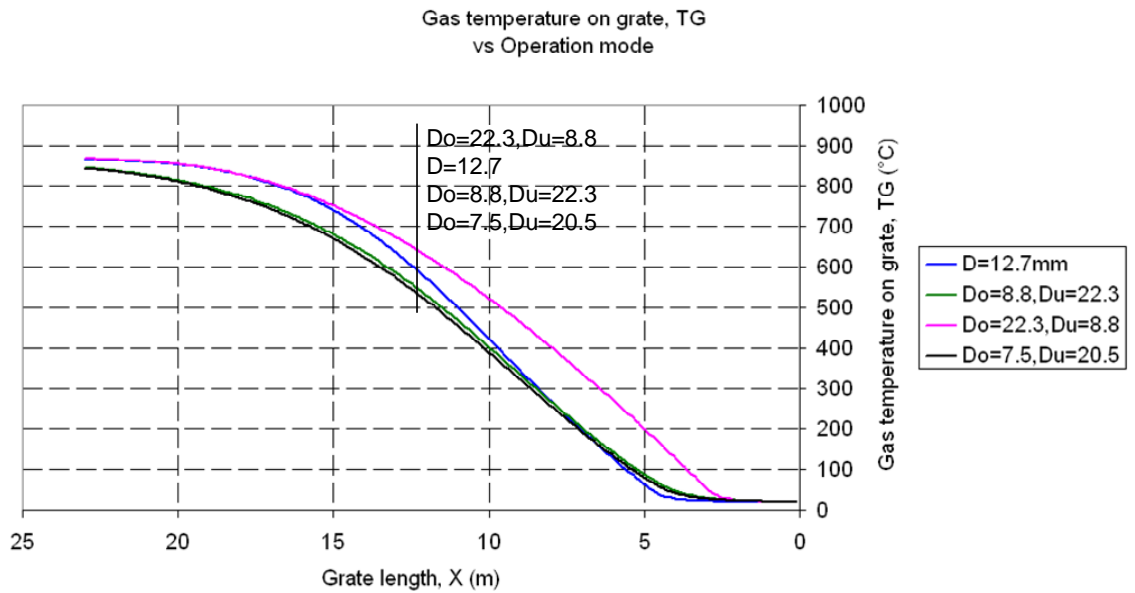


Figure 6.30 Influence of operation mode on gas temperature

74

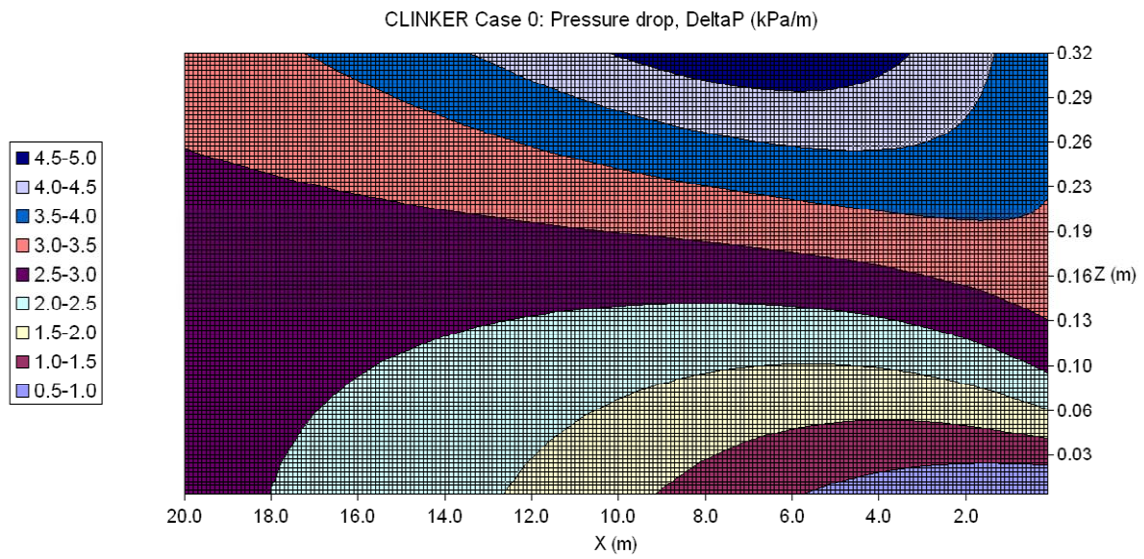


Figure 7.1 CLINKER-case 0: Pressure drop

75

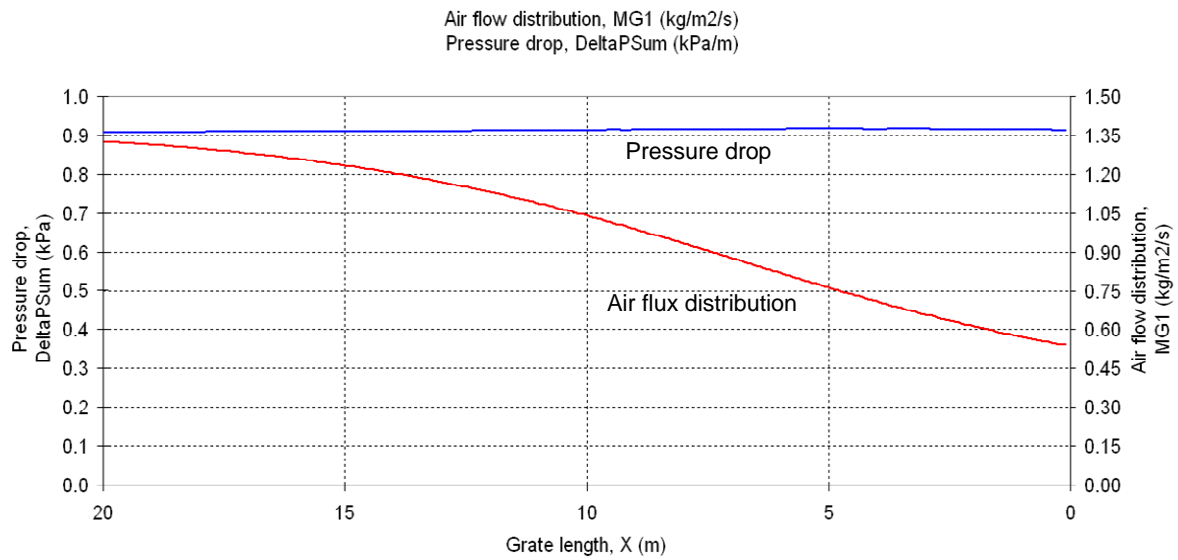


Figure 7.2 CLINKER-case 0: Total pressure drop

76

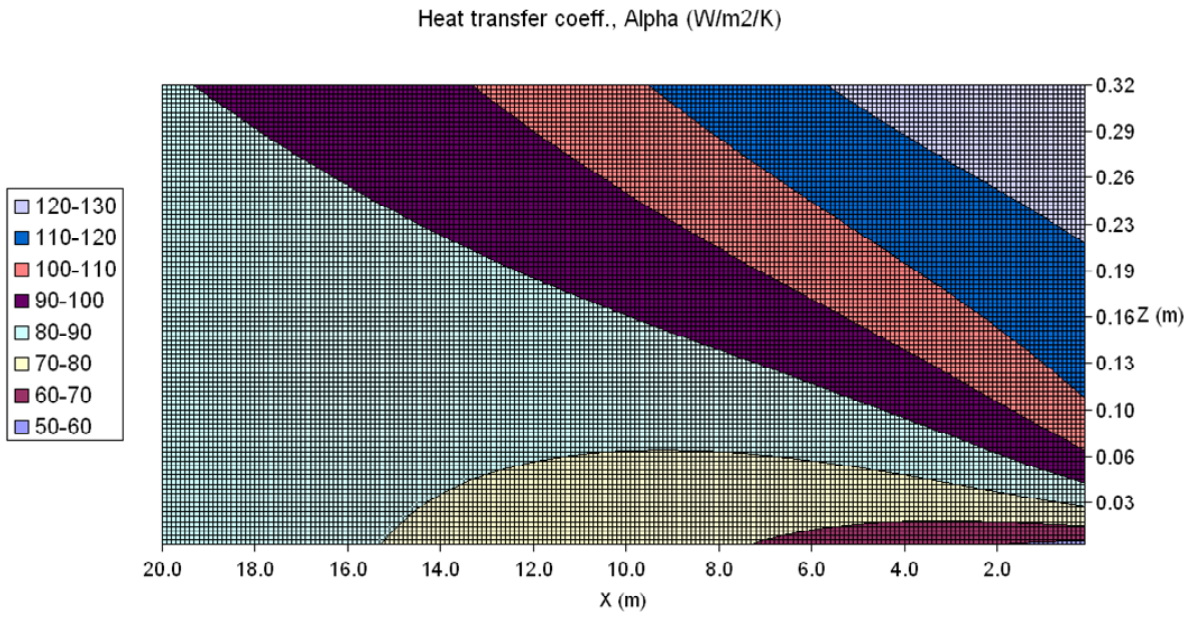


Figure 7.3 CLINKER-case 0: Heat transfer coefficient

77

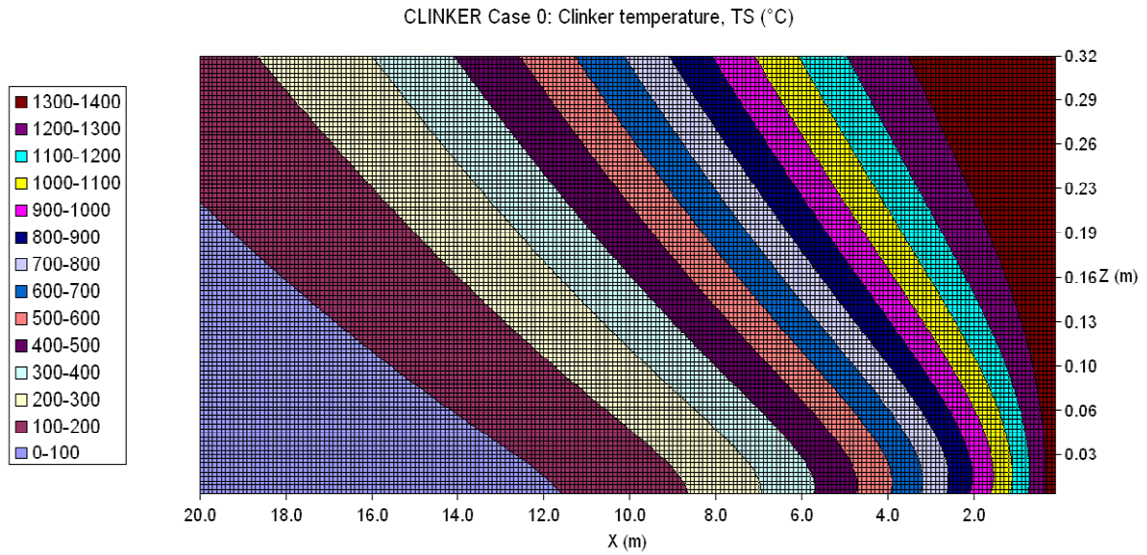


Figure 7.4 CLINKER-case 0: Particle temperature

78

CLINKER Case 0: Air temperature, TG (°C)

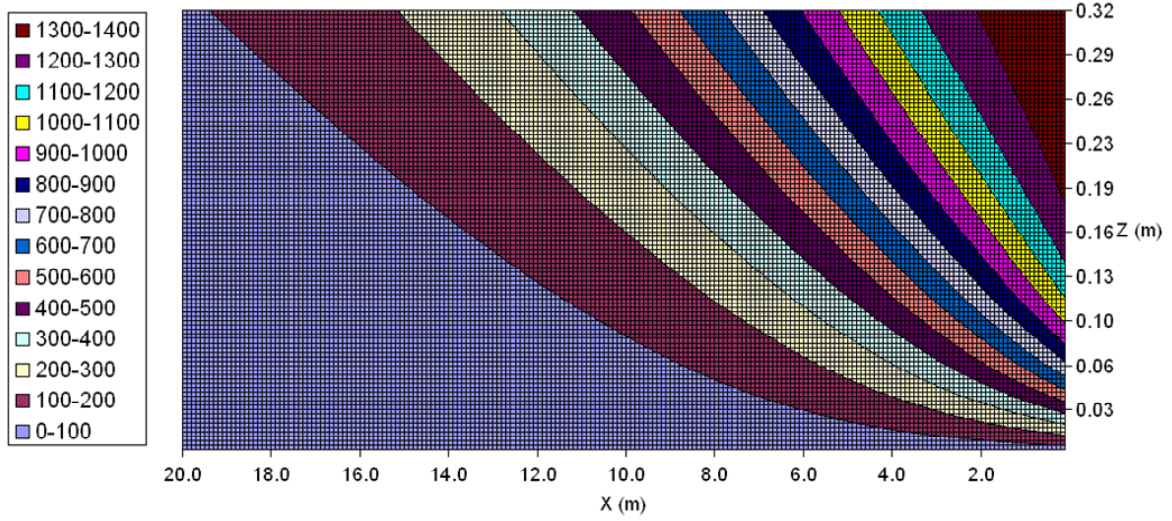


Figure 7.5 CLINKER-case 0: Air temperature

79

Min. fluidisation velocity, WGmf (m/s)

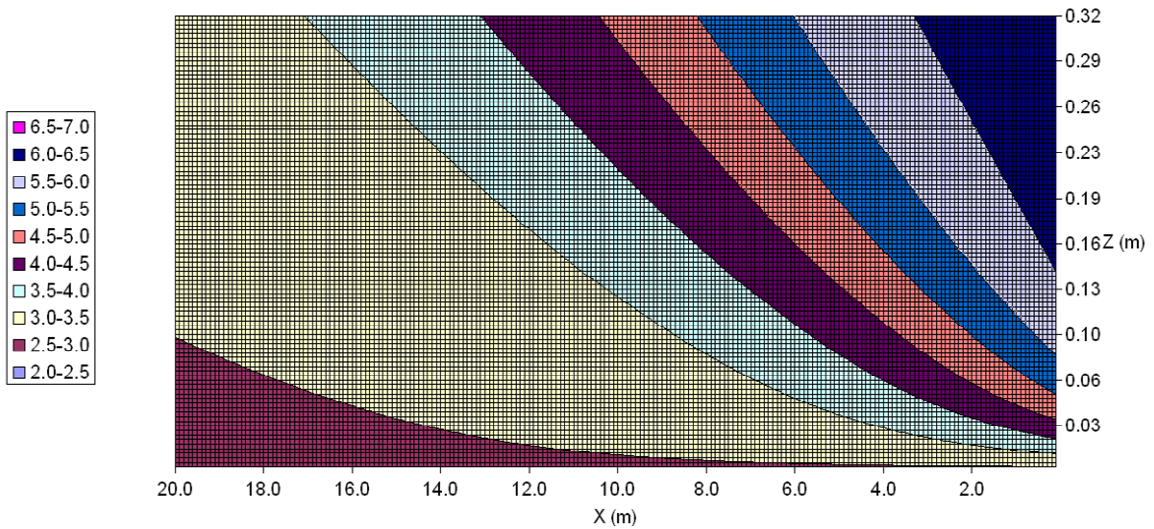


Figure 7.6 CLINKER-case 0: Minimal fluidization velocity

80

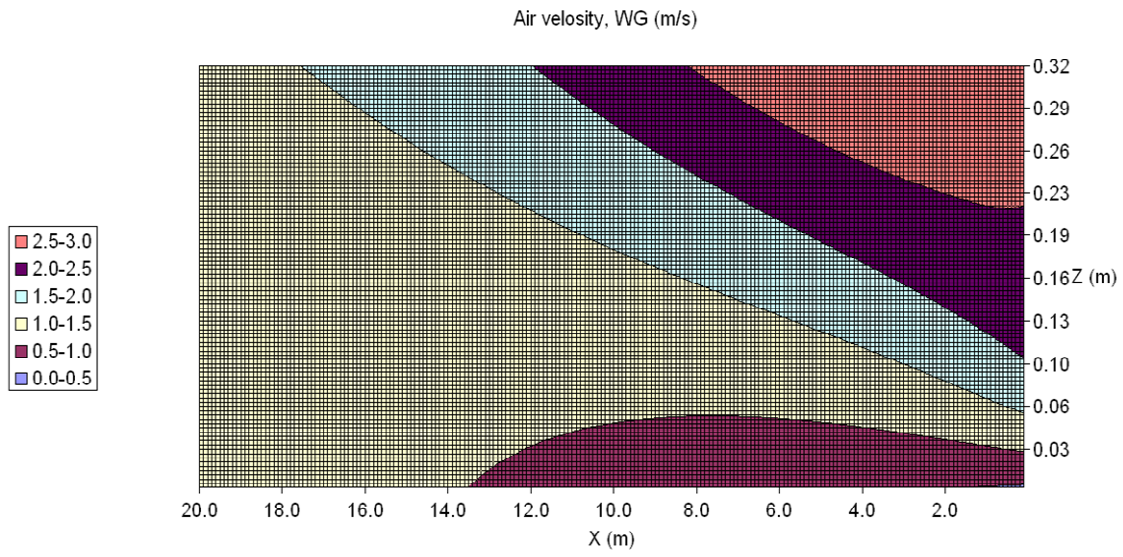


Figure 7.7 CLINKER-case 0: Real air velocity

81

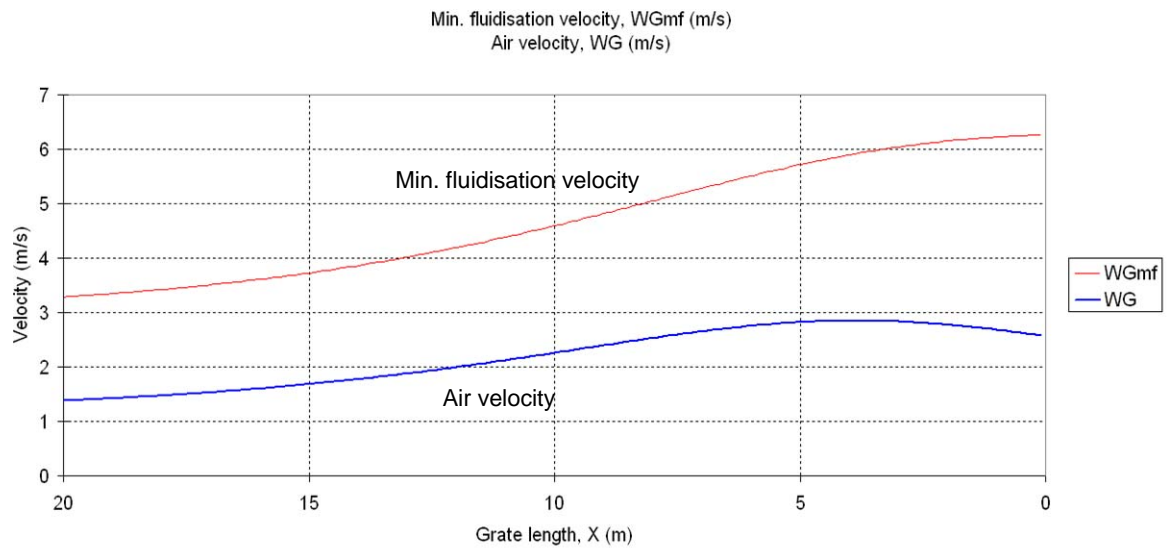


Figure 7.8 CLINKER-case 0: Air velocity comparison

82

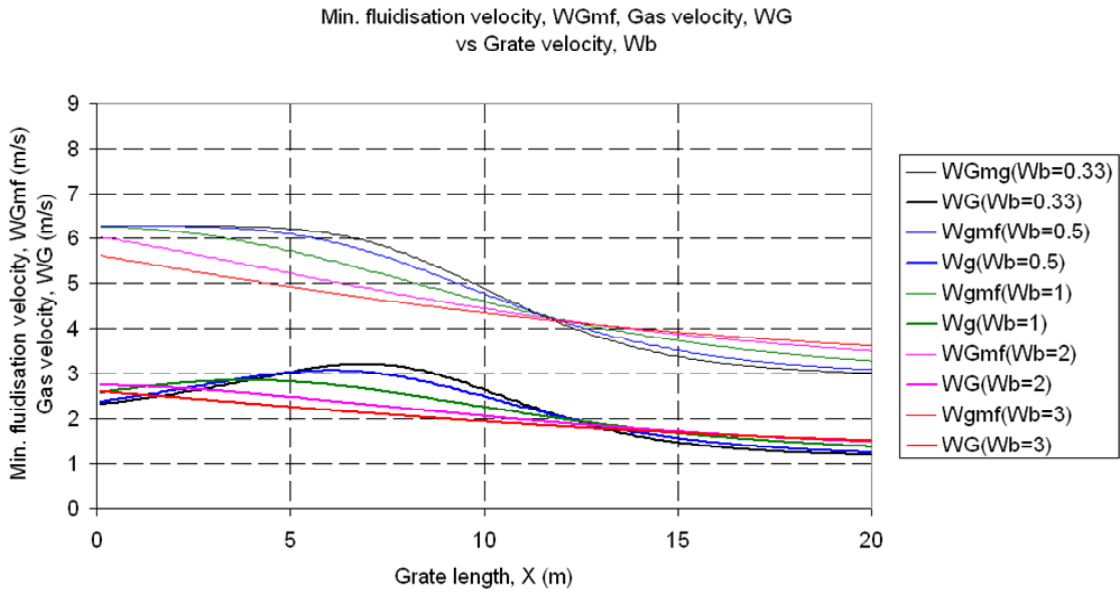


Figure 7.9 Influence of grate velocity on air velocity

83

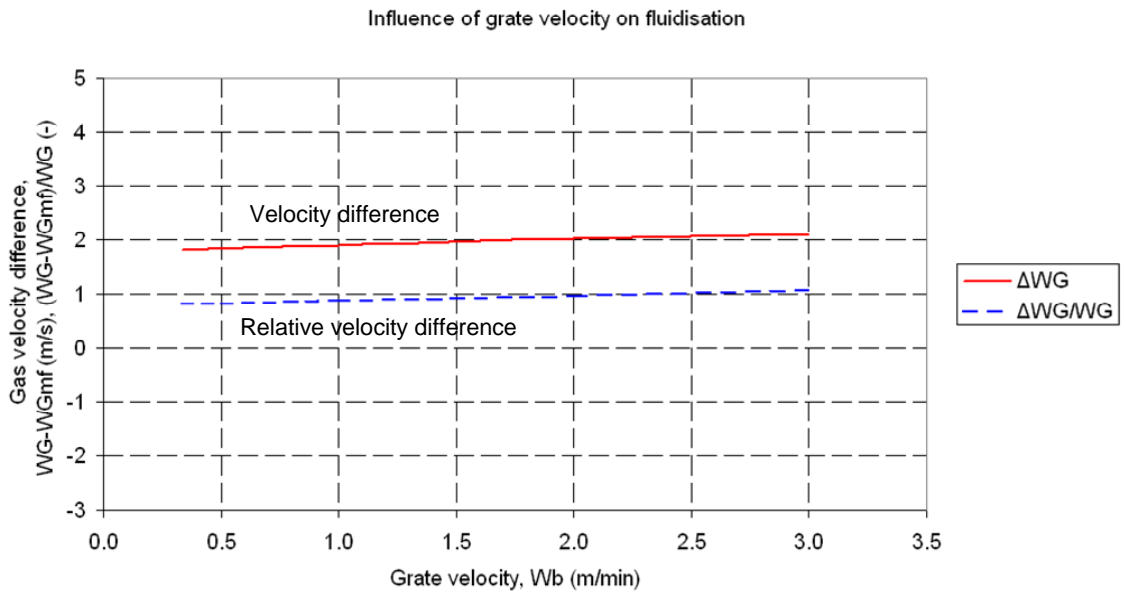


Figure 7.10 Influence of grate velocity on fluidisation potential

84

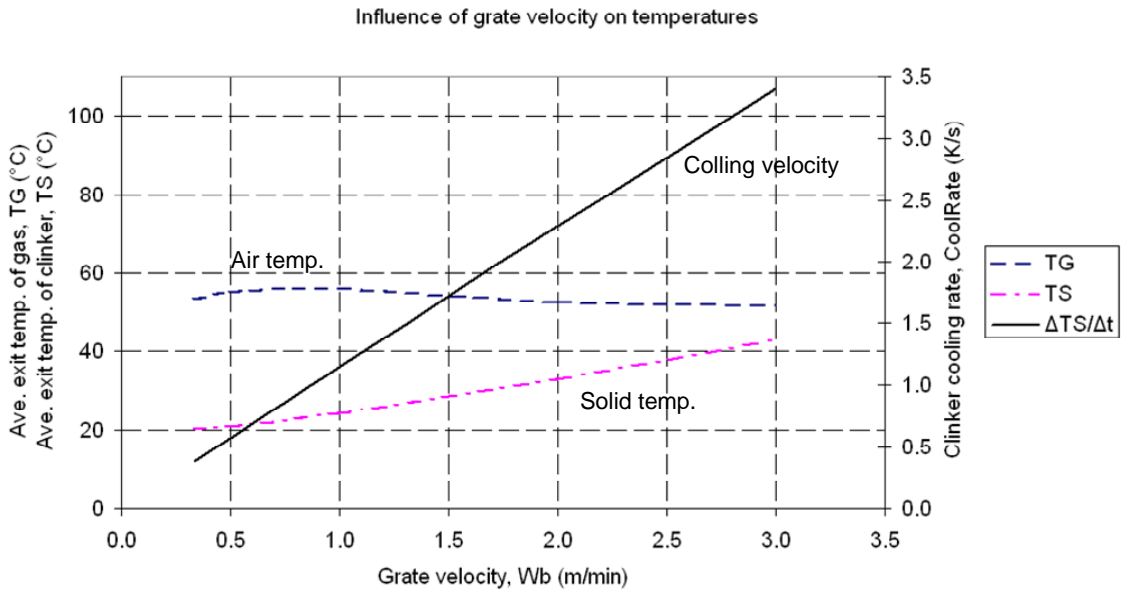


Figure 7.11 Influence of grate velocity on cooling effect

85

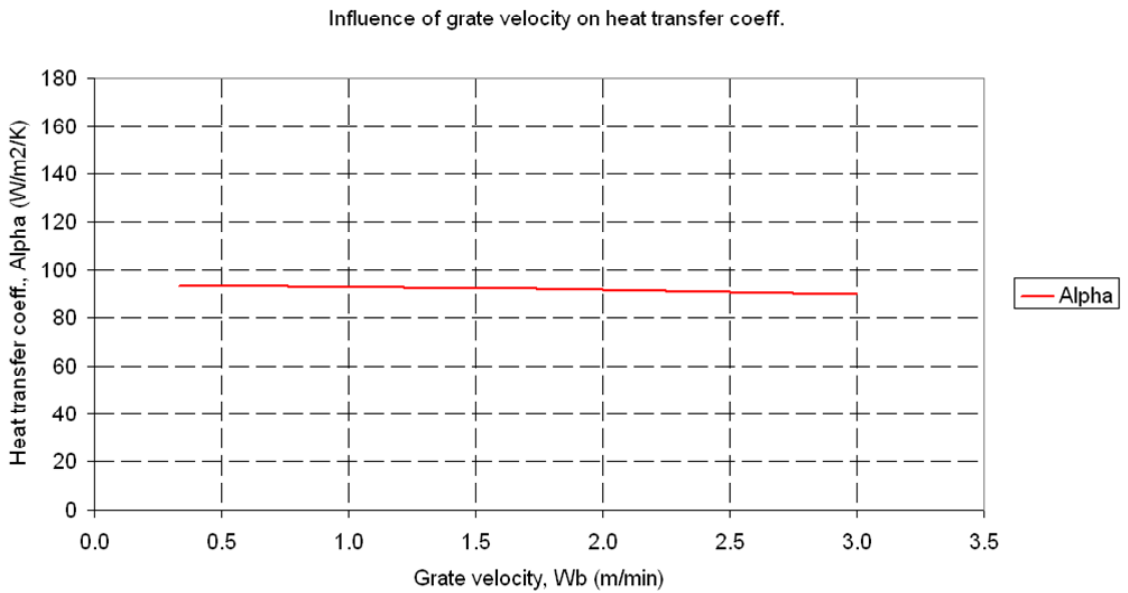


Figure 7.12 Influence of grate velocity on HTC

86

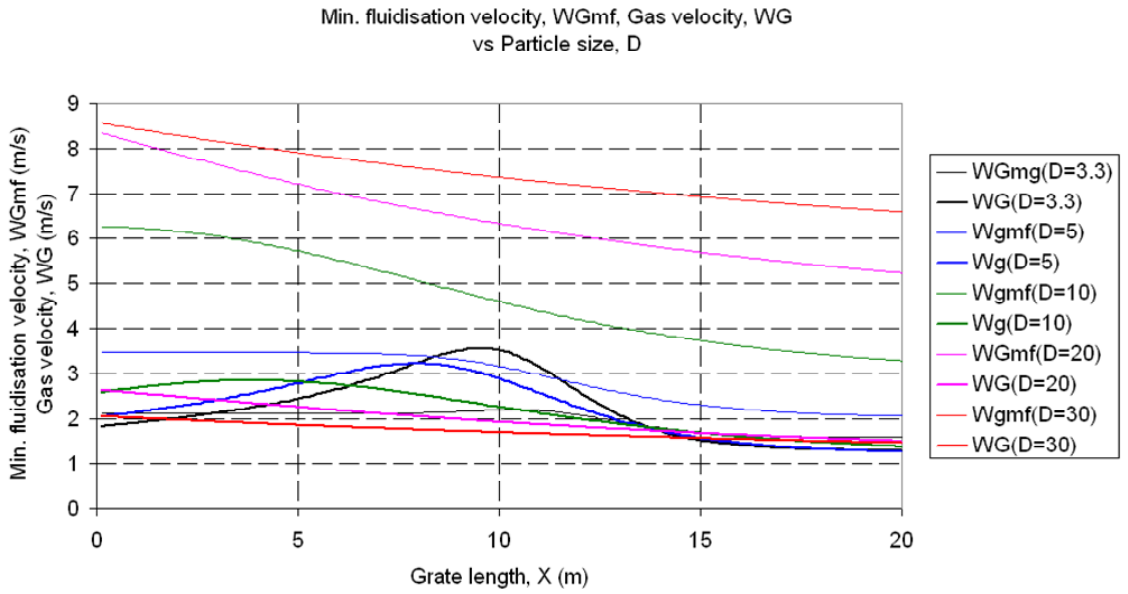


Figure 7.13 Influence of particle size on air velocity

87

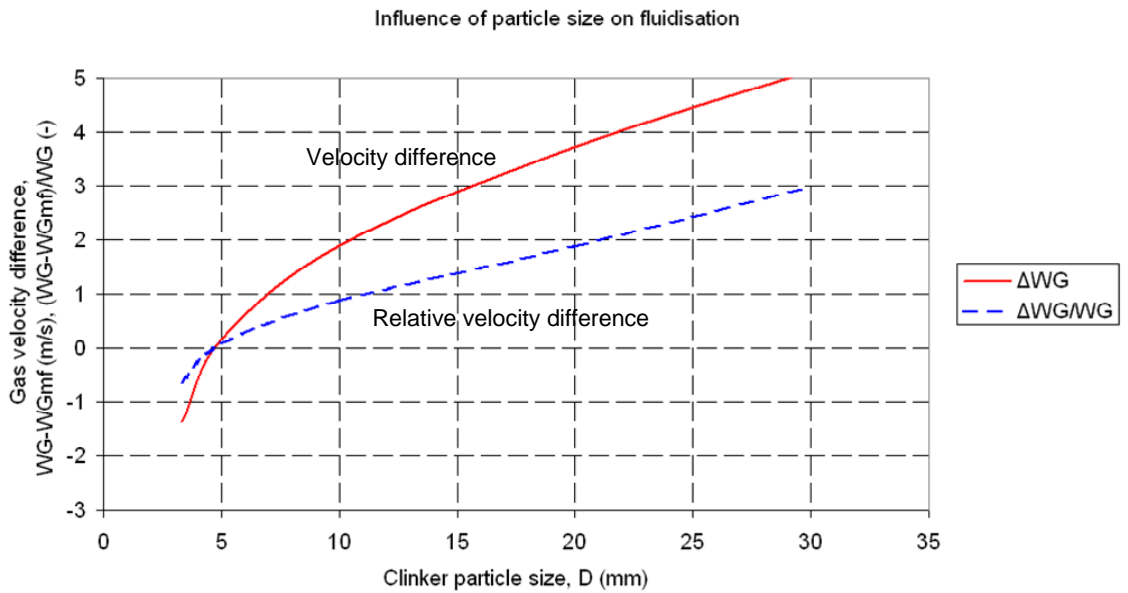


Figure 7.14 Influence of particle size on fluidisation potential

88

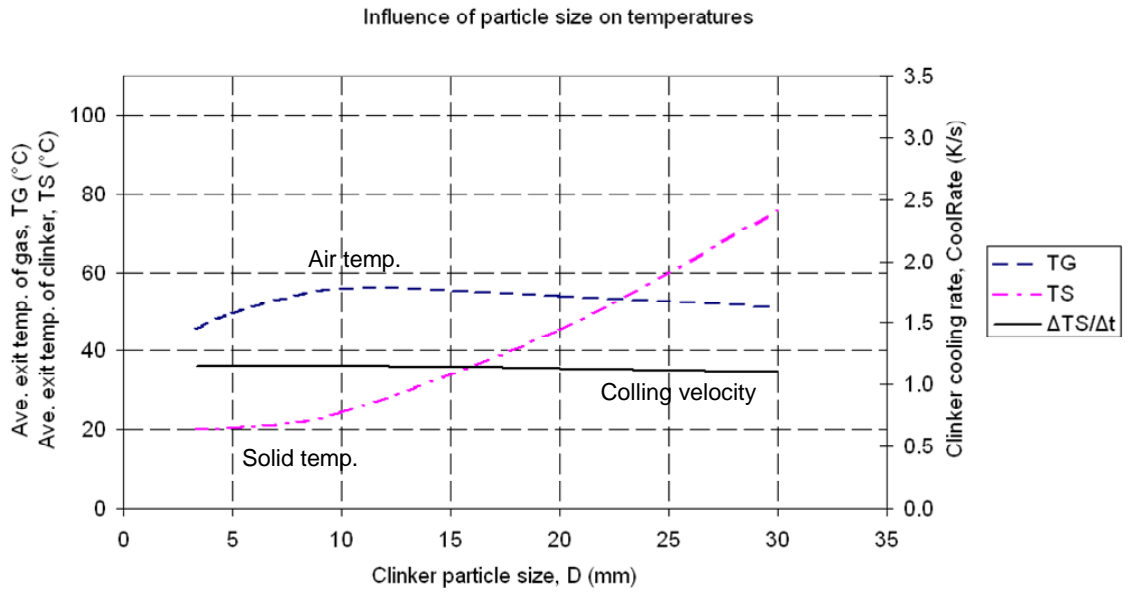


Figure 7.15 Influence of particle size on cooling effect

89

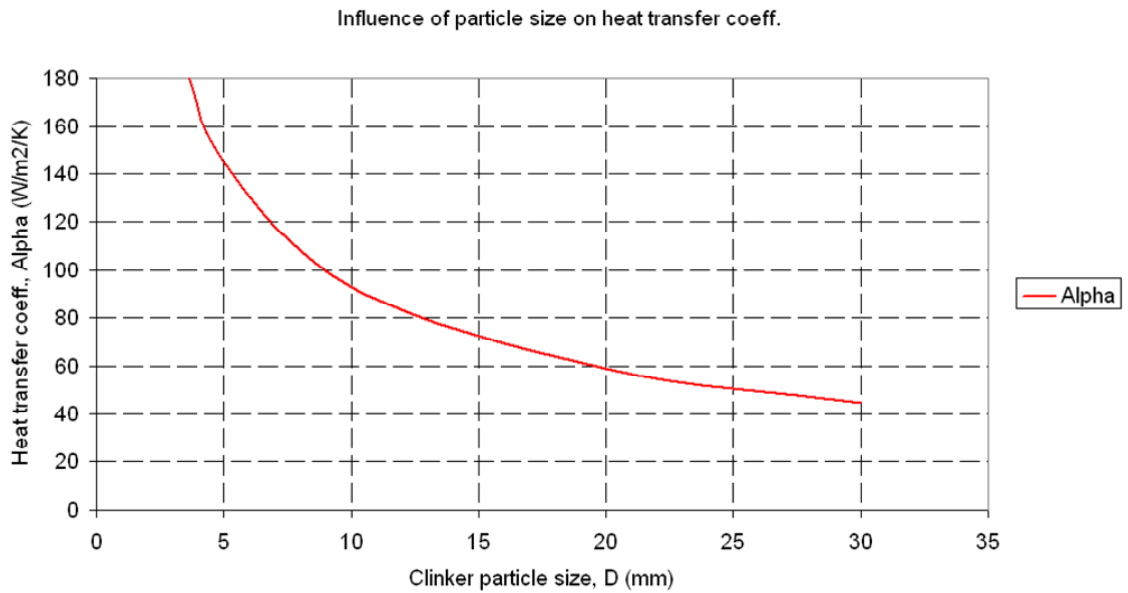


Figure 7.16 Influence of particle size on HTC

90

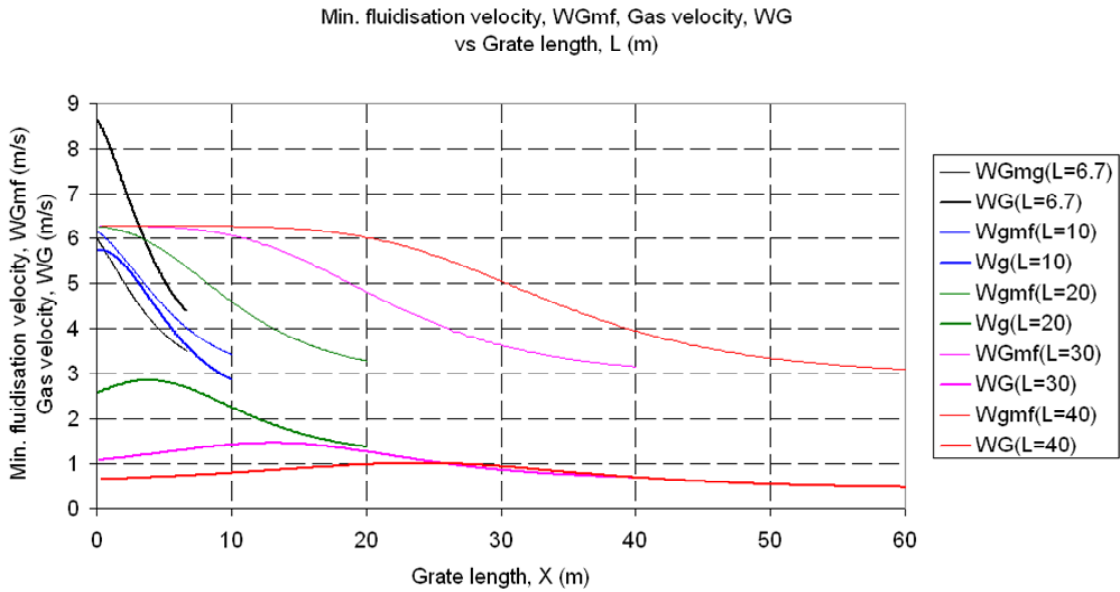


Figure 7.17 Influence of grate length on air velocity

91

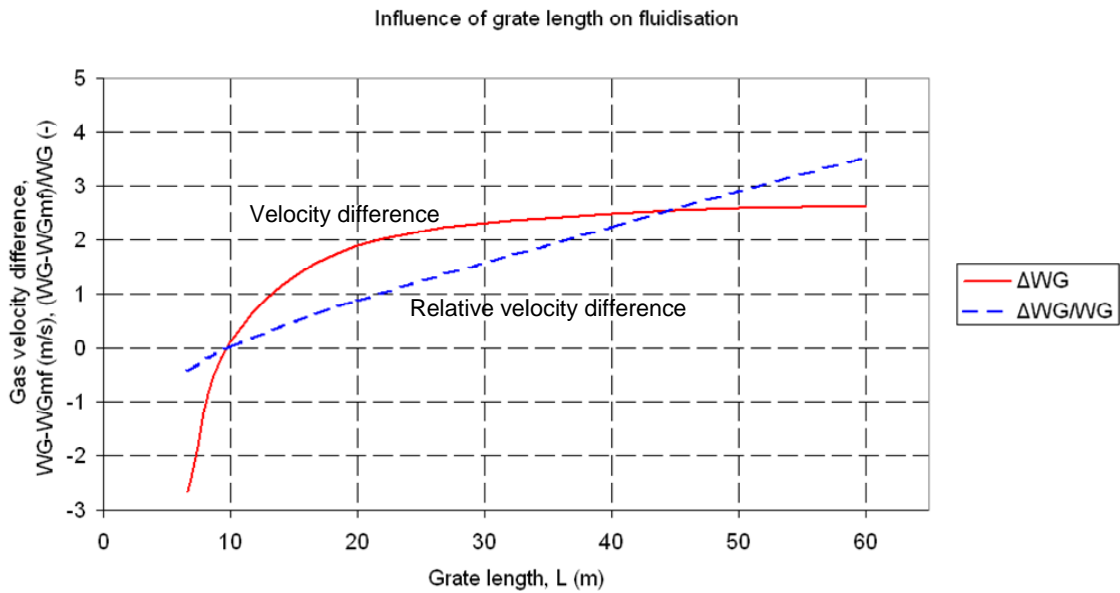


Figure 7.18 Influence of grate length on fluidisation potential

92

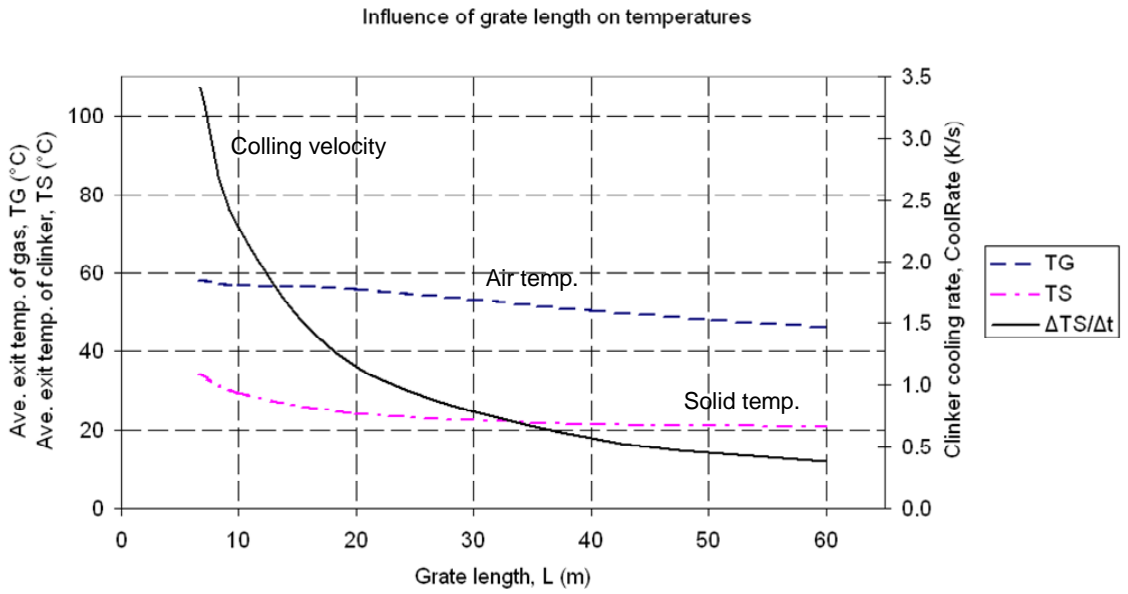


Figure 7.19 Influence of grate length on cooling effect

93

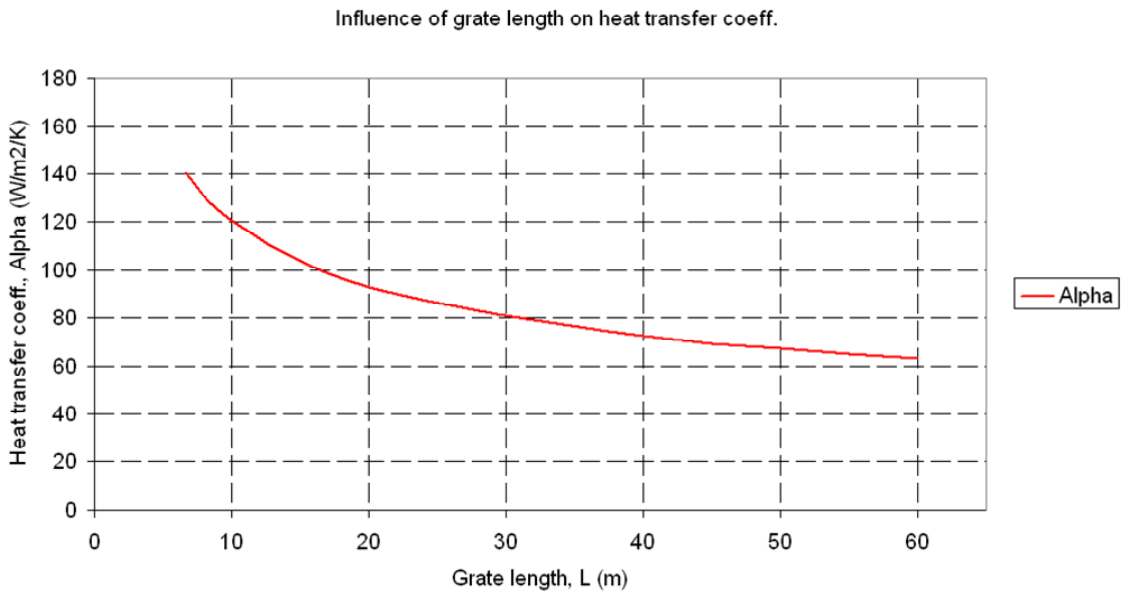


Figure 7.20 Influence of grate length on HTC

94

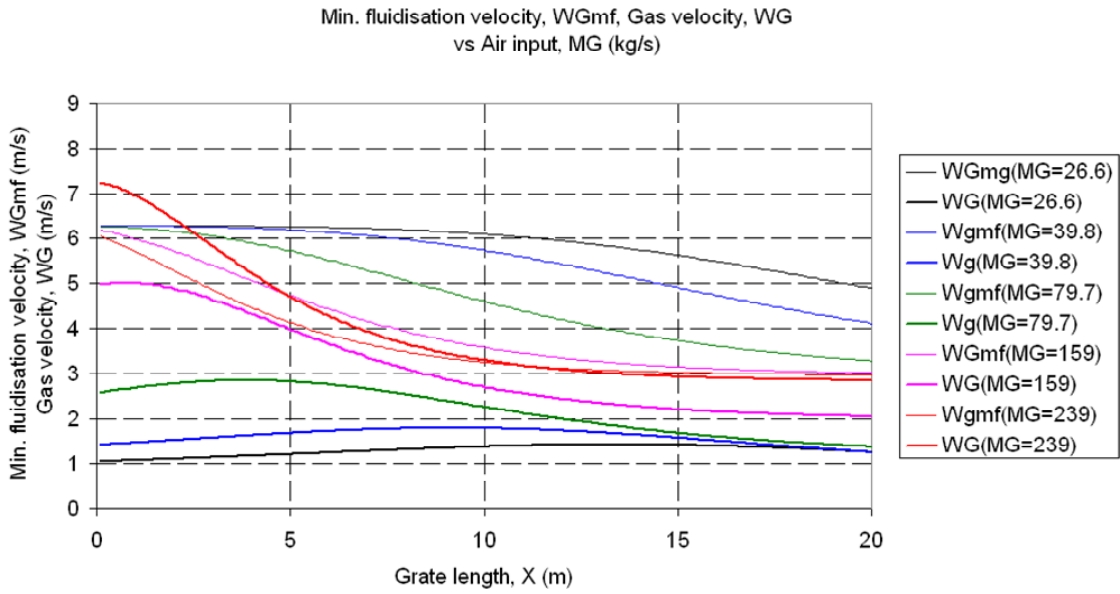


Figure 7.21 Influence of air amount on air velocity

95

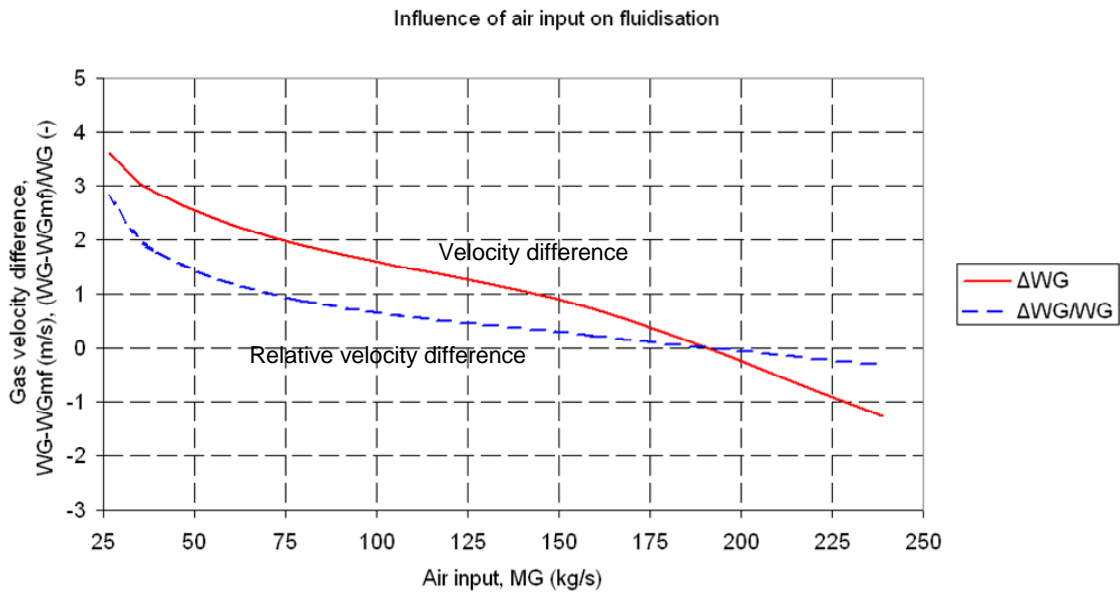


Figure 7.22 Influence of air amount on fluidisation potential

96

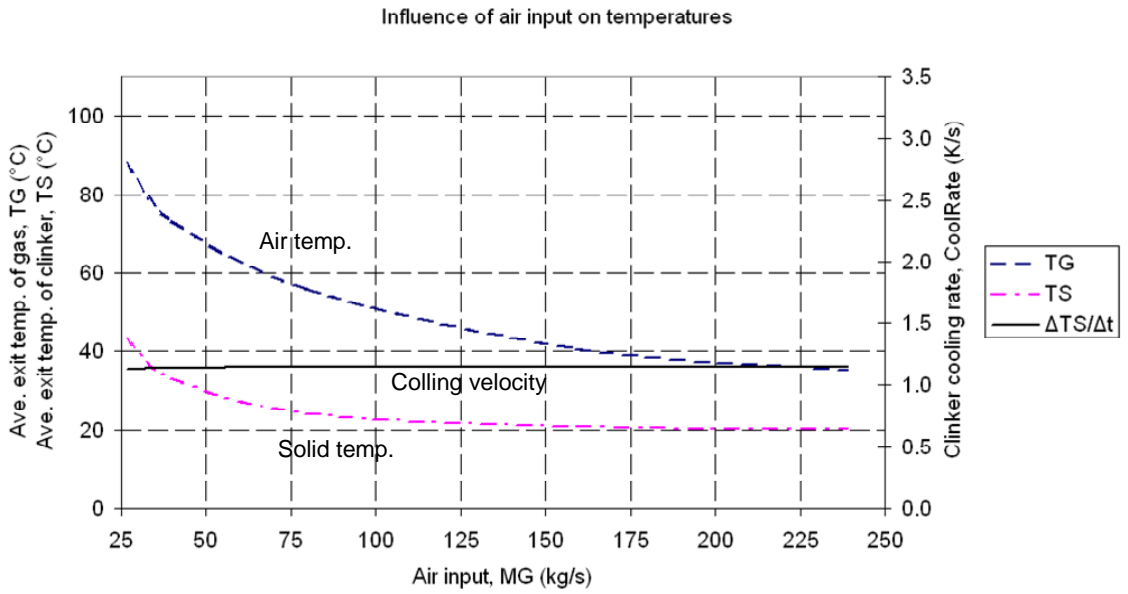


Figure 7.23 Influence of air amount on cooling effect

97

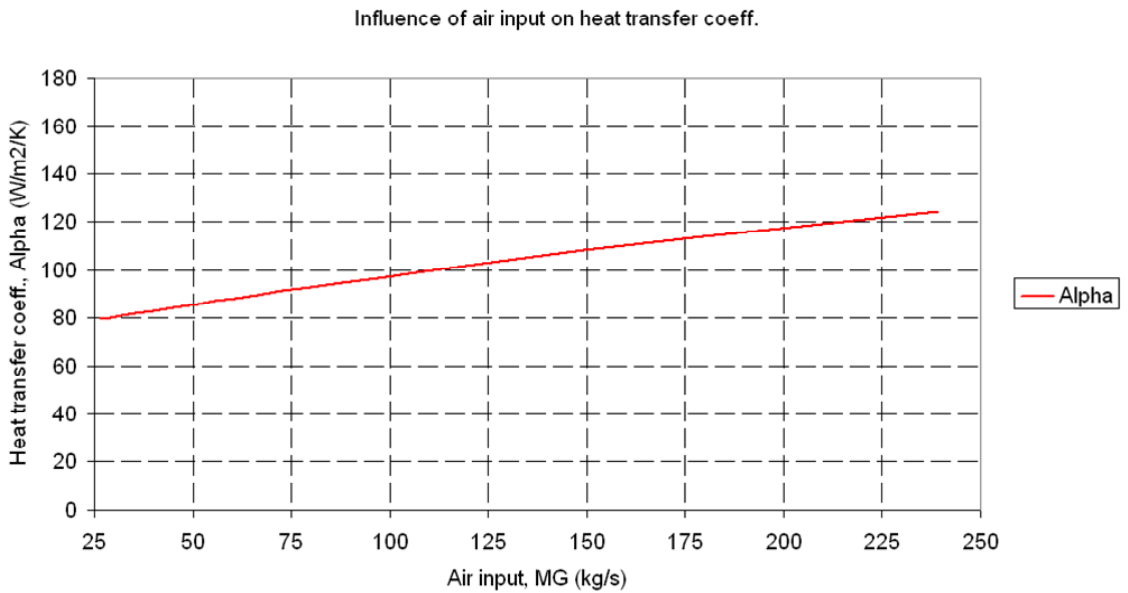


Figure 7.24 Influence of air amount on HTC

98

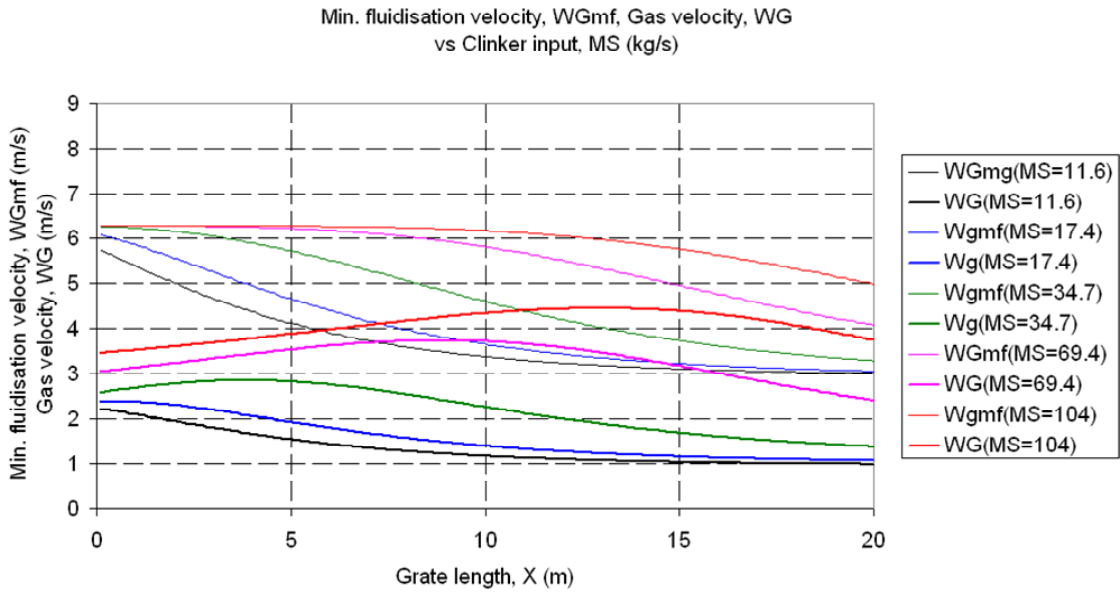


Figure 7.25 Influence of clinker amount on air velocity

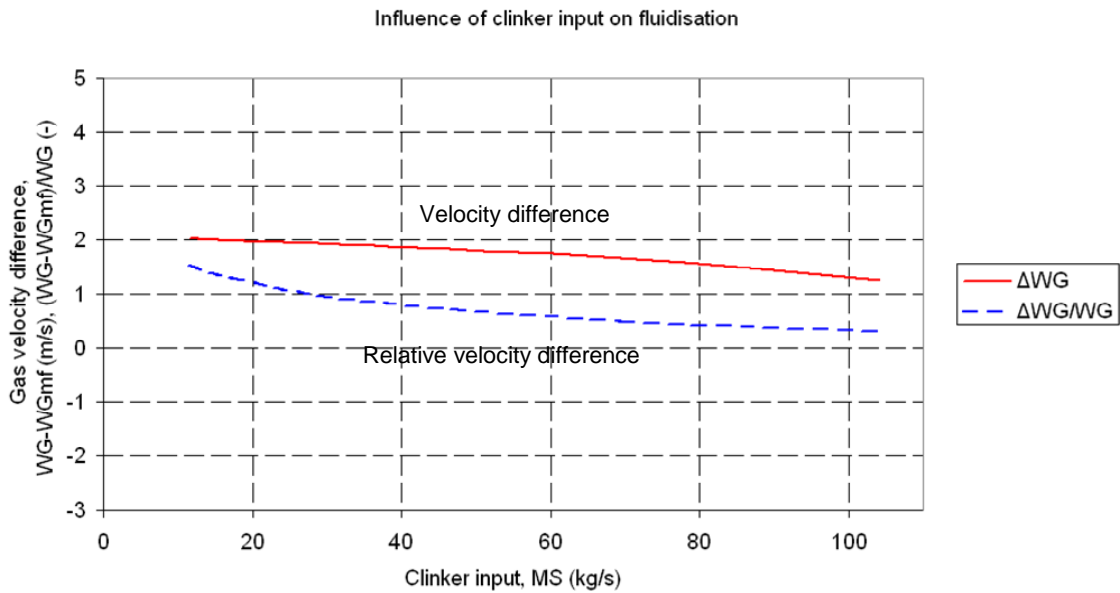


Figure 7.26 Influence of clinker amount on fluidisation potential

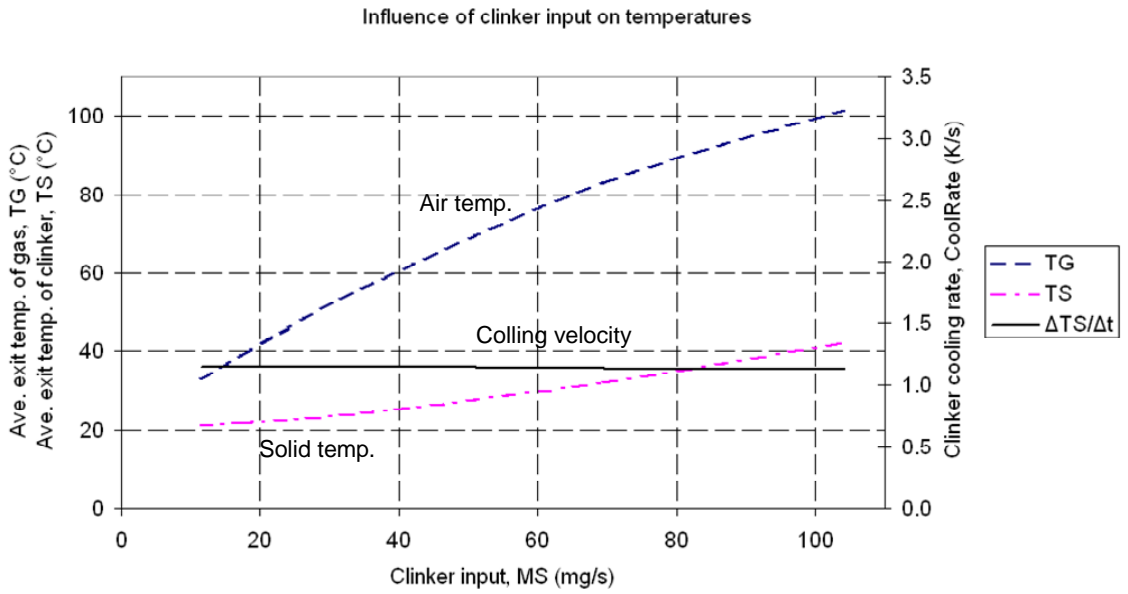


Figure 7.27 Influence of clinker amount on cooling effect

101

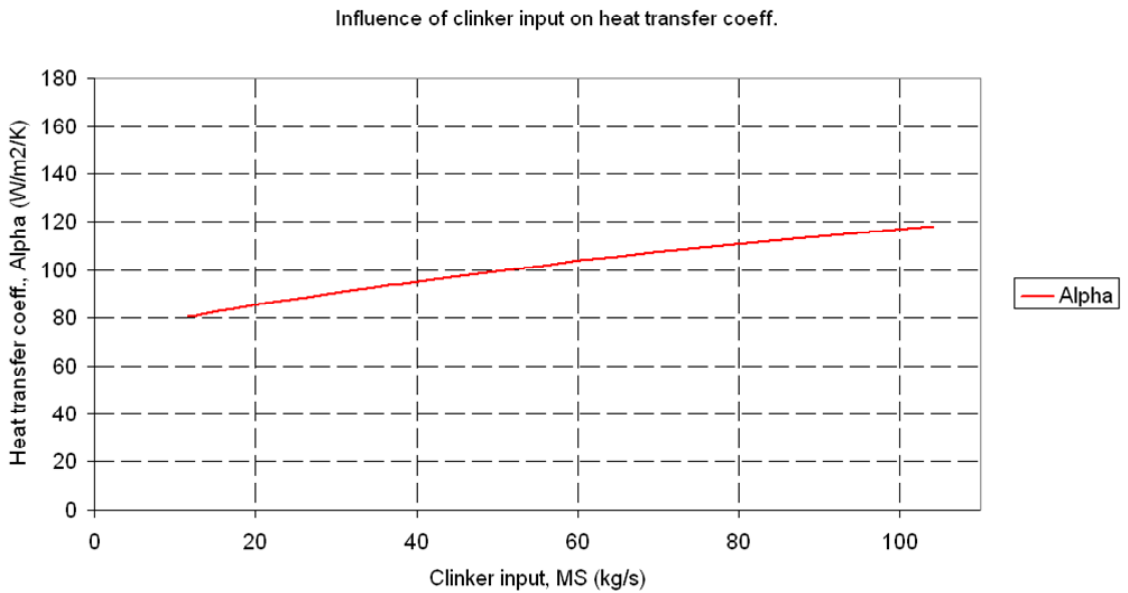


Figure 7.28 Influence of clinker amount on HTC

102

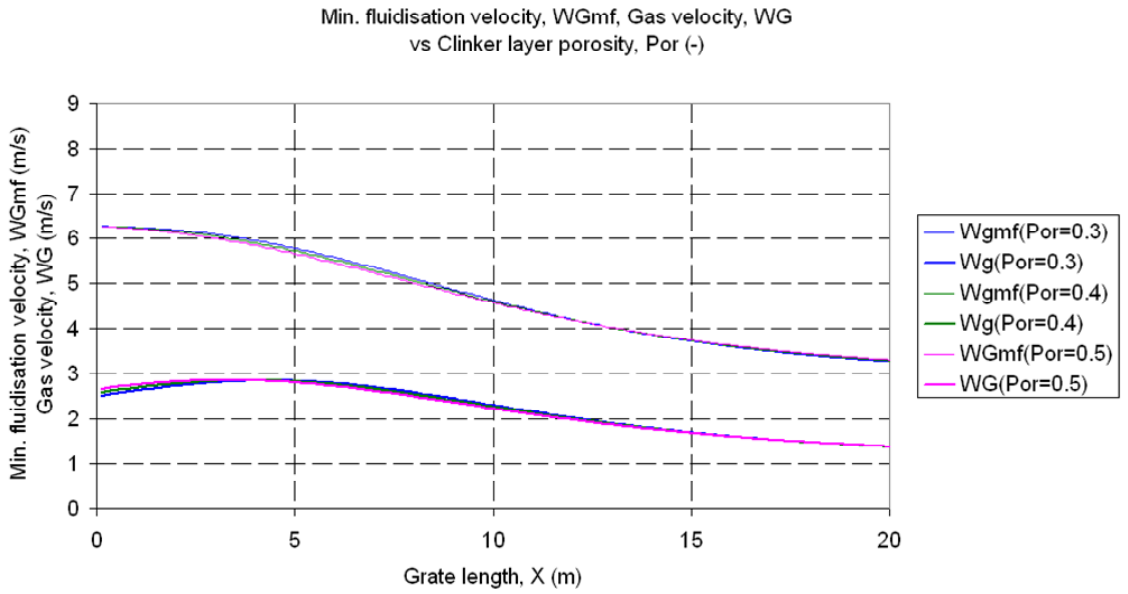


Figure 7.29 Influence of porosity on air velocity

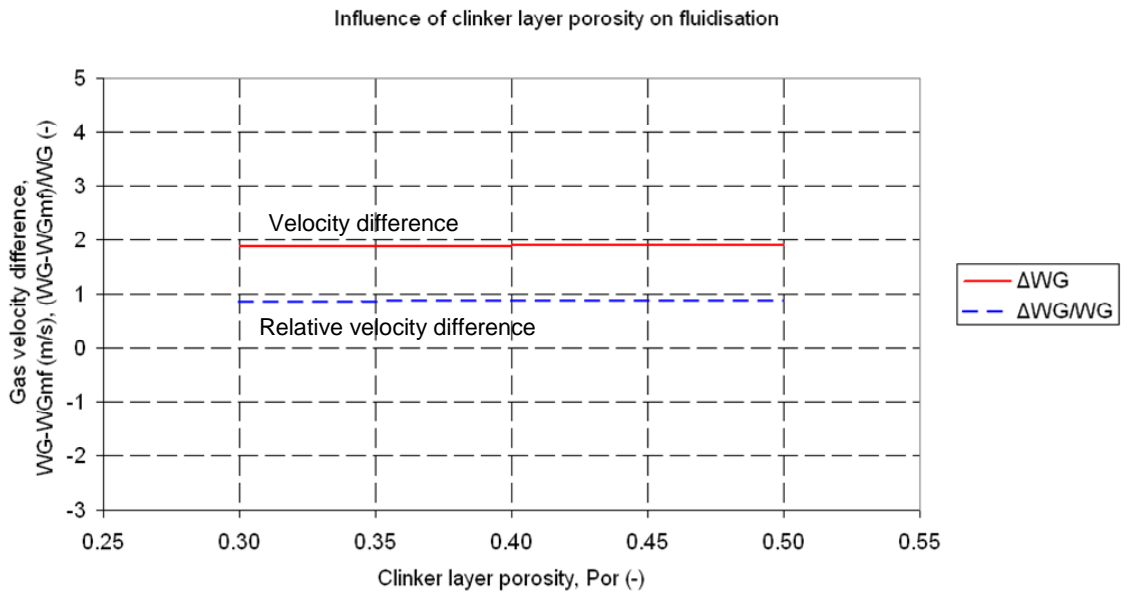


Figure 7.30 Influence of porosity on fluidisation potential

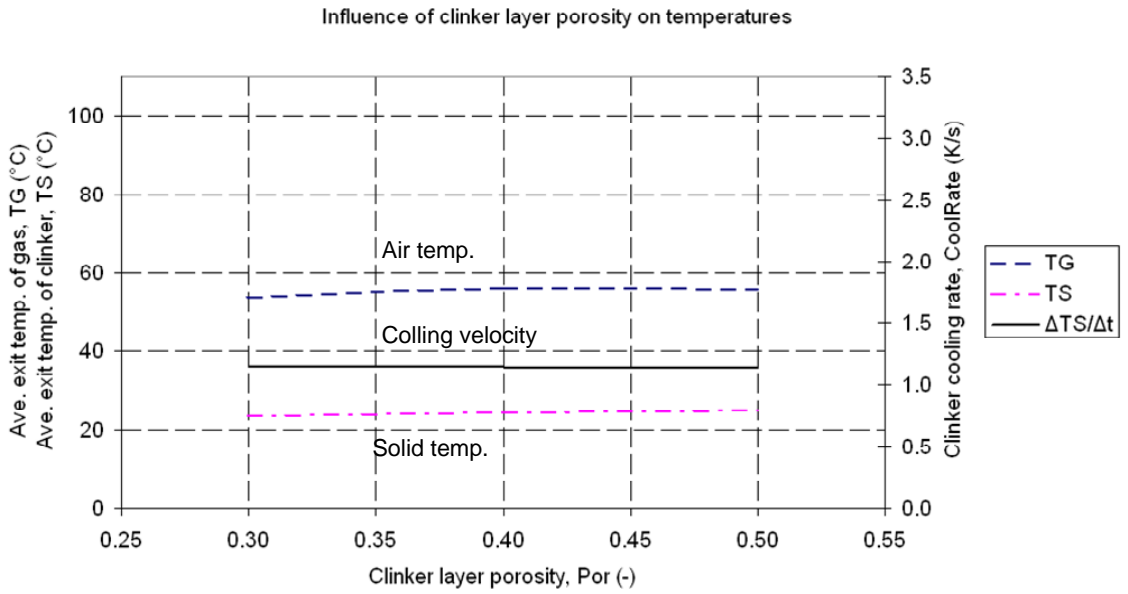


Figure 7.31 Influence of porosity on cooling effect

105

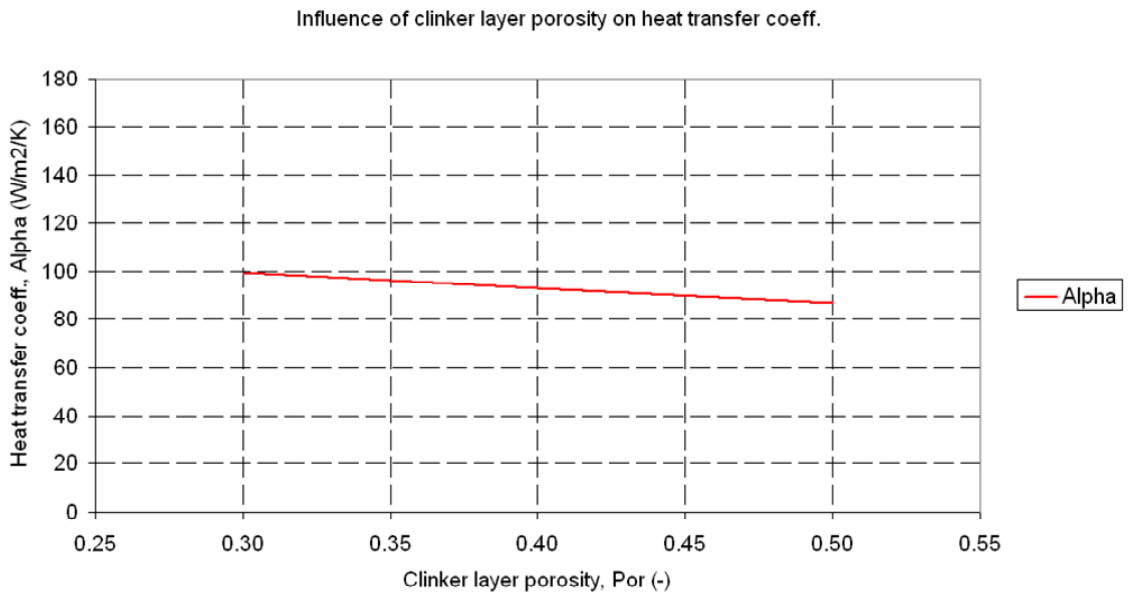


Figure 7.32 Influence of porosity on HTC

106

Literature

- [1] Clayton, P., Coleman, P., Leonard, A., Loader, A., Marlowe, I., Mitchell, D., Richardson, S., Scott, D. and Woodfield, M.: Review of solid waste incineration in the UK, Warren Spring Laboratory (National Environmental Technology Centre) Report No. LR776 (PA), Department of Trade and Industry, London, 1991
- [2] Nakamura, M. and Themelis, N. J.: Modeling of Solid Waste Flow and Mixing on the Traveling Grate of a Waste-to-energy Combustion Chamber, 12th North American Waste To Energy Conference (NAWTEC)
- [3] VDI-Gesellschaft Verfahrenstechnik und Chemieingenieurwesen (Hrsg.): VDI-Wärmeatlas, 10. bearbeitete und erweiterte Auflage, Springer-Verlag, 2006
- [4] Duda, W.H.: Cement data-book, Band 1, 3. Auflage, Bauverlage GmbH, Wiesbaden und Berlin, 1985
- [5] Taylor, H.F.W.: Cement chemistry, 2. Edition, Thomas Telford, London, 1997
- [6] Williams, P.T.: Waste Treatment and Disposal, 2nd Ed., John Wiley & Sons, Ltd., Chichester, 2005
- [7] W. Yang, C. Ryu, S. Choi, E. Choi, D. Lee and W. Huh: Modeling of combustion and heat transfer in an iron ore sintering bed with considerations of multiple solid phases, ISIJ International, Vol. 44 (2004), No. 3, 492-499
- [8] Gnielinski, V.: Gleichungen zur Berechnung des Wärme- und Stoffaustausches in durchströmten ruhenden Kugelschüttungen bei mittleren und großen Pecletzahlen, Verfahrenstechnik, 12 (1978), Nr.6, 363-367
- [9] Gnielinski, V.: Berechnung des Wärme- und Stoffaustausches in durchströmten, ruhenden Schüttungen, Verfahrenstechnik, 16 (1982), Nr.1, 36-39
- [10] Jeschar, R.: Heat transfer in pelletizing with mixed feed, Archiv für das Eisenhüttenwesen, 35 (1964), H.6
- [11] Bes, A.: Dynamic Process Simulation of Limestone Calcination in Normal Shaft Kilns, Dissertation, Universität Magdeburg, 2006
- [12] Jeschar, R., Specht, E., Alt, R.: Grundlagen der Wärmeübertragung, Viola-Jeschar-Verlag, Goslar, 1990
- [13] Wadell, H.: Volume, shape and roundness of quartz particles, J. Geol., 43 (1935) 250-280
- [14] Ergun, S.: Fluid flow through packed columns, Chem. Engng. Prog., 48 (1952) 2, 89-94
- [15] Brauer, M.: Grundlagen der Einphasen- und Mehrphasenströmungen, Sauerländer Verlag, Aarau u. Frankfurt, 1971
- [16] Molerus, O.: Fluid-Feststoff-Strömungen, Strömungsverhalten feststoffbeladener Fluide und kohäsiver Schüttgüter, Springer-Verlag, Berlin, 1982
- [17] Molerus, O.: Principles of Flow in Disperse Systems, Chapman & Hall, London, 1993
- [18] Schweinzer, J.: Druckverlust in und gaskonvektiver Wärmeübergang an Festbetten und Wirbelschichten, Dissertation, University Erlangen-Nürnberg, 1987
- [19] Wen, C.Y. and Y.H. Yu: Generalized Method for Predicting the Minimum Fluidization Velocity, AIChE, 12 (1996) 610-612
- [20] A.B. Fuertes, G. Marban, F. Rubiera: Kinetics of thermal decomposition of limestone particles in a fluidized bed reactor, Trans. IChemE., 71 (1993) 421-428
- [21] M. Rähler: Zur Erzeugung von aktivem Branntkalk, Dissertation TU Clausthal, 1977
- [22] J. Szekely, J.W. Evans, H.Y. Sohn: Gas-Solid-Reactions, Academic press, New York, 1976
- [23] H. Kainer, E. Specht, R. Jeschar: Die Porendiffusions-, Reaktions- und Wärmeleitkoeffizienten verschiedener Kalksteine und ihr Einfluss auf die Zersetzungszeit, Cement Lime Gypsum, 39 (1986) 214-219
- [24] W.R. Bandi and G. Krapf: The effect of CO₂ pressure and alkali salt on the mechanism of decomposition of dolomite. Thermochemica Acta, 14 (1976) 221-243
- [25] Nußelt, W.: Eine neue Formel für den Wärmeübergang im Kreuzstrom, Tech. Mech. U. Therm., 1 (1930) 417-422
- [26] Mason, J.L.: Heat Transfer in Cross-Flow. Proc. 2nd US Natnl. Cong. Appl. Mech., ASME (1955) 801-803

- [27] Cheng, C. and Specht, E.: Reaction coefficients in decomposition of lumpy limestone of different origin, *Thermochimica Acta*, 449 (2006) 8-15
- [28] Zawadski, J., Bretsznajder, S.: Some remarks on the mechanism of reactions of the type: solid=solid+gas, *Trans. Faraday Soc.*, 34 (1983) 951
- [29] Ingraham, T.R., Marier, P.: Kinetic studies on the thermal decomposition of calcium carbonate, *Can. J. Chem. Eng.*, 41 (1963) 170
- [30] Borgwadt, R.H.: Calcium oxide sintering in atmospheres containing water and carbon dioxide, *Ind. Eng. Chem. Res.*, 28 (1989) 493
- [31] Rao, T.R.: Kinetics of calcium carbonate decomposition, *Chem. Eng. Technol.*, 19 (1996) 373-377
- [32] F. Garcia-Labiano, A. Abad, L.F. de Diego, P. Gayan, J. Adanez: Calcinations of calcium-based sorbents at pressure in a broad range of CO₂ concentrations, *Chem. Eng. Sci.*, 57 (2002) 2381-2393
- [33] Ar, I., Dogu, G.: Calcination kinetics of high purity limestones, *Chem. Eng. J.*, 83 (2001) 131-137
- [34] Barin, I.: *Thermochemical Data of Pure Substances*, 3. Edition, 1995, VCH, Weinheim
- [35] Specht, E., Kainer, H. and Jeschar, R.: Die Reaktions-, Porendiffusions- und Wärmeleitkoeffizienten verschiedener Magnesite und ihr Einfluß auf die Zersetzungszeit. *Radex-Rundschau* (1986) 259-268
- [36] Goldsmith, J.R., H.C. Heard: Subsolidus phase relations in the system CaCO₃•MgCO₃, *Journal Geology*, 69(1961), 45-74
- [37] Graf, D.L., J.R. Goldsmith: Dolomite-magnesian calcite relations at elevated temperatures and CO₂ pressures, *Geochimica et Cosmochimica Acta*, 7 (1955), 109-128
- [38] Harker, R.J., O.F. Tuttle: The thermal dissociation of calcite, dolomite and magnesite, *Am. Jour. Sci.*, 253 (1955), 209-224
- [39] Marc, R., Simek, A.: Über die thermische Dissoziation des Magnesiumkarbonates, *Z. anorg. Chemie*, 82 (1913), 21-49
- [40] Haul, A. W., Markus, J.: On the thermal decomposition of dolomite, *J. appl. Chem.*, 2 (1952), 298-306
- [41] Barin, I., Knacke, O., Kubaschewski, O.: *Thermochemical properties of inorganic substances*, Supplement, Springer-Verlag Berlin/Heidelberg/New York, 1977
- [42] Specht, E. and Jeschar, R.: Experimentelle Ermittlung der Porendiffusions-, Reaktions- und Wärmeleitkoeffizienten bei der Zersetzung von Kalksteinen, Magnesiten und Dolomiten, Bericht 8/85, Institut für Energieverfahrenstechnik, TU Clausthal, 1985
- [43] Specht, E.: *Kinetik der Abbaureaktionen*, Cuvillier Verlag, Göttingen, 1993

Lebenslauf

Persönliche Daten

Name: Chuan Cheng
Geburtsdatum: 15.04.1970
Geburtsort: Sichuan / V.R.China.
Staatsangehörigkeit: chinesisch
Familienstand: verheiratet

Schulausbildung und Studium

2002 – 2003 Master of Science
Fachrichtung: Quality, Safety and Environment (QSE)
Studium an der Otto-von-Guericke-Universität Magdeburg
1988 – 1992 Bachelor of Engineering
Fachrichtung: Environmental Monitoring
Studium an der Tongji-Universität, Shanghai / V.R.China.
1982 – 1988 Abschluss High School
Junlian Middle School, Sichuan / V.R.China.

Berufliche Erfahrung

ab August 2006 Wissenschaftlicher Mitarbeiter,
Otto-von-Guericke-Universität Magdeburg
Oktober 2001 – September
2002 Praktikant im Projekt „Umweltorientierte Unternehmensführung“,
Deutschland.
Juli 1992 – September 2000 Ingenieur,
Chengda Engineering Corporation of China, Sichuan / V.R.China.